UNIVERSITY OF OKLAHOMA

GRADUATE COLLEGE

NANOPARTICLES ADSORBED AT THE OIL/WATER INTERFACE: INSIGHTS FROM DISSIPATIVE DYNAMICS SIMULATIONS

A DISSERTATION

SUBMITTED TO THE GRADUATE FACULTY

in partial fulfillment of the requirements for the

Degree of

DOCTOR OF PHILOSOPHY

By

CUONG XUAN LUU
Norman, Oklahoma
2014

Downloaded from SHAREOK. Persistent Handle URL: https://hdl.handle.net/11244/10496

NANOPARTICLES ADSORBED AT THE OIL/WATER INTERFACE: INSIGHTS FROM DISSIPATIVE DYNAMICS SIMULATIONS

A DISSERTATION APPROVED FOR THE
SCHOOL OF CHEMICAL, BIOLOGICAL AND MATERIALS ENGINEERING

BY

_____
Dr. Dimitrious V. Papavassiliou, Chair

_____
Dr. Alberto Striolo

_____
Dr. Friederike Jentoft

_____
Dr. Robert L. Shambaugh

_____
Dr. Takumi Hawa

© Copyright by CUONG XUAN LUU 2014
All Rights Reserved.

To all my beloved family

Acknowledgements

It was indeed a unique experience and great pleasure to conduct research under the guidance of Dr. Alberto Striolo at the University of Oklahoma. This work would not have been possible without his help, guidance, encouragement, and support. His mentorship, innovative way of thinking, and expertise in my field of research significantly helped me to not only complete my research goals, but also grow as an independent thinker. I would like to express my gratitude to my advisor, Dr. Striolo for his understanding and patience during these years.

I would like to thank my committee members: Dr. Dimitrios V. Papavassiliou, Dr. Friederike Jentoft, Dr. Robert L. Shambaugh, and Dr. Takumi Hawa for their help and support during my graduate studies at the University of Oklahoma.

The completion of this work would not have been possible without the support from the OU Supercomputing Center for Education and Research (OSCER) in Norman, Oklahoma and the National Energy Research Scientific Computing Center (NERSC) in Berkeley, California.

This work would not have been feasible without financial support from the Experimental Program to Stimulate Competitive Research (EPSCOR) in Oklahoma, and the National Science Foundation (NSF).

I would like to thank my co-workers in our groups. I also have very much appreciated the help from our department's staff.

Last but not least, I would like to thank my family for their unending love, encouragement and support.

Table of Contents

Acknowledgements iv

Table of Contents v

List of Tables viii

List of Figures ix

Chapter 1. Introduction 1

1.1. Emulsion Overview 1

1.2. Stability of Emulsions 1

1.3. Particles as Emulsifiers 2

1.3.1. Pickering Emulsions 2

1.3.2. Pickering Emulsion Stabilization Mechanism 3

1.4. Parameters Affecting the Stability of Pickering Emulsions. 7

1.4.1. Particle Characteristics 7

1.4.2. Operation Conditions 8

1.5. Liquid Crystals 9

1.6. Research Objectives 9

Chapter 2. Simulation Methodology 11

Chapter 3. Nanoparticles Adsorbed at the Water/Oil Interface: Coverage and Composition Effects on Structure and Diffusion 14

3.1. Abstract 14

3.2. Introduction 14

3.3. Simulation Methodology 16

3.4. Results and Discussion 18

3.4.1. Single-NP Systems 19
3.4.2. Mixed NPs Systems 27
3.5. Conclusions 30
Chapter 4. Ellipsoidal Janus Nanoparticles Adsorbed at the Water-Oil Interface: Some Evidence of Emergent Behavior 32
4.1. Abstract 32
4.2. Introduction 32
4.3. Simulation Methodology 35
4.4. Results 38
4.4.1. NPs Orientation 38
4.4.2. Emergent Behavior 42
4.4.3. Isotropic-to-Nematic Transition 46
4.4.4. Interfacial Tension 50
4.5. Conclusions 52
Chapter 5. Ellipsoidal Janus Nanoparticles Assembled at Spherical Oil/Water Interfaces 53
5.1. Abstract 53
5.2. Introduction 54
5.3. Methods and Algorithms 55
5.4. Results 58
5.4.1. Oil Droplets Immersed in Water 58
5.4.2. Water Droplets Immersed in Oil 66
5.5. Discussion 68

5.6. Conclusions 70

Chapter 6. Conclusions and Future Work 71

References 73

APPENDIX 93

List of Tables

Table 2.1. DPD interaction parameters expressed in k_BT / R_c units. Symbols ‘w’, ‘o’, ‘ap’, and ‘p’ are for water beads, oil beads, NP non-polar beads, and NP polar beads, respectively. 13

Table 3.1. Three-phase contact angle θ obtained from DPD simulations. Data are averaged over all surface densities considered in this work for simulations with one NP type. 18

Table 5.1. Radial order parameter S_R, and average orientation angle of NPs adsorbed on an oil droplet of diameter $50R_c$ immersed in water. The errors are obtained as one standard deviation from the average of three simulations. NPs have aspect ratio 2 and surface chemistry N=30 or 70. 59

List of Figures

Figure 1.1. Desorption energy of a particle as a function of contact angle at various particle radius. 5

Figure 1.2. Bending behavior of emulsion droplets coated in particles[43] 5

Figure 3.1. Representative simulation snapshot for the systems considered in this work. A biphasic system containing water and oil is considered. Pink and cyan beads represent water (w) and oil (o), respectively. At the conditions considered water and oil yield two planar interfaces, where several nanoparticles (NPs) adsorb. The number of NPs adsorbed on one interface equals that adsorbed on the other interface. Purple and green beads represent non-polar (ap) and polar beads (p) on the NPs, respectively. In the specific case considered in this snapshot 50% of the NPs are homogeneous (50HP) and 50% Janus (50JP). Details on NPs type are given in Figure 3.2. 16

Figure 3.2. Schematic representation of the NPs simulated in this work. Different panels represent different NPs: panel (a) is for 75HP; (b) for 50HP; (c) for 25HP; (d) for 25JP; (e) for 50JP; and (f) for 75JP NPs. Purple and green beads are non-polar (ap) and polar (ap), respectively. HP and JP indicate homogeneous and Janus NPs, respectively. 17

Figure 3.3. Interfacial tension as a function of surface coverage for various NPs at the water/oil interface. Only one type of NP is present in each of the systems considered. Symbols are simulation results. The error bars represent one standard deviation from the average. Lines are guides to the eye. 20

Figure 3.4. Six-bond orientational order parameter obtained for different NPs as a function of surface coverage. Panels (a) and (b) are for homogenous and Janus NPs,

respectively. Error bars are obtained as one standard deviation from the average. Lines are guides for the eye. 21

Figure 3.5 Two-dimensional radial distribution functions *g(r)* obtained for various NPs at increasing the NP surface coverage. Panels (a), (b), (c), and (d) are for 75HP, 25HP, 50HP, and 50JP NPs, respectively. The insets are enlargements at short NP-NP distances. Results are obtained at increasing surface density. 23

Figure 3.6. Top view of representative simulation snapshots obtained for 50JP NPs assembled at the water-oil interface. Panels (a) and (b) are for surface coverage 0.53 and 0.79, respectively. The results are representative of disordered liquid-like structure and of ordered hexagonal structure, respectively. 23

Figure 3.7. Self-diffusion coefficient as a function of surface coverage for various NP types. Panels (a), (b), and (c) compare 75HP and 25HP, 75JP and 25JP, and 50HP and 50JP NPs, respectively. Error bars, one standard deviation from the average, can be smaller than the symbols. Lines are guides for the eye..... 24

Figure 3.8. Vector-vector autocorrelation function (Eq. (3.4)) as a function of time for 75HP NPs at various surface coverages (panel a), and for six different NPs at surface coverage ϕ =0.66 (panel b). 26

Figure 3.9. Two-dimensional radial distribution functions *g(r)* for the three NP mixtures considered in this work. In all cases the total surface coverage is ϕ =0.53. From top to bottom, the three panels are for 75HP and 25HP NPs, 75JP and 25JP NPs, and 50HP and 50JP, respectively. For each mixture, results are obtained at various compositions, expressed by 'x', as indicated in the panels. 28

Figure 3.10. Averaged two-dimensional self-diffusion coefficient obtained for NPs in the three mixtures considered in Figure 3.9. In all cases $\phi = 0.53$ but the mixture composition changes systematically. The variable *x* represents the fraction of 75HP NPs in mixture 1 (composed by 75HP and 25HP NPs), that of 75JP NPs in mixture 2 (composed by 75JP and 25JP NPs), and that of 50HP NPs in mixture 3 (composed by 50HP and 50JP NPs). Lines are guides for the eye. 29

Figure 4.1. Schematic of one simulated system. Orthorhombic boxes are used, within which two planar water-oil interfaces are present. Pink and cyan beads represent water (w) and oil (o) beads, respectively. An equal number of ellipsoidal Janus nanoparticles (NPs) adsorb at both interfaces. Purple and green beads indicate nonpolar (ap) and polar (p) beads on the NPs, respectively. In this figure, each NP is a Janus prolate ellipsoid with aspect ratio 2.0. 35

Figure 4.2. Schematic presentations of two 50JP NPs. Panel 1 is for a prolate NP with *c/b*=4; panel 2 is for an oblate NP with *c/b*=0.5. To ease visualization, one part of each NP is removed and the axes are shown. Purple and green beads are nonpolar and polar, respectively. In panels 3 and 4, we show how the orientation angle α is defined for prolate and oblate NPs, respective. In this picture, n is the normal vector of the oil/water interface. 37

Figure 4.3. Orientation angle as a function of surface properties for various NPs. (1) Prolate NPs; (2) Oblate NPs. For these simulations the interface area per NP is maintained at $A_c \approx 84.34\ \mathrm{R}_c^2$. The results for cases c/b=2 and c/b=0.5 are averaged from the results obtained from three independent simulations. Error bars represent one

standard deviation from the average, and can be smaller than symbols. Lines are guides to the eye..... 38

Figure 4.4. Averaged orientation angle for ellipsoidal NPs at the water-decane interface as a function of surface area per NP, A_c. For each Janus NP the results are shown for two levels of surface 'nonpolar coverage' x, 30 and 70. The error bars represent one standard deviation from the average. In most cases the error is smaller than the symbols. Lines are guides to the eye. Different panels are for different NPs: (a) *c/b*=0.3; (b) *c/b*=0.5; (c) c/b=1; (d) c/b=1.5; (e) c/b=2.0; (f) c/b=4.0. In panel c the two data sets overlap. 44

Figure 4.5. Representative simulation snapshots for some ellipsoidal Janus NPs adsorbed at the water-oil interface. The NP beads are colored consistently with Figure 4.2. The cyan beads represent oil beads. Water beads are not shown for clarity. Left and right panels are obtained at surface area per NP Ac~84 R_c^2 and ~28 R_c^2, respectively. From top to bottom, different panels are for different NPs: (a) c/b=0.5 with x=30; (b) c/b=0.5 with x=70; (c) c/b=2 with x=30; (d) c/b=2 with x=70; (e) c/b=4 with x=30. ... 45

Figure 4.6. Two-dimensional radial distribution functions *g(r)* obtained for various NPs with aspect ratio *c/b*=2 at decreasing A_c. Panels (a) and (b) are for x=30 and 70, respectively. 47

Figure 4.7. Orientational correlation function C_p as a function of NP distance *r*. Left and right panels are obtained for x=30 and x=70, respectively. From top to bottom, different panels are for different NPs: (a) c/b=0.5; (b) c/b=2; (c) c/b=4; (d) c/b=0.5; (e) c/b=2; (f) c/b=4. In each panel the results are presented for different values of interface area per NP, A_C..... 49

Figure 4.8. Interfacial tension reduction as a function of interfacial area per NP (A_c) for selected NPs. The error bars represent one standard deviation from the average. Lines are guides to the eye. Different panels are for different NPs: (a) *c/b*= 4; (b) *c/b*=2; (c) *c/b* =1; (d) *c/b*=0.5. In each panel, NPs with different surface properties are compared. 51

Figure 5.1. Schematic of one typical simulation box. The oil droplet (cyan) is covered by NPs and immersed in water (pink). Green and purple beads are polar and nonpolar, respectively, on the NPs. The prolate NPs have aspect ratio 2.0, and 30% of the beads on their surface are nonpolar. 56

Figure 5.2. Schematic representing an ellipsoidal Janus NP adsorbed at the oil-water interface. In this picture, ap (pink), p (green), o (cyan), and w (purple) represent nonpolar, polar, oil, and water, respectively. u_i and R_i are the unit vectors along the NP c axis and along the radial direction from the center of the droplet, respectively. S_{p-w}, S_{p-o}, S_{ap-w}, and S_{ap-o} are polar NP surface in water, polar surface in oil, nonpolar surface in water, and nonpolar surface in oil, respectively. The interfacial area occupied by the NP, S_1, is highlighted in red. θ_a and θ_p are the contact angles of completely nonpolar and polar spherical NPs, respectively. 58

Figure 5.3. Representative simulation snapshots for ellipsoidal Janus NPs adsorbed on one oil droplet immersed in water. The color code is that of Figure 5.1. Water beads are not shown for clarity. The droplet diameter is $50R_c$. The NPs have aspect ratio 2. Left and right panels are for NPs with N=30 and N=70, respectively. Top and bottom panels are for $A_c = 90.5R_c^2$ and $A_c = 19.4R_c^2$, respectively. 60

Figure 5.4. One portion of the droplets surface shown in panels (b) and (d) of Figure 5.3 is extracted and magnified in panels (a) and (c), respectively. The interfacial areas are flattened and shown in panels (b) and (d), respectively. In these latter panels the filled circles are for the centers of NPs that have six nearest neighbors, the stars for NPs with more or less than six nearest neighbors, which are indicative of 'defects'. ... 62

Figure 5.5. Representative simulation snapshots for ellipsoidal Janus NPs adsorbed on one oil droplet. Water beads are not shown for clarity. The droplet diameter is $50R_c$. The NPs have aspect ratio 4. Left and right panels are for NPs with N=30 and N=70, respectively. From top to bottom, the NP surface density is increased: in panels (a) and (d) $A_c \sim 90 R_c^2$; (b) and (e) $A_c \sim 35 R_c^2$; (c) and (f) $A_c \sim 24 R_c^2$. 63

Figure 5.6. Representative simulation snapshots for ellipsoidal Janus NPs adsorbed at oil/water interfaces of increasing curvature. The NPs have aspect ratio 4. The area per NP is constant at $A_c \sim 24 R_c^2$. Left and right panels are for NPs with N=30 and N=70, respectively. Panels (a) and (d) are for flat interface; (b) and (e) for a droplet of diameter $d=75R_c$; (c) and (f) for a droplet of diameter $d=20R_c$ 64

Figure 5.7. Average orientation angle as a function of area per NP. Results are for NPs with aspect ratio c/b=4 and N=30. Different symbols are for different droplet diameters. The error bars are obtained as one standard deviation from the average of three simulations. The solid line is a 'master curve', which can be divided into three regions. See text for a discussion. 66

Figure 5.8. Probability density distribution (PDF) of the orientation angle of ellipsoidal Janus NPs of aspect ratio 4 adsorbed on a water droplet of diameter $d=40R_c$.

Panels (a) and (b) are for N=30 and N=70, respectively. Different lines are for different NP surface densities, A_c. 67

Abstract

Nanoparticles (NPs) can stabilize the so-called Pickering emulsions. These emulsions are used in many applications, including biofuel upgrading, material synthesis, food preservations and pharmaceutical processes. The fundamental understanding of the behavior of NPs adsorbed at oil/water interfaces is required to effectively utilize NPs for these and other applications. To this end, dissipative particle dynamics simulations were implemented and used herein. Various NP types, NP concentrations, and oil/water interfacial curvatures were systematically investigated. We found that the NP surface chemistry, NP shape, NP concentration at the interface, system composition, and curvature of the oil/water interface are all the key factors that can alter structural and dynamical properties of the NPs at interfaces. In some cases, evidence for emergent behavior has been documented. Among other interesting results, we found that when adsorbed at a flat oil/water interface, the averaged two-dimensional self-diffusion coefficient for a mixture of two types of spherical NPs of equal surface density is not a monotonic function of the NP composition. It was found that spherical Janus NPs are better at reducing interfacial tension than spherical NPs with homogeneous distribution of surface functional groups (homogenous NPs). For ellipsoidal Janus NPs it was found that the NP orientation with respect to the oil/water interface depends on the NP surface chemistry and aspect ratio. Ellipsoidal Janus NPs are more effective at reducing the interfacial tension than spherical NPs. An isotropic-nematic phase transition was observed for ellipsoidal Janus NPs with high aspect ratio as the NP surface density increased. Ellipsoidal NPs were found to yield isotropic, axial nematic, radial nematic, and isotropic phases with axial nematic domains, depending on

droplet diameter, NP surface density, aspect ratio and surface chemistry. In addition, we found that the NPs behavior at curved interfaces strongly depend on the liquid type. It was found that NPs with high aspect ratios and few surface nonpolar beads, when adsorbed on a water droplet, have two equilibrium orientation angles. This observation becomes more interesting when one considers that the same NPs adsorbed on an oil droplet show only one preferential orientation angle. When coupled with appropriate experimental observations, our findings could be useful for the advancement of all those applications in which Pickering emulsions could be used.

Chapter 1. Introduction

1.1.Emulsion Overview

Emulsions are formed when one liquid is dispersed into another immiscible liquid. Typical immiscible liquids are oil and water. Emulsions have been found in many applications including foods (salad dressings, deserts),[1,2] cosmetics (hand creams, lotions),[3] pharmaceuticals,[4] oil processing,[5,6] and biofuel upgrading.[7,8] It has been proposed to use emulsions in many other fields, including templates for material synthesis.[9-11]

1.2.Stability of Emulsions

The stability of emulsions refers to the ability to resist changes in their properties over time. There are many processes require long living emulsions. However emulsions are thermodynamically unstable, oil and water will separate rather quickly. The oil/water phase separation occurs under various ways, including sedimentation, coalescence, flocculation and Ostwald ripening.[12-15] Sedimentation occurs when the oil and water with different densities are separated by gravity.[13] The coalescence occurs when two droplets come into contact; the thin liquid films around the droplets are broken, resulting in the fusion of two contacting droplets.[14] This is considered as the most severe cause of emulsion instability. Flocculation involves the aggregation of the droplets.[12] This occurs when the repulsion between droplets is weak. The Ostwald ripening relates to the disappearance of the small droplets. This is because the difference in solubility between the small and the large droplets.[15]. As time passes, the molecules of the smaller droplets diffuse through the continuous medium and deposit onto the larger droplets causing phase separation.

1.3.Particles as Emulsifiers

1.3.1. Pickering Emulsions

To increase the stability of emulsions, emulsifiers are used. Perhaps, the most typical emulsifier is surfactants. These compounds will prevent or delay the phase separation when adsorbed at the droplet surfaces. Small particles (e.g., nanoparticles NPs) have been proposed to be used as emulsifiers over the last one hundred years.[16,17] The particle-stabilized-emulsions have been known as Pickering emulsions.[18] This topic has received tremendous attention over the last few decades. Several reasons can explain this increasing interest.

First, particle-stabilized emulsions offer some advantages over the traditional surfactant.[19-22] Surfactant stabilized emulsions cause some problems, including skin tissue irritation.[22] The viscosity of the Pickering emulsions can be easily adjusted by manipulating the types and concentration of NPs.[20] The surface chemistry of particles can be easily modified, yielding effective emulsifiers. [21] In addition, many emulsion systems naturally contain particles, including silica or clay in oil processing.[23,24]

Second, many applications related to Pickering emulsions have been explored.[8,11,25-30,11,28-33]These emulsions can be used as templates for advanced material synthesis.[11] The studies of particles adsorbed onto the interfaces give insights for other fields, including the crystal growth mechanism in crystallization.[29,30] Composite microcapsule and microspheres synthesis are based on Pickering emulsions.[26-28] Interfacial catalysts, in which the catalysts are adsorbed at the oil/water interface and catalyze reactions in both oil and water phases, are proposed to be used in biofuel

upgrading.[8,25] By using these catalysts, it is possible to control the desired reactions in both oil and water phases.

Finally, the novel development of particles provides many types of particles which can be effective emulsifiers. Silica particles can be made polar and nonpolar to stabilize oil-in-water (o/w) and water-in-oil (w/o) emulsions, respectively.[31,32] Inversion of emulsions (from o/w to w/o and vice versa) can be achieved by changing the composition of mixture of polar silica and nonpolar silica.[33] Polymer-grafted particles can be effective emulsifiers.[34-37] For example, poly (styrenesulfonate)-grafted silica NPs stabilize heptane-in-water emulsions with a very low concentration of particles (0.04 weight % particles).[37]

1.3.2. Pickering Emulsion Stabilization Mechanism

Although the Pickering emulsions have been widely used, the stabilization mechanisms are not totally understood.[14,38-45] It is widely accepted that particles kinetically stabilize emulsions. However, whether or not particles can thermodynamically stabilize emulsions is still in debate.[38,42]

1.3.2.1.Kinetic Stability

Kinetic stability relates to the presence of NPs on droplet surfaces and prevents coalescence.[40,44] Kinetically stabilized emulsions can be last for several months to years. Typically, particles will adsorb on the droplet surfaces, create steric layers and prevent droplet combination. This mechanism depends on the ability of particles to adsorb on droplet surfaces, which relates to desorption energy, and the interaction between particles.

a. Desorption Energy

To stabilize emulsions, particles must adsorb on droplet surfaces. This relates to the desorption energy of particle i.e., the energy required to remove particles from the interface into the bulk phase. Levine et al.,[40] found that desorption energy is strongly correlated to the stability of emulsions. It is difficult to break the particle layer and allow coalescence when the desorption energy is high. Consider a small spherical particle with a uniform surface chemistry, the detachment energy is calculated as:[41,43,45]

$$\Delta E = \pi r^2 \gamma_{ow}(1 \pm \cos\theta) \tag{1.1}$$

Here r is the radius of a spherical particle, γ_{ow} is the oil/water interfacial tension, θ is the three phases contact angle of particle at the interface, measured though the water phase. Inside the bracket, the plus (minus) sign is for particle desorbs into the oil (water) phase.

The desorption energy depends on particle contact angle and size (see Figure 1.1). The results from this figure suggest that particles must have appropriate contact angle and size in order to stabilize emulsions. The smaller particles offer higher packing efficiency, thus yielding higher stability emulsions.[32,46,47] However, too small particles have too small desorption energy. Such particles are not strongly pinned to the interface to stabilize emulsions. In general, to successfully stabilize emulsions, the size of particles must range from a few nanometers to a micrometer.[46-48]

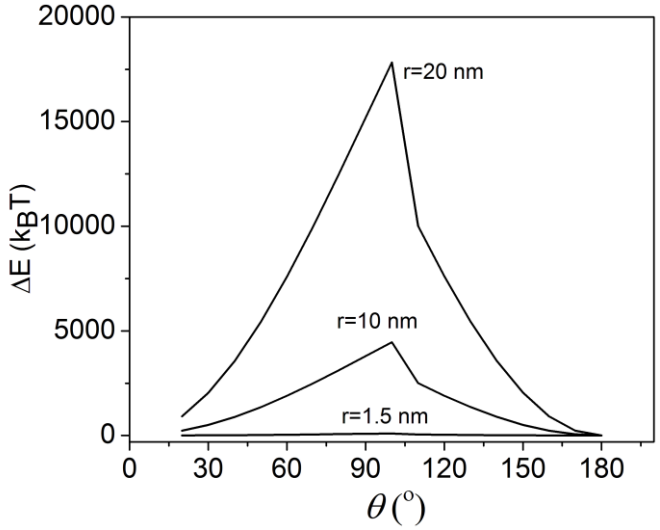

Figure 1.1. Desorption energy of a particle as a function of contact angle at various particle radius.

Peoples also found that particles with small contact angle ($\theta < 30°$) or large angle ($\theta > 150°$) may not stay at the interface because the desorption energy is small. Such NPs, in principle, are not able to stabilize emulsions. For other values of contact angle, it is suggested that NPs with $\theta < 90°$ stabilize oil-in-water (o/w) emulsions while NPs with $\theta > 90°$ stabilize water-in-oil emulsions (see Figure 1.2).

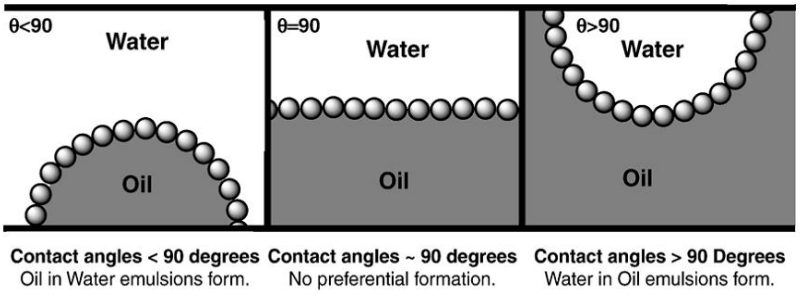

Figure 1.2. Bending behavior of emulsion droplets coated in particles[43]

b. Particle-Particle Interaction

Because desorption energy of a particle is rather large, the adsorption of particles on the oil/water interface is considered irreversible. It is believed that adsorbed particles generate a steric barrier to prevent the coalescence.[45,49] As two droplets covered by particles approach each other, the adsorbed particles on the two closest regions of two droplets begin to interact. The effective repulsion between droplets depends on the interaction between NPs.[44,50] The particle-particle interactions also affect the network structures of particles on the droplet, which have great effect on coalescing.[51]

1.3.2.2.Thermodynamic Stability

Whether particles thermodynamically stabilize emulsions is a question that needs further investigations. The thermodynamic stabilization of emulsions is related to the free energy of emulsion formation, ΔG. Without NPs, ΔG is always positive because the emulsion formation process creates new interfaces. Therefore, bare emulsions are thermodynamically unstable.

The presence of particles can lower ΔG, and sometimes makes ΔG negative, yielding thermodynamically stabilized emulsions. One possible way that particles can lower ΔG come from the contribution of adsorption energy which is negative.[38,52] This energy has the same magnitude but opposite sign with desorption energy. To make ΔG negative, the magnitude of adsorption energy must be high. It is suggested that some Janus particles might have this ability. Robert Aveyard[38], using theoretical calculation, suggested that ΔG of emulsions stabilized by spherical Janus particles is negative. This research is supported by the recent research done by Lee et al.,[42] who found that the

Janus Dumbbells can offer thermodynamically stabilized emulsions. Indeed the calculated free energy of emulsion formation is negative.

1.4.Parameters Affecting the Stability of Pickering Emulsions.

Regarding the discussion on the mechanisms of Pickering emulsion stabilization, the stability of emulsions depends on the structure of the NP layers and the interaction between particles. Such properties were found to depend on a number of factors, including the nature of particles (e.g. contact angle, size and shape) and the operation conditions (e.g. particle concentration and composition).

1.4.1. Particle Characteristics

a. Particle Surface Chemistry

Both the nature of particle surface function groups and their distribution have been found to have great effect on emulsions. Bink et al.,[52] theoretically calculate the adsorption of homogeneous and Janus particles at the oil/water interface. He found that Janus particles are pinned more strongly at the o/w interface than homogeneous particles. He also suggested that Janus NPs are more efficient in stabilizing emulsions.

b. Shape of Particles

The shape of particles was found to be an important factor influencing the stability of emulsions. Non-spherical particles (ellipsoids, dumbbells, rods) can create orientation angles with respect to the o/w interface, leading to complex structures of particles.[53-55] This will affect the mechanism that particles stabilize emulsions. For example, Boode and Walstra[56] found that the protruding crystals tend to form a bridge between two droplets in coalescing process. This does not occur for crystals which are

oriented parallel to the interface. Madivala et al.,[57] mentioned that hematite ellipsoidal NPs with small aspect ratios are not able to stabilize o/w emulsions. However, when the aspect ratio is high, such NPs can stabilize emulsions. It has been reported that the minimum amount of nanorods needed to stabilize an emulsion decreases when the length of nanorods increases.[58] The shape of particles has a great effect on the particle structure, interfacial rheology, which are important factor affecting emulsion stability.

1.4.2. Operation Conditions

a. Oil Type

When particles with $\theta \sim 90°$ are used, the property of emulsions depends on the volume fraction of solvents, the initial phase where particles are introduced, and the oil type.[32,33,59] For example, toluene-water mixtures, w/o emulsions were formed when silica particles are initially dispersed in oil while o/w emulsions are preferred when NPs are dispersed in water.[59] It was also suggested that silica particles with intermediate hydrophobicity stabilize o/w emulsions when oils are nonpolar (e.g., hydrocarbons) and stabilize w/o emulsions when polar oils were used (e.g., fatty acid and ester). This was supported by Frelichowska et al.,[60] who used bare silica particles (polar surface) to stabilize o/w emulsion when oil is polar oil.

b. Particle Concentration

The concentration of particles is an important factor governing the stability and many aspects of emulsions. Tambe and Sharma[41] suggested that particles must cover all the droplet interface in order to prevent coalescence This idea is supported by Frelichlowska et al.,[60] who found that the stability of o/w emulsions increases with

increasing silica particle concentration. However, some reports have demonstrated that sometimes emulsions can be stabilized by particles at low concentration.[51,61] For example, Vignati et at., [51] showed that silica particles can stabilize emulsions at concentration only ~15% of a dense monolayer.

1.5.Liquid Crystals

Liquid crystal materials have properties from both liquid and solid phases.[62] The distinguishing characteristic of these materials is the orientational order i.e. the non-spherical molecules have one common direction. This is different with liquid phases, which have no intrinsic order, and with solid phases, which have high order. When non-spherical particles adsorb on the oil/water interface, they can have orientational order, depending on particle designs (e.g. aspect ratio, surface chemistry), particle surface density and the curvature of the oil/water interface. The orientational order of the particles is expected to have great effect on utilizing particles, for example, designing optical and electrical devices.

1.6.Research Objectives

Despite this wealth of research, there are a number of unsolved questions. In this thesis, we address three problems,

(i) We quantify the structural and dynamical properties of particles adsorbed at the oil/water interface. The particles can be either similar or a mixture of two types of particles.

(ii) We access the structures and the emergent behavior of ellipsoidal Janus particles when they are adsorbed at the flat oil/water interface.

(iii) We investigate the ellipsoidal Janus particles assembled on the droplet interfaces.

We used dissipative particle dynamics simulations to investigate the behavior of NPs adsorbed at the oil/water interface (see chapter 2). We used particles with different surface chemistries (i.e. polar and nonpolar) and shape (i.e. spherical and ellipsoidal shapes). Various operation conditions are considered, including heterogeneous mixture of particles, particle concentration and the curvature of the oil/water interfaces. In chapter 2 we discuss about the simulation method. In chapter 3 we present the structural and dynamical properties of systems of NPs with different surface coverage and composition. In chapter 4, we focus on the interfacial tension reduction, the network structures, and the emergent behavior of ellipsoidal Janus particles when adsorbed at the flat oil/water interface. In chapter 5, we remove the flat oil/water interface constraint. We assess the structures of ellipsoidal particles assembled at spherical oil/water interfaces. Finally, we summarize our main findings in chapter 6.

Chapter 2. Simulation Methodology

To investigate the property of the system, the molecular dynamics (MD) simulation is often used. The Newton's equation of motion is implemented in this method to find the trajectories of atoms and molecules. The interactions between atoms (molecules) can be Lennard-Jones, van der Waals, and electrostatic forces. This method is appropriate for small systems where the number of atoms (molecules) is small. However, it is difficult to use MD simulation to simulate complex systems because (i) the number of calculation is too large, and (ii) long MD simulation may generate cumulative errors in numerical integration.

All the simulations in this thesis are considered big systems, and the MD simulation cannot be employed. We use dissipative particle dynamics (DPD) method. This method is considered a coarse graining model of MD simulation. It reduces the number of calculations by grouping some atoms (molecules) into one group, which is called bead. There are three kinds of interaction forces in the DPD systems, namely, conservative, dissipative, and random forces. The conservative force is the interaction between DPD beads. It is calculated to ensure the compressibility of the fluids inside the system. Dissipative force is to account the energy lost due to the frictional force inside bead. Random force is taken into account because we lost degrees of freedom by grouping the molecules. Detailed descriptions of the DPD formalism are available in the literature.[39,63,64]

Dissipative particle dynamics simulations were performed using LAMMPS.[65] In our simulations water and oil are present. One water bead represents 5 water molecules.

Following our prior work,[44,66] the oil is intended to represent decane. Two 'oil' beads, connected with one harmonic spring, represent one decane molecule. Inspired by Zerbetto and coworkers,[67] each nanoparticle is modeled as a hollow rigid NP. We used polar (p) and non-polar (ap) beads, we changed their ratio and their distribution on the NPs surface. The scaled liquid density is set to 3, and the scaled mass of each bead (oil, water, as well as NP beads) is set to 1. The self-interaction parameters, derived from the fluids compressibility, were calculated following Groot and Warren.[68] The interaction parameter between water beads and oil beads reproduces the water-decane interfacial tension, as described previously.[44,66,69] The nanoparticle-solvent interaction parameters were parameterized to reproduce the contact angle obtained via MD simulations for one silica NP at decane-water interface.[69] The NP-NP interaction parameters differ somewhat compared to those used in our previous work.[44,66] Specifically, the interaction parameters between NPs polar and non-polar beads were adjusted to ensure that NPs are able to assemble and disassemble without yielding permanent dimers at the water/oil interface. All DPD parameters are given in **Table 2.1**.

Table 2.1. DPD interaction parameters expressed in $k_B T / R_c$ units. Symbols 'w', 'o', 'ap', and 'p' are for water beads, oil beads, NP non-polar beads, and NP polar beads, respectively.

	w	**o**	**ap**	**p**
w	131.5	198.5	178.5	110
o		131.5	161.5	218.5
ap			450	670
p				450

All simulations were carried out in the NVE ensemble.[70] The scaled temperature is 1, equivalent to 298.73 K. The DPD time scale $\tau = 7.6 ps$ is obtained by fitting the self-diffusion coefficient of water in DPD simulation to the experimental water self-diffusion coefficient.[68]

Chapter 3. Nanoparticles Adsorbed at the Water/Oil Interface: Coverage and Composition Effects on Structure and Diffusion

The material presented in this chapter was published in 2013 in Langmuir, Volume 29.

3.1. Abstract

Dissipative particle dynamics simulations are performed to study the structural and dynamical properties of various systems of nanoparticles accumulated at the water/oil interface. Homogeneous and Janus nanoparticles with different surface compositions are studied. For all nanoparticles, as the surface density increases, a transition from liquid-like to solid-like state is observed, as expected. At high density of nanoparticles, hexagonal structures emerge and the nanoparticles self-diffusion coefficient decreases due to caging effects. Similar results are observed for nanoparticles with different surface chemistry. Because different nanoparticles have different contact angles at the water/oil interface, more interesting are the results obtained for systems containing mixed nanoparticles. For example, our results show that the self-diffusion coefficient is not a monotonic function of the system composition, caused by the complex relation between hydrodynamic interactions and effective nanoparticle-nanoparticle interactions.

3.2. Introduction

Pickering emulsions,[71] stabilized by nanoparticles (NPs) adsorbed at liquid-liquid interfaces, have found applications in crude oil recovery,[72,73] biofuel processing,[74]

cosmetics, encapsulation for drug delivery,[75] food preservation,[76,77] etc. To further develop these applications the influence of NPs interfacial behavior on emulsion stability needs to be clarified.[78]

Many experimental efforts described the structure of NP monolayers at interfaces.[43,79-84] Bink et al.[80,81] investigated the packing of NPs at the air-water interface finding that the compression elastic modulus can reach a maximum when the contact angle is ~ 90°. NP size and contact angle affect adsorption isotherms and interfacial tension.[82] It has been shown that Janus NPs are more effective in reducing the interfacial tension than homogeneous NPs with similar over-all chemical composition.[79] Interfacial systems containing both surfactants and NPs have also been investigated, sometimes showing competing phenomena.[85,86]

Besides the structure of NP monolayers, the NPs diffusion also affects the system stability.[87-93] The NPs diffusion at interfaces depends on surface coverage,[92] hydrodynamic and effective NP-NP interactions.[88] The effect of fluids viscosity on the NPs diffusion remains elusive,[89,87] and 'caging' effects that can slow the NPs diffusion have been reported at high NP coverage.[90]

Simulation studies aid the interpretation of experimental observations.[44,66,68,69,85,92,94-107] Using molecular dynamics (MD), for example, Dai and coworkers discussed competing phenomena when NPs and surfactants adsorb at the oil-water interface.[96-98] Larger systems can be studied with coarse-graining techniques, with the shortcoming of losing some atomistic details.[103-107] For example, Fan and Striolo implemented dissipative particle dynamics (DPD) to investigate (a) the mechanism of droplets coalescence ,[44] and (b) the interfacial tension[66] in the presence of NPs.

Following this line of research, in the present manuscript we use DPD simulations to quantify structure and dynamics of NPs at a water-oil interface as a function of NP type and surface coverage. As opposed to most of the studies available in the literature, particular emphasis is given here to mixed systems. In the remainder of this article we first discuss the simulation methodology, including some differences compared to our prior attempts; we discuss the results (first for homogeneous systems, then for mixtures); and finally we summarize our main findings.

3.3. Simulation Methodology

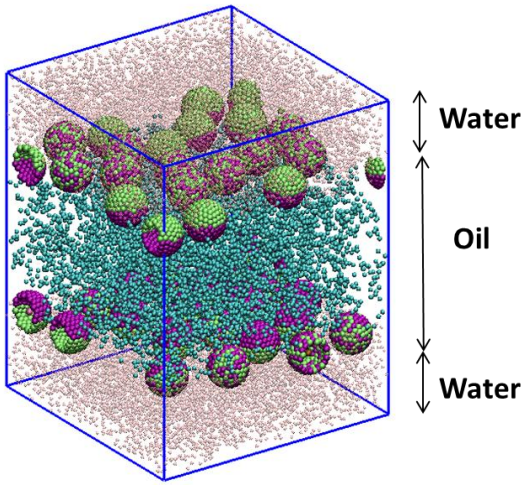

Figure 3.1. Representative simulation snapshot for the systems considered in this work. A biphasic system containing water and oil is considered. Pink and cyan beads represent water (w) and oil (o), respectively. At the conditions considered water and oil yield two planar interfaces, where several nanoparticles (NPs) adsorb. The number of NPs adsorbed on one interface equals that adsorbed on the other interface. Purple and green beads represent non-polar (ap) and polar beads (p) on the NPs, respectively. In the specific case considered in this snapshot 50% of the NPs are homogeneous (50HP) and 50% Janus (50JP). Details on NPs type are given in **Figure 3.2.**

In **Figure 3.1** we present the typical setup considered in our simulations. In each of the systems simulated, water and oil demix, and nanoparticles (NPs) adsorb at the water-oil interface, always planar. Because of periodic boundary conditions, two

interfaces are present within one simulation box. An equal number of NPs are adsorbed on both interfaces. No NPs are present within the bulk water and/or oil phases. The simulation system size is $L_x \times L_z \times L_z \cong 30 \times 30 \times 40 R_c^3$, where R_c is the cutoff radius in the DPD formalism, and L_i is the length of the simulation box along the i direction. Orthorhombic boxes are used.

Each NP is modeled as a hollow rigid sphere with 192 beads on the surface and 1 bead at the center. The NPs have radius $2R_c$ (~ 1.5nm). We used polar (p) and non-polar (ap) beads, we changed their ratio and their distribution on the NPs surface. We considered homogeneous NPs, abbreviated as 'HP', on which the chemical groups are randomly distributed on the NP surface, and Janus NPs, denoted by 'JP', on which beads of one type are segregated on one face of the NP. In our notation, the number (i.e., 25, 50, and 75) before 'HP' or 'JP' indicates the fraction of non-polar beads on the NP surface. In 25HP NPs, e.g., 25% of the surface beads are non-polar. The NPs considered are represented schematically in **Figure 3.2**.

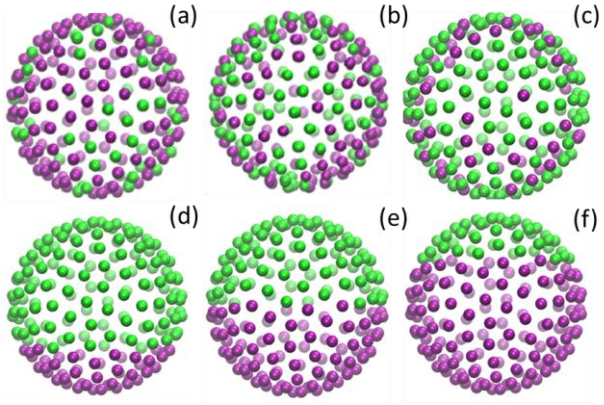

Figure 3.2. Schematic representation of the NPs simulated in this work. Different panels represent different NPs: panel (a) is for 75HP; (b) for 50HP; (c) for 25HP; (d) for 25JP; (e) for 50JP; and (f) for 75JP NPs. Purple and green beads are non-polar (ap) and polar (ap), respectively. HP and JP indicate homogeneous and Janus NPs, respectively.

In **Table 3.1** we report the averaged contact angles obtained during our DPD simulations for the various NPs at the water-decane interface. The data reported are averaged over all the NP surface densities considered. In general, the contact angle does not change with surface density of NPs. The θ standard deviations for Janus NPs are smaller than those for homogeneous NPs with the same overall surface composition. This suggests that the Janus NPs fluctuate less in the direction perpendicular to the interface (they are more strongly pinned to the interface). Based on our earlier studies,[44] this observation might suggest that Janus NPs could be better capable of stabilizing Pickering emulsions than their homogeneous counterparts.

Table 3.1. Three-phase contact angle θ obtained from DPD simulations. Data are averaged over all surface densities considered in this work for simulations with one NP type.

	75HP	50HP	25HP	25JP	50JP	75JP
Contact angle θ (^{o})	77	58	37	44	81	82
Standard deviation	5.9	7.2	12.8	6.2	4.2	4.9

3.4. Results and Discussion

Our results, both for single NPs and for mixed NP systems, are quantified as a function of the NPs surface coverage, which is defined as:

$$\phi = n * \pi d^2 / 4A \quad . \qquad (3.1)$$

In Eq. (3.1), *n* is the number of NPs absorbed at the interface, *A* is the surface area (correspondent to the simulation box area parallel to the interface), and *d* is the shortest distance between two NPs, as obtained from the first peak in radial distribution functions (described later).

3.4.1. Single-NP Systems

The interfacial tension γ as a function of NPs surface coverage ϕ is calculated as:[108]

$$\gamma = \left\langle P_{zz} - \frac{P_{xx} + P_{yy}}{2} \right\rangle \frac{L_z}{2} \tag{3.2}$$

.

In Eq. (3.2), P_{ij} is the *ij* element of the pressure tensor, L_z is the simulation box length in the z dimension, and angular brackets denote ensemble averages. The results are shown in **Figure 3.3**.

In qualitative agreement with results obtained with the 'micro-Wilhelmy plate' algorithm, reported previously,[66] our results suggest that NPs reduce the interfacial tension only when their surface coverage is significant, which is expected to yield strong NP-NP repulsions. Hórvölgyi[109] and Stirner[110] pointed out that NP-NP repulsion yields a large contribution to the pressure tensor in Eq. (3.2). Our results are consistent with some experimental results,[111,112] including the reduced surface pressures reported as a function of coverage for particle-laden interfaces.[113]

Out of the particles considered here, the 50JP NPs show the highest capability of reducing the interfacial tension, which is consistent with prior results.[66] At high ϕ, the interfacial tension decreases much faster for 50JP than 50HP NPs, while the difference between 75HP and 75JP NPs, or that between 25HP and 25JP NPs, is not obvious, probably because these NPs yield similar contact angles.

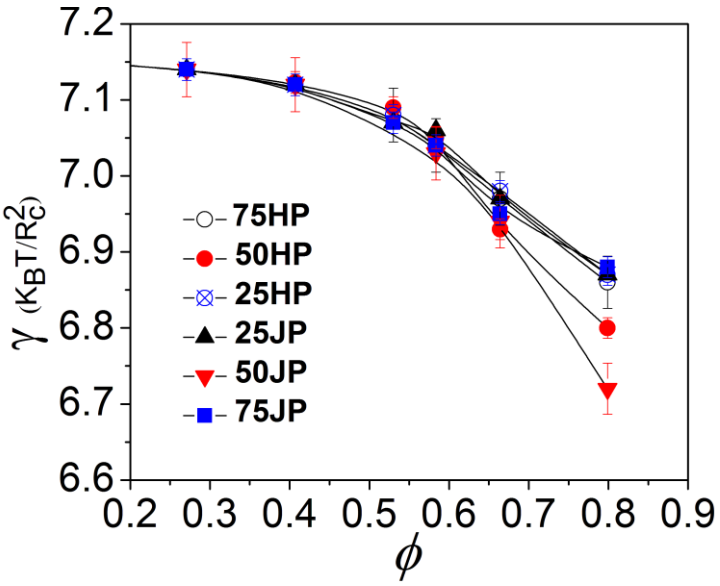

Figure 3.3. Interfacial tension as a function of surface coverage for various NPs at the water/oil interface. Only one type of NP is present in each of the systems considered. Symbols are simulation results. The error bars represent one standard deviation from the average. Lines are guides to the eye.

To quantify the structure of NPs at interfaces we computed the order parameter ψ_6 [114,115] as a function of surface coverage. The order parameter is obtained as:

$$\psi_6 = \frac{1}{N_t}\sum_{l=1}^{N_t}\left|\frac{1}{N_P}\sum_{j=1}^{N_P}\frac{1}{6}\sum_{1}^{N_J}\exp(i6\theta_{jk})\right| \qquad (3.3)$$

In Eq. (3.3), i is the imaginary unit; N_t and N_p are the number of frames used for the calculations, and the number of NPs present at the interface, respectively; θ_{jk} is the angle between the vector joining NPs j and k and an arbitrary reference axis. For every NP j, only NPs within one NP diameter were considered as candidates for calculating ψ_6 (next-neighboring NPs). The order parameter ψ_6 is sensitive to local hexagonal order. For liquid-like disordered structures, ψ_6 approaches zero, while for hexagonal structures $\psi_6 = 1$.

In our results (**Figure 3.4**) ψ_6 increases with the surface coverage, following a trend opposite than that, but reminiscent of the one discussed for the interfacial tension. The slope change in Figure 3.4 might suggest a disorder-to-order phase transition from low to high densities, which is reflected in Figure 3.3. These results are consistent with experimental observations from Okubo,[116] who reported reductions in interfacial tension for systems in which the NPs organize in crystalline structures at the interface, but not when the NPs show liquid-like structures.

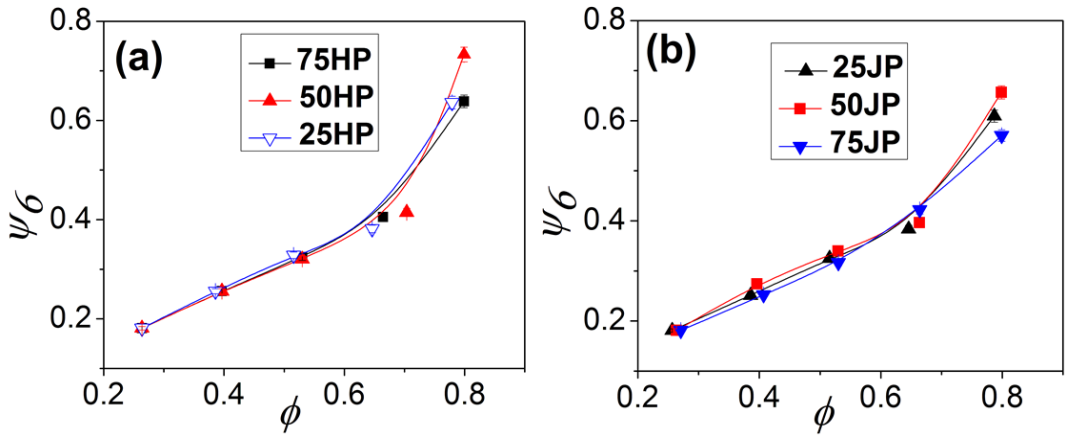

Figure 3.4. Six-bond orientational order parameter obtained for different NPs as a function of surface coverage. Panels (a) and (b) are for homogenous and Janus NPs, respectively. Error bars are obtained as one standard deviation from the average. Lines are guides for the eye.

To further characterize the NPs structure at the interfaces we calculated 2-dimensional radial distribution functions *g(r)*, shown in **Figure 3.5**. For brevity, we only report results for 4 NP types, i.e., 75HP, 25HP, 50HP, and 50JP NPs, in Figures 3.5a, 3.5b, 3.5c, and 5d, respectively. In each case, we consider 4 representative surface coverages, i.e., 0.26, 0.53, 0.66, and 0.79.

The RDFs are consistent with a low-density fluid at low NP coverage, and with a more structured phase at high density. For all NPs the results show many peaks, which can be grouped in those representing the first and second neighboring shells, respectively. Within each shell (e.g., peaks at distances less than 7 Rc for the first shell), the individual peaks are separated by intervening solvent beads packed in between the NPs. The solvation layers decrease as the NPs surface density increases. Although it is possible that, for example, water molecules yield long-lived layered structures near a solid substrate,[117,118] the pronounced structuring at short NP-NP separation in our RDFs is most probably an artifact of the simulation methodology. However, the transition between a disordered low-density to an ordered NP aggregate is consistent with experimental observations. In **Figure 3.6** we report representative simulation snapshots to illustrate the disordered NPs aggregate obtained at low density (left panel) and the hexagonally ordered aggregate obtained at high density (right). In the right panel note that the NPs are sometimes separated by one layer of solvent beads (lower right corner), and some other times by two-three layers of solvent beads (upper left corner). The similarity between RDFs obtained for different NPs types suggests that excluded volume effects, rather than details in NP-NP interactions due to the surface chemical properties, are the driving forces for the observed structural results for NPs at water-decane interfaces.

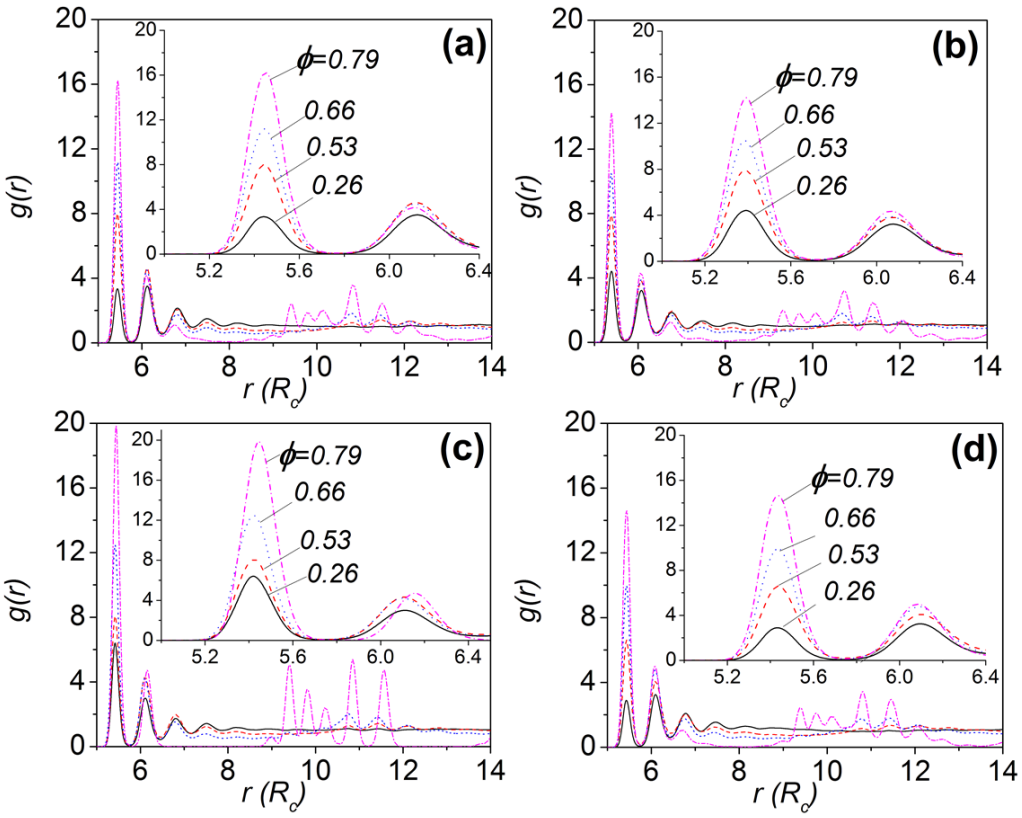

Figure 3.5 Two-dimensional radial distribution functions *g(r)* obtained for various NPs at increasing the NP surface coverage. Panels (a), (b), (c), and (d) are for 75HP, 25HP, 50HP, and 50JP NPs, respectively. The insets are enlargements at short NP-NP distances. Results are obtained at increasing surface density.

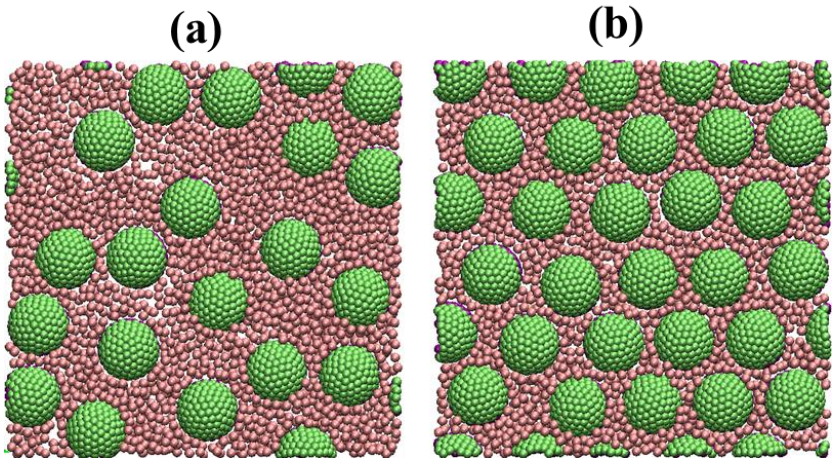

Figure 3.6. Top view of representative simulation snapshots obtained for 50JP NPs assembled at the water-oil interface. Panels (a) and (b) are for surface coverage 0.53 and 0.79, respectively. The results are representative of disordered liquid-like structure and of ordered hexagonal structure, respectively.

We quantified the NPs in-plane self-diffusion coefficient from the two-dimensional mean square displacement.[87] The NPs mobility depends on the viscosity of both liquids at the interface, although the mechanism remains elusive.[87] The NPs diffusion also depends on direct NP-NP interactions, especially when the NP density is large enough to generate 'cages' around each individual NP.[90] As the NP coverage increases hydrodynamic effects become coupled with NP-NP and NP-solvent correlations. In some cases it has even been reported that hydrodynamic interactions can enhance the NPs self-diffusion coefficient.[88]

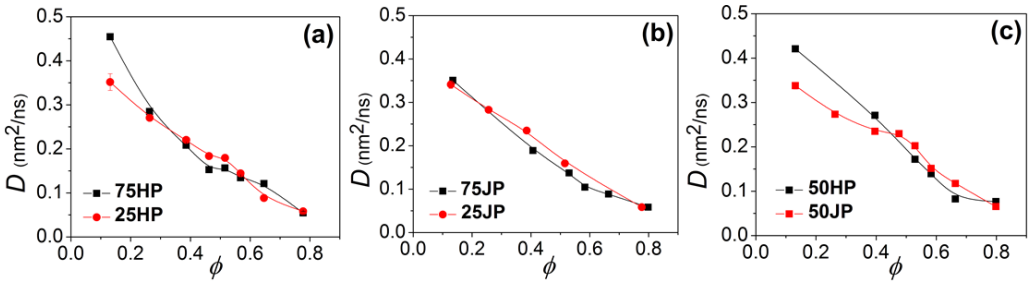

Figure 3.7. Self-diffusion coefficient as a function of surface coverage for various NP types. Panels (a), (b), and (c) compare 75HP and 25HP, 75JP and 25JP, and 50HP and 50JP NPs, respectively. Error bars, one standard deviation from the average, can be smaller than the symbols. Lines are guides for the eye.

In **Figure 3.7** we compare the in-plane self-diffusion coefficients obtained for 75HP and 25HP NPs (panel a), 75JP and 25JP NPs (b), and 50HP and 50JP NPs (b). For each NP type we report the self-diffusion coefficient as a function of surface coverage. In all cases at low ϕ the diffusion coefficients decrease almost linearly as ϕ increases**,** which has been observed by others.[87,119] Our results suggest that, at low coverage, $D_{75HP} > D_{25HP,}$ $D_{75JP} \sim D_{25JP}$ and $D_{50HP} > D_{50JP}$. These differences might be explained in terms of NP-solvent interactions, which are due to a combination of the contact angle and to

the composition of the NP surface. For example, the 75HP NPs contain a significant number of non-polar beads on their interface, while the 25HP NPs contain many polar beads. Both 75HP and 25HP NPs are immersed into the aqueous phase (contact angle < 90°). Because the interactions between polar (non-polar) NP beads and water (oil) beads are less repulsive than those between polar (non-polar) NP beads and oil (water) beads, the hydrodynamic resistance is expected to be larger for 25HP than for 75HP NPs, leading to slower diffusion ($D_{25HP} < D_{75HP}$). Similar observations qualitatively explain the differences in NPs diffusion shown in Figs. 3.7b and 3.7c.

As the coverage increases, the diffusion coefficients do not depend strongly on the NPs type. At these conditions NP-NP interactions influence the self-diffusion coefficient. Comparing the two-dimensional RDFs to the self-diffusion coefficients we observe that when the RDF peaks are more intense and closely packed (indicative of strong NP-NP attraction), the self-diffusion coefficient is lower. At high NP coverage it is possible that the NPs are trapped in cages formed by neighboring NPs. To quantify this possibility we calculated the scaled vector-vector correlation function:[120]

$$V(\Delta t, t) = \frac{1}{\Delta r^2}\left\langle \frac{1}{N_t - t}\sum_{j=1}^{N-t}\frac{1}{N_p}\sum_{i}^{N_p}(r_j(\Delta t).r_{j+t}(\Delta t))\right\rangle \quad . \qquad (3.4)$$

In Eq. (4), Δt is the time interval used to define the vector at any time t. In our calculations Δt = 0.6 τ (see Methods section for the DPD time scale τ). The autocorrelation function is calculated as a function of time t. The mean square displacement Δr^2, was also calculated as a function of time to compare results obtained at different surface coverages. *V* decreases as time progresses, and it might become negative if a NP changes directions, e.g., when it rebounds inside a cage.

Representative results for the autocorrelation function V as a function of time are reported in **Figure 3.8**. For 75 HP NPs (Figure 3.8a), the autocorrelation function decays slowly from 1 to 0 at low surface coverage, due to rare encounters between different NPs. As the surface coverage increases the autocorrelation function decays rapidly to 0, because more NP-NP encounters lead to frequent changes in the direction of NP motion. When the surface coverage is above ~0.53, the autocorrelation function decays to negative values, and then gradually increases to zero, suggesting the formation of cages. In panel (b) of **Figure 3.8** we report results obtained for six different NPs at surface coverage 0.66. In all cases the autocorrelation function is indicative of caging effects. The minima in the autocorrelation functions depend on the NP type, with $V_{75HP} < V_{25HP}$; $V_{75JP} < V_{25JP}$; $V_{50HP} < V_{50JP}$, which might be related to the self-diffusion coefficients at large surface coverage. Comparing our results, caging effects appear at coverages sufficient to yield hexagonally ordered NP structures and reduce the water-oil interfacial tension.

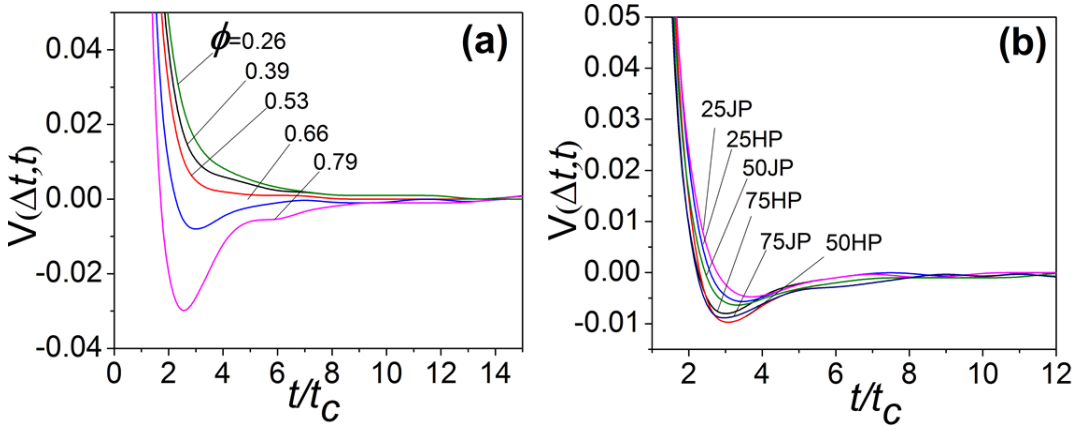

Figure 3.8. Vector-vector autocorrelation function (Eq. (3.4)) as a function of time for 75HP NPs at various surface coverages (panel a), and for six different NPs at surface coverage ϕ =0.66 (panel b).

3.4.2. Mixed NPs Systems

We quantify structure and dynamics of three mixed NP systems, each composed by two NP types. The three 'mixtures' considered contain (1) 75HP and 25HP NPs; (2) 75JP and 25JP NPs; and (3) 50HP and 50JP NPs. We report the composition of the various systems using the variable x, which represents the fraction of the first type of NPs with respect to the total number of NPs in each mixture. For example, in mixture #1, x represents the fraction of 75HP NPs with respect to the sum of 75HP and 25HP NPs. The total surface coverage is maintained at 0.53.

The RDF results for the mixed systems (Figure 3.9), indicative of dense fluid structures, are qualitatively similar to those reported in Figure 3.5. Compare to the single-NP systems, the NPs can sometimes get closer to each other in mixed systems because of the different contact angles of two NPs. Such geometric effects are responsible for small changes in the first RDF peak position and intensity as a function of mixture composition. For example, in the case of 75HP/25HP mixture, as the fraction of 75HP NPs increases, the first RDF peak (at ~5.5) first decreases in intensity and shifts to shorter distances, and then it increases in intensity and shifts to larger distances. This occurs because when the 75HP NPs are a small fraction of those present, the mixed RDF reflects the features obtained for the pure 25HP NPs; vice versa, when the 75HP NPs are most of those present in the system, the mixed RDF reflects the features obtained for the pure 75HP NPs. When both NPs are present in ~ equal amounts, the mixed RDFs reflect the possibility of two different NPs to get closer to each other than expected based on their diameter because of the different contact angles. Similar observations as those just summarized are obtained for the 75JP/25JP NPs mixture. For

the 50HP/50JP mixture, the peak positions observed in the mixed RDF results do not shift significantly as the system composition changes because the two NPs have similar contact angles.

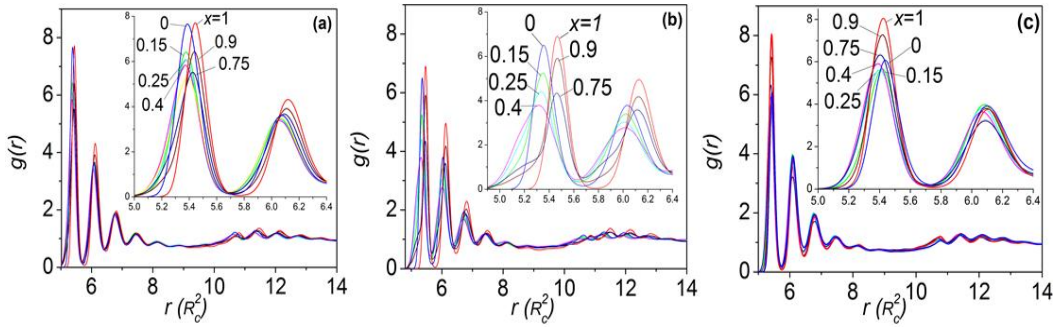

Figure 3.9. Two-dimensional radial distribution functions *g(r)* for the three NP mixtures considered in this work. In all cases the total surface coverage is ϕ=0.53. From top to bottom, the three panels are for 75HP and 25HP NPs, 75JP and 25JP NPs, and 50HP and 50JP, respectively. For each mixture, results are obtained at various compositions, expressed by 'x', as indicated in the panels.

We also evaluated the averaged self-diffusion coefficient for the NPs within the three mixtures, as a function of the mixture composition. It is worth repeating that the surface coverage is in all cases $\phi \cong 0.53$. The results for the self-diffusion coefficients are shown in **Figure 3.10**.

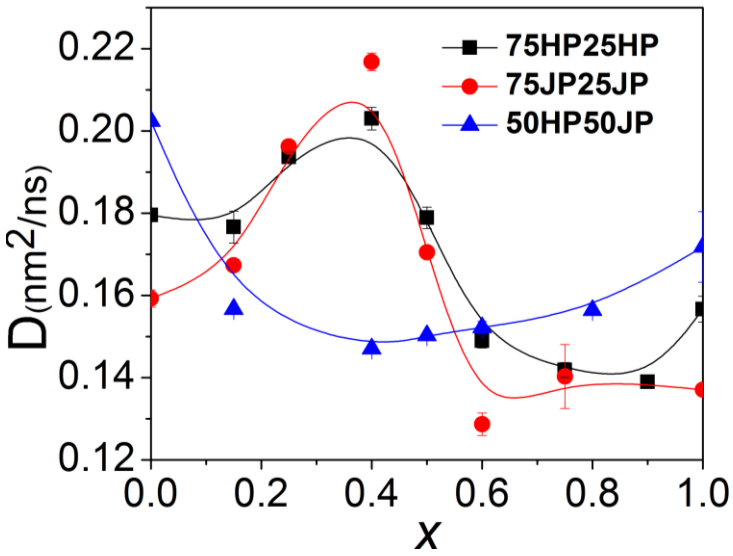

Figure 3.10. Averaged two-dimensional self-diffusion coefficient obtained for NPs in the three mixtures considered in Figure 3.9. In all cases $\phi = 0.53$ but the mixture composition changes systematically. The variable *x* represents the fraction of 75HP NPs in mixture 1 (composed by 75HP and 25HP NPs), that of 75JP NPs in mixture 2 (composed by 75JP and 25JP NPs), and that of 50HP NPs in mixture 3 (composed by 50HP and 50JP NPs). Lines are guides for the eye.

The averaged self-diffusion coefficient results show a pronounced non-monotonic behavior. The self-diffusion coefficient obtained for NPs in mixtures 1 and 2 shows a clear maximum at x~0.4, while the self-diffusion coefficients obtained for NPs in mixture 3 show a minimum at similar composition. These differences are probably due to changes in NP-NP packing as the composition changes. In mixtures 1 and 2 the contact angle for the two NP types present in the mixture is different (see Table 3.2). It is possible that when x~0.4 there is less 'compatibility' between the NPs aggregated at an interface, which leads to enhanced diffusion. These results are consistent with the lower intensity in the RDF peaks at short NP-NP separation observed for x~0.4 (indicative of weaker NP-NP attraction). In mixture 3, the contact angle of the two NPs is similar, and the RDF peak position does not change as the composition changes.

Changes in the intensity of the first RDF peak might reflect subtle changes in preferential packing between the NPs at the interface, which might result in the lower mobility observed at x~0.4

In the case of single NPs, we explained changes in the diffusion coefficient based on the autocorrelation function of **Figure 3.8**. Although when the surface coverage is 0.53 we do not expect caging effects (negative values in the autocorrelation function), the time required by the autocorrelation function to decay from 1 to 0 might be representative of NP-NP interactions. Our results (not shown for brevity) suggest that for mixture 1 and 2 the vector-vector autocorrelation function at x=0.4 is the slowest to decay to zero, while for mixture 3 the autocorrelation function at x=0.4 is the fastest to decay to zero. Because NP-NP collisions are responsible for the decay in the vector-vector auto-correlation function, this qualitative observation suggests that the effective free volume available for each NPs is larger at x~0.4 in mixtures 1 and 2, and smaller in mixture 3, possibly explaining the non-monotonic effects observed for the averaged self-diffusion coefficients shown in Figure 3.10.

3.5. Conclusions

The structure and diffusion of nanoparticles at an oil/water interface were investigated using dissipative nanoparticle dynamics simulations. We found that the interfacial tension reduces significantly only when the surface coverage is large enough that repulsive NP-NP interactions are expected. In correspondence to significant reductions in interfacial tension, our results suggest the formation of ordered hexagonal structures for all nanoparticles considered. These ordered structures also affect the nanoparticles mobility. The nanoparticle self-diffusion coefficient is high at low surface

coverage, and quickly decreases as the surface coverage increases. At high surface coverage all nanoparticles exhibit reduced mobility because of caging effects. When mixtures containing two nanoparticle types are present, our results show some differences in the packing structure, which can be for the most part explained by the contact angles of the individual nanoparticles, and pronounced differences in the averaged self-diffusion coefficient. As the composition changes while the surface coverage is maintained constant (yielding dense-liquid structures) it is possible to observe both minima and maxima in the averaged self-diffusion coefficient for the nanoparticles. These trends can be explained, at least qualitatively, by changes in the effective excluded volume available to each NP, which depends on the contact angle of the NPs in the mixture and on effective NP-NP interactions. Because both the packing and mobility of the nanoparticles at liquid-liquid interfaces are known to affect the stability of Pickering emulsions, our results suggest that tuning the composition of the particles used is an additional parameter that could be used to improve those applications for which Pickering emulsions are important (drug delivery, cosmetics, and others).

Chapter 4. Ellipsoidal Janus Nanoparticles Adsorbed at the Water-Oil Interface: Some Evidence of Emergent Behavior

The material presented in this chapter was published in 2013 in the Journal of Physical Chemistry B, Volume 117.

4.1. Abstract

The equilibrium behavior of ellipsoidal Janus nanoparticles at water-oil interfaces was investigated using dissipative particle dynamics simulations. It was found that the orientation of the nanoparticles with respect to the interface depends on nanoparticle aspect ratio, on the amount of polar vs. nonpolar surface groups, and on the interactions between the nanoparticles surface groups and aqueous and non-aqueous solvents. The changes in nanoparticle orientation are not always monotonic, probably because of a competition between different driving forces. For nanoparticles of high aspect ratio, steric effects seem to cause an isotropic-to-nematic phase transition as the surface coverage increases. It was observed that at a sufficiently high surface coverage the nanoparticles are most effective at reducing the interfacial tension when they lay with their longer axis parallel to the interface. The simulation results presented could be useful for the design of Pickering emulsions.

4.2. Introduction

Particle-stabilized emulsions, also known as Pickering emulsions, have been proposed for many applications, including crude oil separation,[72,74] biofuel upgrading,[8,121,122] drug delivery, and food preservation.[4,123,124] A better understanding of

the behavior of nanoparticles (NPs) at interfaces will help the further development of these, and other applications.[125]

Among other important factors, the NPs shape, the chemistry of functional groups on their surface, as well as the distribution of such groups on the NP surface determine the NPs interfacial behavior.[126-130] Several investigators considered, for example, Janus NPs (characterized by two types of surface properties, as the name implies).[8,121,122,131-138] It has been suggested that Pickering emulsions can be stabilized not only kinetically, but also thermodynamically using Janus NPs.[38] Recently, non-spherical NPs (rods, sheets, wedges, disk-like, needle-like, etc.) have been developed and sometimes used to stabilize oil-in-water emulsions.[55,57,58,126-128,139-141] Wedge-shaped NPs at interfaces can yield oriented structures,[139] amphiphilic nano-sheets can stabilize toluene-in-water emulsions,[55] and both ellipsoidal hematite NPs of high aspect ratio[57] and alkyl gallate micro-needles[141] are capable of stabilizing emulsions. It has been reported that the minimum amount of nanorods needed to stabilize an emulsion decreases as the particle aspect ratio increases.[58] The molecular mechanisms responsible for these observations, as well as whether or not NPs adsorbed at a liquid/liquid interface manage to reduce the interfacial tension,[51,142] remain the subject of scientific debate.

In addition to experiments, and often synergistically to them, numerous simulations and theoretical studies have been reported that document the effect of NP surface chemistry and shapes on the interfacial properties of NPs at liquid-liquid interfaces.[44,89,143-149] Atomistic molecular dynamics (MD) simulations are typically used for individual nanoparticles at interfaces.[89,143,146] Coarse grained models allow us to

investigate larger systems with longer time scales.[68] Our group used dissipative particle dynamics simulations (DPD), a coarse-grained method, to investigate the coalescence of droplets stabilized by NPs, the effect of NPs on the water-oil interfacial tension, the structure and dynamics of spherical Janus NPs adsorbed at water-oil interfaces.[44,147,148] We found that Janus NPs can in some cases stabilize emulsions better than homogeneous NPs, and that the interfacial tension can be reduced by NPs at high surface coverage.[147,148] The focus of the present contribution is on ellipsoidal NPs. This work was stimulated by recent contributions from Park et al.,[138,150,151] who investigated the equilibrium configuration of single nonspherical Janus NPs (prolate ellipsoids and dumbbells) at water-oil interfaces. These calculations quantified the orientation of individual NPs at the interface as a function of NP aspect ratio and surface properties. Because of numerical issues, the considered NPs were constrained to maintain their center of mass at the water-oil interface. Our tools allow us to relax this constraint, and to investigate systems composed by multiple NPs at the interface; we can therefore focus on the emergent behavior of ellipsoidal NPs. In addition to structural features, we quantify the interfacial tension reduction due to the presence of NPs at the interface, and more importantly to NP-NP interactions.

The remainder of the manuscript is organized as follows: we first present the methods and algorithms; we then discuss the results, and their relevance to experimental and theoretical observations available in the literature; finally we summarize our main findings.

4.3. Simulation Methodology

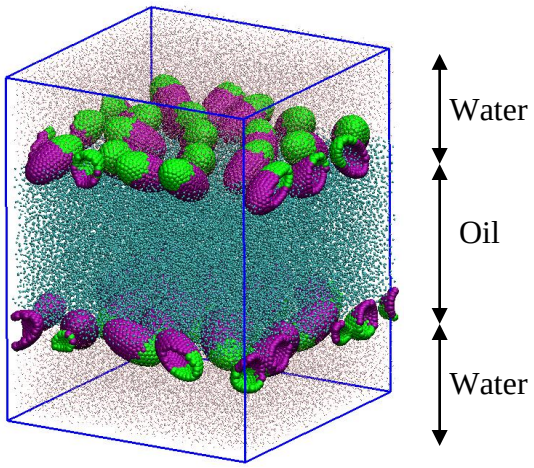

Figure 4.1. Schematic of one simulated system. Orthorhombic boxes are used, within which two planar water-oil interfaces are present. Pink and cyan beads represent water (w) and oil (o) beads, respectively. An equal number of ellipsoidal Janus nanoparticles (NPs) adsorb at both interfaces. Purple and green beads indicate nonpolar (ap) and polar (p) beads on the NPs, respectively. In this figure, each NP is a Janus prolate ellipsoid with aspect ratio 2.0.

Shown in Figure 4.1 is a typical simulation system, containing models for water and decane. Organic and aqueous phases demix, yielding two planar interfaces. The size of the orthorhombic simulation box is $L_X \times L_Y \times L_Z \sim 30 \times 30 \times 40 R_c^3$, where R_c is the DPD cutoff distance and L_i is the box length along the ith direction. Periodic boundary conditions are applied in all three directions. An equal number of NPs are randomly placed near each interface at the beginning of each simulation, with their polar (nonpolar) part in the water (oil) phase. No NP was found to desorb from the interfaces during our simulations.

The ellipsoidal NPs considered in this manuscript were hollow and contain polar (p) and nonpolar (ap) DPD beads on their surface. We considered oblate and prolate NPs, shown schematically in Figure 4.2. The shape of an ellipsoidal NP is defined by

the equation: $x^2/b^2 + y^2/b^2 + z^2/c^2 = 1$, where x, y, and z are Cartesian coordinates, and c and b are the semi-axis of the ellipsoid. When b=c spherical NPs are obtained. When c<b the ellipsoid is oblate; when b<c it is prolate. All NPs simulated had the same volume, $4/3\pi a_0^3$, where a_0 is the radius of the equivalent sphere. In the simulations below we imposed $a_0 = 2R_c \approx 1.5nm$.

The total number of beads on one NP surface changes with the aspect ratio. Specifically, 245 beads are used for NPs with c/b=4, 237 for c/b=2, 198 for c/b=1.5, 192 for c/b=1, 210 for c/b=0.5, and 252 for c/b=0.3. This allows us to maintain the surface bead density constant at 3.82 beads per R_c^2, which is sufficient to prevent other DPD beads (either decane or water) from penetrating the NPs (which would be unphysical). The NPs beads are either polar or nonpolar. The beads are arranged so that one face of one NP is entirely covered by beads of one type, hence Janus NPs, indicated as JPs. The two NP faces are separated by a boundary line, which we define as the Janus boundary line (JBL). The ratio between the two bead types (polar and nonpolar) ranged from 10% to 90%. In our notation, the number (e.g., 10) before JP (i.e., Janus particle) indicates the percentage of nonpolar beads. We focus on prolate NPs with JBL perpendicular to the NPs c axis, and on oblate NPs with JBL parallel to the NPs c axis (see schematic in Figure 4.2).

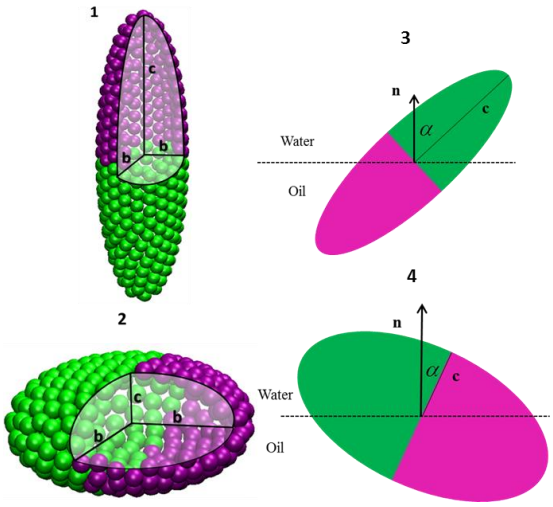

Figure 4.2. Schematic presentations of two 50JP NPs. Panel 1 is for a prolate NP with *c/b*=4; panel 2 is for an oblate NP with *c/b*=0.5. To ease visualization, one part of each NP is removed and the axes are shown. Purple and green beads are nonpolar and polar, respectively. In panels 3 and 4, we show how the orientation angle α is defined for prolate and oblate NPs, respective. In this picture, n is the normal vector of the oil/water interface.

Unless otherwise specified, the interaction parameters shown in Table 2.1 are used herein. By tuning the interaction parameters between polar (p) or nonpolar (ap) NP beads and the water (w) and decane (o) beads present in our system, it is possible to quantify the effect of surface chemistry on the structure and dynamics of NPs at water-oil interfaces.

Each simulation was run for 7×10^6 time steps, which approximately equals 1600 ns. The systems were equilibrated in the first 5×10^6 time steps. During the following 2×10^6 steps, data were collected every 500 time steps, and used for subsequent analysis. Due to limited computational resources, only some simulations were repeated with different initial configurations to check the reliability of the obtained data. The results were always found consistent, suggesting that proper equilibration was achieved in all

simulations presented below. Representative error bars are shown when such information is available.

4.4. Results

4.4.1. NPs Orientation

We define the orientation angle α as the angle between the vector *n* normal to the interface and the unit vector along the axis c of one NP (see schematic in Figure 4.2). Note that in the case of the prolate NPs, the direction of the axis c is perpendicular to the JBL, while for oblate NPs the direction of the axis c is parallel to the JBL. When the NP axis c is perpendicular to the interface, α =0°; when the axis c is parallel to the interface α =90°. We are interested in quantifying how the angle α changes when the NPs geometry and/or surface properties change. To investigate emergent properties (discussed below), we also quantify how such orientation changes as the NP density at the interface increases.

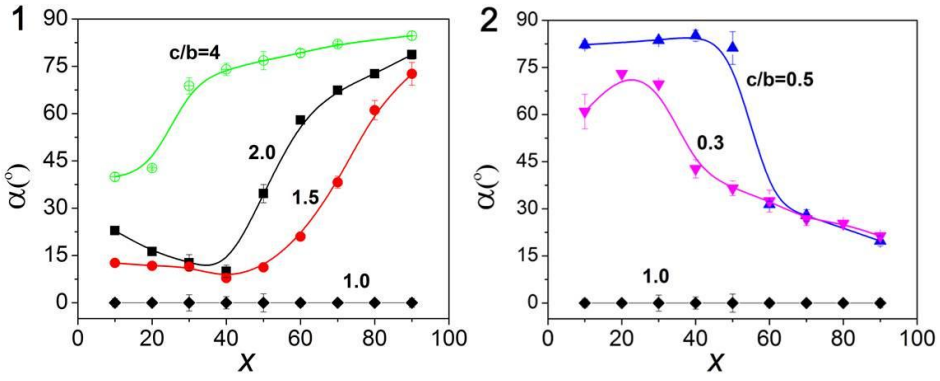

Figure 4.3. Orientation angle as a function of surface properties for various NPs. (1) Prolate NPs; (2) Oblate NPs. For these simulations the interface area per NP is maintained at $A_c \approx 84.34\ R_c^2$. The results for cases c/b=2 and c/b=0.5 are averaged from the results obtained from three independent simulations. Error bars represent one standard deviation from the average, and can be smaller than symbols. Lines are guides to the eye.

In Figure 4.3 we show how the average orientation angle α changes for ellipsoidal NPs of various aspect ratios as a function of their surface chemistry. The variable x represents the fraction of DPD beads on the NPs surface that are nonpolar. All results shown in Figure 4.3 are obtained at constant number of NPs at the interface, yielding a surface area per NP of $A_c \sim 84\,R_c^2$. At these conditions of low NP surface density, the influence of neighboring NPs on the orientation angle is negligible. The data are averaged over the behavior of all NPs in the systems simulated, over an extensive simulation time (details in the Methods section). Three independent simulations were conducted for NPs characterized by c/b=2 and c/b=0.5. Because the results were consistent for each system, only one, albeit long, simulation was conducted for the other cases. The error bars are estimated as one standard deviation from the average.

Before we discuss our results, we should refer to the recent theoretical and experimental results reported by Park and coworkers.[138,150,151,152] These authors suggested that in some cases it is possible that one non-spherical NP at a liquid/liquid interface adopts two well-defined orientations. One is representative of the equilibrium orientation, while the second represents a local minimum in the free-energy landscape. Stimulated by this report, we analyzed the distribution of orientation for the NPs considered in our simulations. The results, shown as Supplemental Material, indicate that each of the NPs considered in our work has one preferential orientation, although they oscillate around this preferential orientation. This suggests that the average angles reported in Figure 4.3 are representative of the global minima in the free-energy landscape. It is possible that the temperature of our systems provides sufficient fluctuations that the NPs escape the local minima discussed by Park and

coworkers.[138,150,151,152] We now return to the data shown in Figure 4.3. The results for ellipsoidal NPs are compared with those obtained for spherical NPs. As in spherical NPs b=c, the angle α is defined between the normal vector of the interface and the unit vector that points from the nonpolar to the polar face of the Janus NP. We maintain this formalism in both panels of Figure 4.3. As discussed in our prior report,[148] our results show that spherical Janus NPs maintain their JBL parallel to the water/oil interface, independently on the variable x. The ellipsoidal NPs show a much richer behavior.

In the case of prolate NPs (c>b, panel 1 in Figure 4.3) the angle α is small when the fraction of nonpolar beads on the NP surface is low (indicating that the axis c is perpendicular to the interface), but it increases to almost 90° as the fraction of nonpolar beads increases (indicating that the axis c becomes more and more parallel to the interface). The oblate NPs show a different behavior, with the angle α being large at low x (indicating that the axis c can be almost parallel to the interface), and decreasing as x increases (axis c more perpendicular to the interface). It should be pointed out that the trends just discussed are not always monotonic. For example, in the case of the prolate NPs with c/b=2, a clear minimum is observed for the angle α when x~40%, while in the case of oblate NPs with c/b=0.3 a clear maximum is observed for α when x~20%. The behavior of prolate Janus NPs at low surface coverage is qualitatively consistent with the global minima reported by Park et al.[150,151] For completeness, it should be repeated that in the case of the prolate NPs the axis c connects the nonpolar to the polar face of the Janus NPs, while for the oblate NPs the axis c is parallel to the JBL. As a consequence, when the results in Figure 4.3, panel 1 are considered, a small angle α

indicates that the JBL is parallel to the water-decane interface; when the results in Figure 4.3, panel 2 are considered, the JBL is parallel to the interface when $\alpha = 90°$.

As already discussed by Park et al.,[150,151] the equilibrium orientation of one NP at the water-oil interface is the result of two competing driving forces: (1) the minimization of the unfavorable water-oil interactions, which is obtained when the NP occupies as much interfacial area as possible, and (2) the minimization of NP-solvent interactions, which is obtained when the polar beads on the NP interact preferentially with water beads, and the nonpolar beads on the NP interact with oil beads. For spherical NPs, the interfacial area occupied by a NP does not depend on the orientation angle α, therefore the latter is only due to the minimization of NP-solvent interactions. For the prolate NPs considered here, the interfacial area occupied by one NP is maximized when $\alpha = 90°$, and the NP-solvent interactions are minimized when $\alpha = 0°$. Hence a competition emerges between the two driving forces, resulting in an orientation angle that changes with the fraction of the NP surface beads that are nonpolar (variable x in Figure 4.3). For example, the c/b = 2 NPs will orient their c axis parallel to the interface when x is large (to maximize the surface area occupied), while they will orient it perpendicularly to the interface when x is small (to minimize NP-solvent interactions). The appearance of a local minimum in orientation angle at around x=40 suggests that the driving force of minimizing NP-solvent interaction gains more influence as x increases from 10 to 40; while the tendency to maximize occupied interfacial area excels as x increases further to 90. For the oblate NPs considered here, the interfacial area occupied by one NP is maximized when $\alpha = 0°$, and the NP-solvent interactions are

minimized when α = 90°. In addition to the effects just discussed, it is possible to change the equilibrium orientation angle α for a given NP by manipulating the interaction parameters used in the simulations. One example of such calculation is provided as Supplemental Material. Experimentally, changing the chemical groups tethered to the NP surface, or changing one or both solvents could attain such manipulation. It should be pointed out that controlling the orientation of one Janus NP at water-oil interfaces could be extremely important when catalytic systems are designed to operate at such interfaces.[8] In these cases, for example, it is desired to have different catalysts in contact with organic or aqueous phases.

4.4.2. Emergent Behavior

In Figure 4.4 we show the variations of orientation angles of the NPs considered in Figure 4.3 as the NP surface density changes. Surface density is indicated by surface area per NP, A_c. Lower A_c corresponds to higher NP density at the interface. Different NPs are considered in the various panels of Figure 4.4. The NP aspect ratio increases from panel a to f; correspondingly the NP geometry changes from oblate to sphere and then to prolate. The data are averaged over all NPs in the simulated system. To ease visualization, for each NP aspect ratio we only consider two surface properties, namely the nonpolar fractions x=30 and x=70 (less and more nonpolar, respectively). The results obtained for NPs with different surface properties (e.g., x=50) vary within the limits described in Figure 4.4, following the trends highlighted in Figure 4.3 when $A_c \sim 84\,R_c^2$. It is worth repeating that for oblate NPs (panels a and b) the axis c is parallel

to the JBL, while for spherical and prolate NPs (panels c, d, e, and f) the axis c is perpendicular to the JBL (see Figure 4.2).

The results for the spherical Janus NPs are shown in panel c of Figure 4.4. These results show that, independently on the surface properties and on the NP density at the interface, the average orientation of the NPs is such that the axis c is perpendicular to the water/oil interface.

For all other NPs, the results show that when the NPs surface is predominantly polar (i.e., x=30) the average orientation of the NPs with respect to the liquid-liquid interface does not change as the NP density increases. The only exception is observed when the NP aspect ratio is 4 (panel f). In this case the average orientation changes by at most 10° when A_c decreases from ~ 84 to $25\,R_c^2$.

When x=70 the average NP orientation changes for most of the NPs considered, except when the NPs are spherical (panel c). However, our results show that the change in average orientation never exceeds ~ 20° for any of the NPs considered here. Because the changes in NP orientation are always observed at rather high NP density at the water-oil interface, we conclude that these emergent phenomena are due to NP-NP interactions, which are for the most part due to steric effects in our simulations.

The observation that the orientation angle of prolate NPs decreases with increasing surface coverage agrees with the simulation results of Xu et al.[129] for Janus nanorods adsorbed at the interface of binary polymer mixtures. This result was explained by increased nanorod-nanorod interactions with the interfacial density. These authors found that the orientation angle of nanorods increases with the aspect ratio, which also agrees with our findings on prolate NPs.

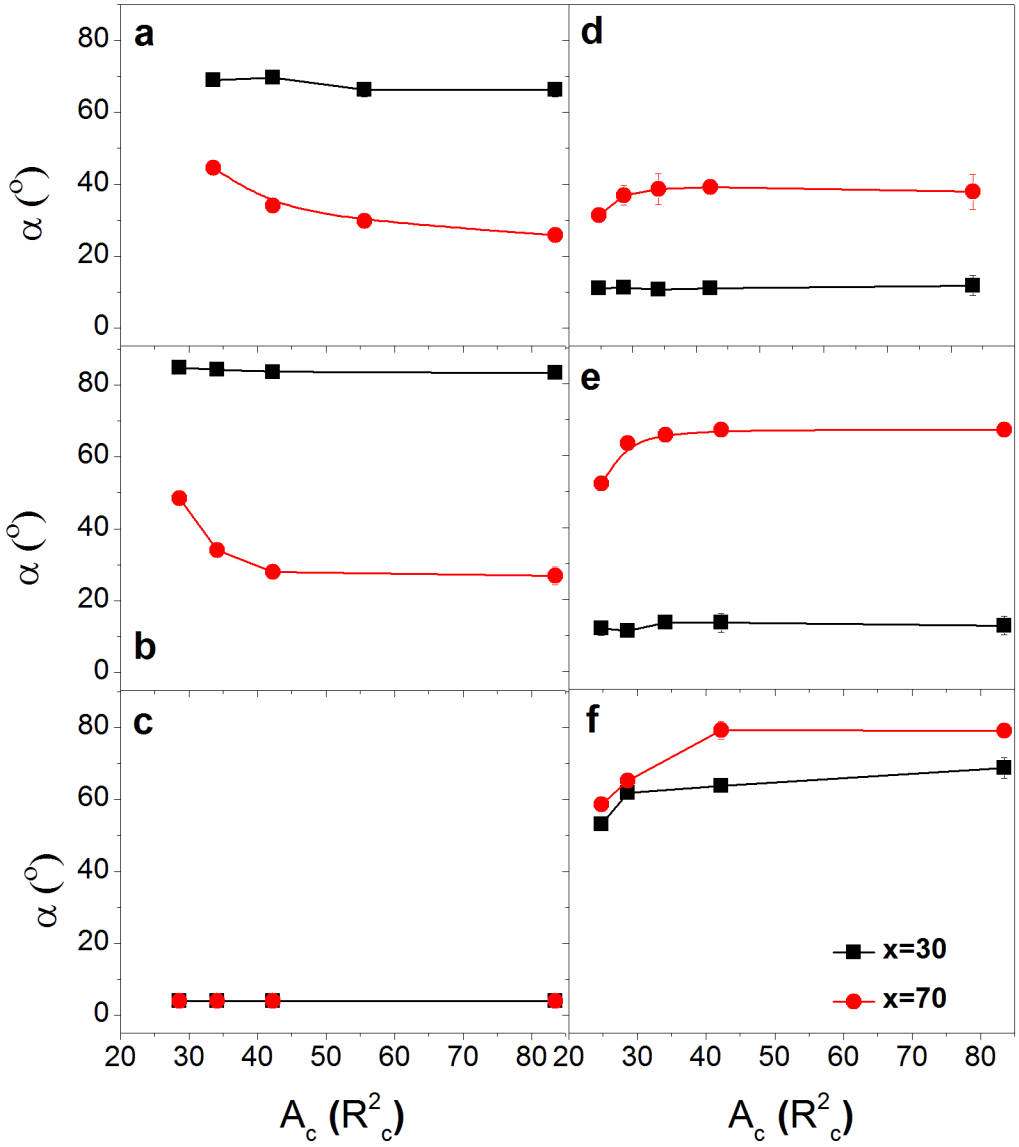

Figure 4.4. Averaged orientation angle for ellipsoidal NPs at the water-decane interface as a function of surface area per NP, A_c. For each Janus NP the results are shown for two levels of surface 'nonpolar coverage' x, 30 and 70. The error bars represent one standard deviation from the average. In most cases the error is smaller than the symbols. Lines are guides to the eye. Different panels are for different NPs: (a) *c/b*=0.3; (b) *c/b*=0.5; (c) c/b=1; (d) c/b=1.5; (e) c/b=2.0; (f) c/b=4.0. In panel c the two data sets overlap.

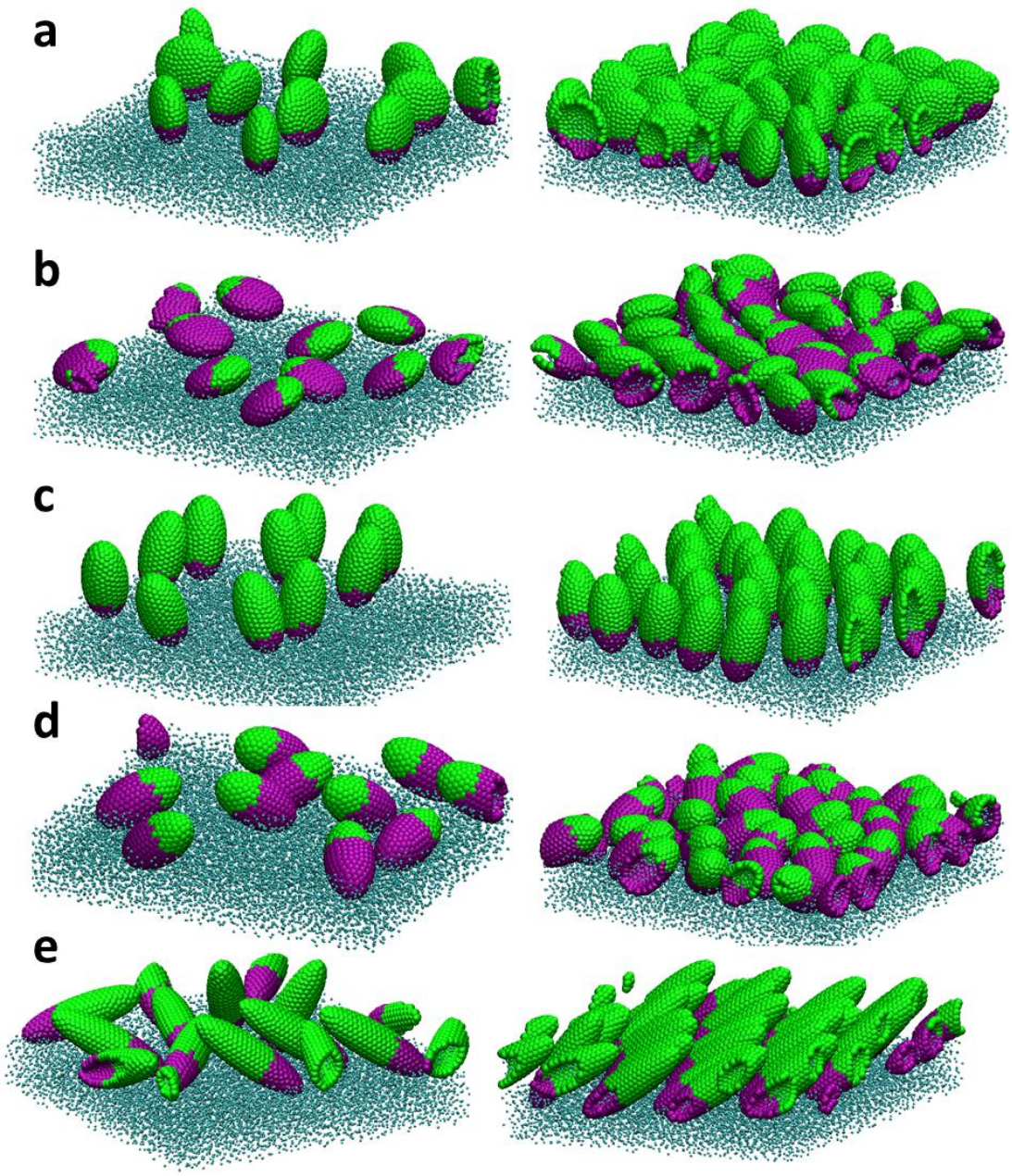

Figure 4.5. Representative simulation snapshots for some ellipsoidal Janus NPs adsorbed at the water-oil interface. The NP beads are colored consistently with Figure 4.2. The cyan beads represent oil beads. Water beads are not shown for clarity. Left and right panels are obtained at surface area per NP Ac~84 R_c^2 and ~28 R_c^2, respectively. From top to bottom, different panels are for different NPs: (a) c/b=0.5 with x=30; (b) c/b=0.5 with x=70; (c) c/b=2 with x=30; (d) c/b=2 with x=70; (e) c/b=4 with x=30.

In Figure 4.5 we report representative simulation snapshots for several systems considered in Figure 4.4. Simulation snapshots for other NPs are not reported because their behavior is very similar to what discussed in Figure 4.5. For example, NPs with aspect ratios c/b=0.3, c/b=1.5, and c/b=4 (all characterized by x=70), behave similarly to NPs with aspect ratios c/b=0.5, c/b=2, and c/b=4 (all characterized by x=30), respectively. Left and right panels in Figure 4.5 are for low and high NP density at the interface, respectively. Visual inspection of left and right panels for the same NPs confirms that the NP orientation does not change substantially as the NP density increases. The NPs in panel (e) only slightly change their average orientation with respect to the interface as the NP density increases. However, the snapshots suggest that in this case the NPs are rather disordered at low surface density, while they show pronounced order at high density.

4.4.3. Isotropic-to-Nematic Transition

To characterize the structure of ellipsoidal NPs at the interface, we calculated two dimensional radial distribution functions (RDFs), *g(r)*. For these calculations, r is the distance between the beads located at the center of two NPs. Representative results are shown in Figure 4.6. For brevity, we only show data for NPs with aspect ratio c/b=2 characterized by x=30 and x=70 (Figures 4.6a and 4.6b, respectively). The RDFs are shown at various surface coverages. For the NPs shown in Figure 4.6a, the orientation angle is small (~15°) (the c axis of the NPs remains almost perpendicular to the interface) at all surface coverages considered. As discussed for spherical NPs,[148] the RDFs are characterized by numerous peaks. Those found at r ~ 4-8 R_C represent the first shell of neighboring NPs, separated by different numbers of solvent beads; those found

at r ~ 9-12 R_C correspond to the second shell. As A_c decreases, the intensity of the first and second peaks increases and that of the third peak decreases, suggesting that as the NP surface density increases, the NPs form a dense liquid structure, similar to that observed for spherical NPs.[148]

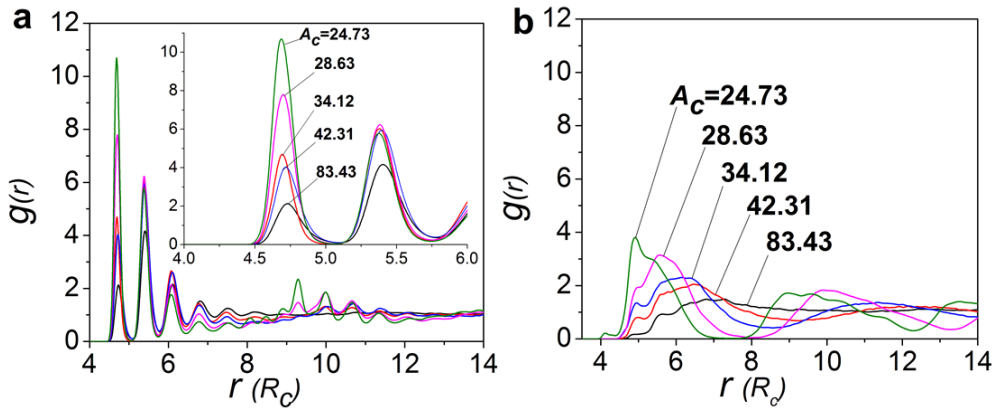

Figure 4.6. Two-dimensional radial distribution functions *g(r)* obtained for various NPs with aspect ratio *c/b*=2 at decreasing A_c. Panels (a) and (b) are for x=30 and 70, respectively.

In the case of the NPs with x=70 (Figure 4.6b), the angle α is ~60-70° when few NPs are at the interface, suggesting that these NPs preferentially maintain their c axis almost parallel to the interface (see Figure 4.3). As the surface density increases, α decreases because of NP-NP interactions, and the NPs project their c axis in a direction that is more perpendicular to the interface (see Figures 4.4 and 4.5). The RDF data shown in Figure 4.6b are much less structured than those shown in Figure 4.6a. These results suggest that when A_C is large (i.e, A_c=83.43 R_c^2) the NPs assume a disordered liquid-like structure. When A_c<34.12 R_c^2, two peaks become distinct, and eventually become separated by a region at which the RDF equals 0. Although the peaks observed

at high surface coverage (low A_C) are much less pronounced and much wider than those shown in Figure 4.6a, they seem representative of ordered structures.

To further characterize the structure of NPs at the interface, we employed the orientational radial correlation C_p,[153] which allows us to quantify the relative orientation of two NPs as a function of the distance between them. C_p is obtained by

$$C_p = \frac{\left\langle \sum_{i \neq j} \frac{1}{2}(3(u_i \cdot u_j)^2 - 1)\delta(r_{ij} - r) \right\rangle}{\left\langle \sum_{i \neq j} \delta(r_{ij} - r) \right\rangle} \tag{4.1}$$

In Eq. (4.1), u_i is a unit vector along the c axis of a NP i. δ is the Dirac delta function, which tags two NPs i and j separated by distance $r_{ij} = r$. The delta function is calculated by selecting intervals of width $\Delta = 0.075R_C$. The angular brackets represent ensemble averages. When two NPs are parallel to each other, $C_p = 1$; when they are perpendicular to each other, $C_p = -0.5$; when they show no preferential orientation, $C_p = 0$. Note that a nematic phase is characterized by a C_p that remains ~1 at sufficiently large r, while isotropic phases are characterized by $C_p \sim 0$.

In Figure 4.7, we plot the results for C_p calculated for selected NPs (c/b=0.5, c/b=2.0, and c/b=4.0). The results for NPs with c/b=0.3 are similar to those with c/b=0.5, thus not shown. For each NP type, data are shown for x=30 and x=70. Based on our observations, both oblate and prolate NPs with low aspect ratios (c/b = 0.5 and 2.0, respectively) present nematic phases independently on surface coverage when x is small

(left panels), while they yield isotropic phases when x is large (right panels). For these NPs the nematic phase is favored even at low surface coverage because these prolate (oblate) NPs always orient their c axis nearly parallel (perpendicular) to the vector normal to the interface (Figure 4.5). When x is large, these NPs are oriented randomly with respect to each other, which is consistent with isotropic phases. For the NPs just discussed, our results suggest the presence of nematic phases only when the NPs JBL is parallel to the interface.

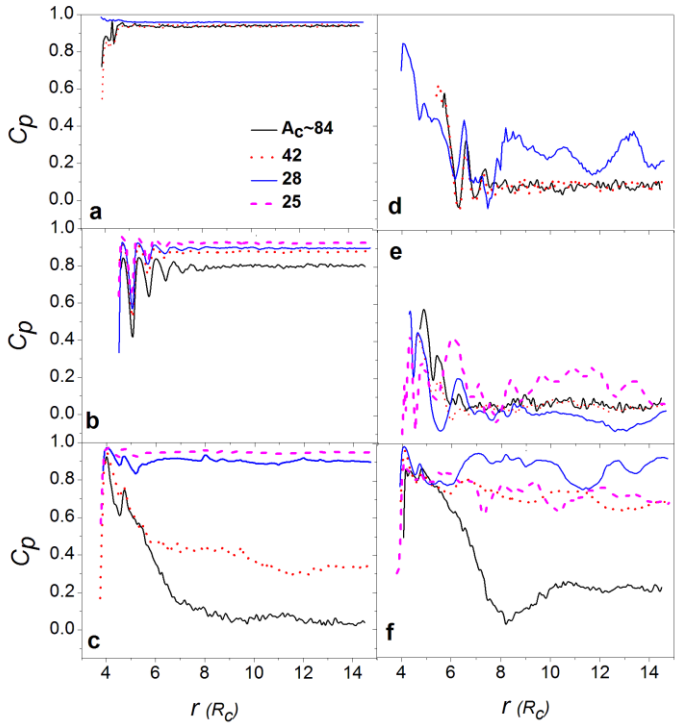

Figure 4.7. Orientational correlation function C_p as a function of NP distance r. Left and right panels are obtained for x=30 and x=70, respectively. From top to bottom, different panels are for different NPs: (a) c/b=0.5; (b) c/b=2; (c) c/b=4; (d) c/b=0.5; (e) c/b=2; (f) c/b=4. In each panel the results are presented for different values of interface area per NP, A_C.

The prolate NPs with aspect ratio c/b=4.0 behave differently. The results in panels c and f suggest an isotropic to nematic phase transition as density increases. This

appears counter-intuitive, as the averaged orientation angle is higher than 45° for these NPs when x is either 30 or 70 (Figure 4.4). Visual analysis of the simulation snapshots in Figure 4.5 confirms that at high surface density these NPs are all parallel to each other, at an angle slanted with respect to the liquid-liquid interface. Because the isotropic-to-nematic phase transition occurs as the surface density of the NPs increases, we believe that entropic effects are responsible for it. In fact the excluded volume will decrease when all NPs are oriented in the same direction.

4.4.4. Interfacial Tension

It is still debated whether NPs can reduce the water-oil interfacial tension. Some suggest that repulsive NP-NP interactions can lead to interfacial tension reductions.[142,147] Our previous studies on spherical NPs with different surface chemistries (Janus or homogeneous) are consistent with this possibility.[148] Because ellipsoidal NPs can present different oriented configurations at the water-oil interface, it is of interest to investigate how interfacial tension changes upon NP loading. We report in Figure 4.8 the interfacial tension reduction $\gamma_0 - \gamma$ (i.e., the difference between the water-decane interfacial tension when no NP is present, $\gamma_0 \approx 7.1 k_B T / R_c^2$, and that when NPs are present, γ) as a function of the surface area per NP. Standard methods are used to calculate the interfacial tension.[154] The results in Figure 4.8 for spherical NPs (panel c) agree well with the data we published previously for Janus NPs with x=50.[148] The data in Figure 4.8 suggest that prolate and oblate NPs can reduce interfacial tension more efficiently than spherical ones, provided that the NP surface density is high. For a given NP shape, the interfacial tension reduction becomes more significant as x (the

percent of nonpolar beads on the NP surface) increases. Analysis of simulation results suggest that prolate and oblate NPs are more effective than spherical NPs in reducing the interfacial tension because of the larger excluded volume, which increases when the NPs orient their longer axis parallel to the interface.

Our results are consistent with recent experimental data, according to which emulsions can be stabilized by prolate hematite NPs with sufficiently high aspect ratio (i.e., c/b>2),[57] and the interfacial tension reduction increases with nanorod length.[127] The fact that the interfacial tension is predicted to decrease significantly in the presence of prolate NPs with high orientation angle may also explain the observation that a smaller amount of nanorods is needed to stabilize emulsions when higher aspect ratio species are used.[58]

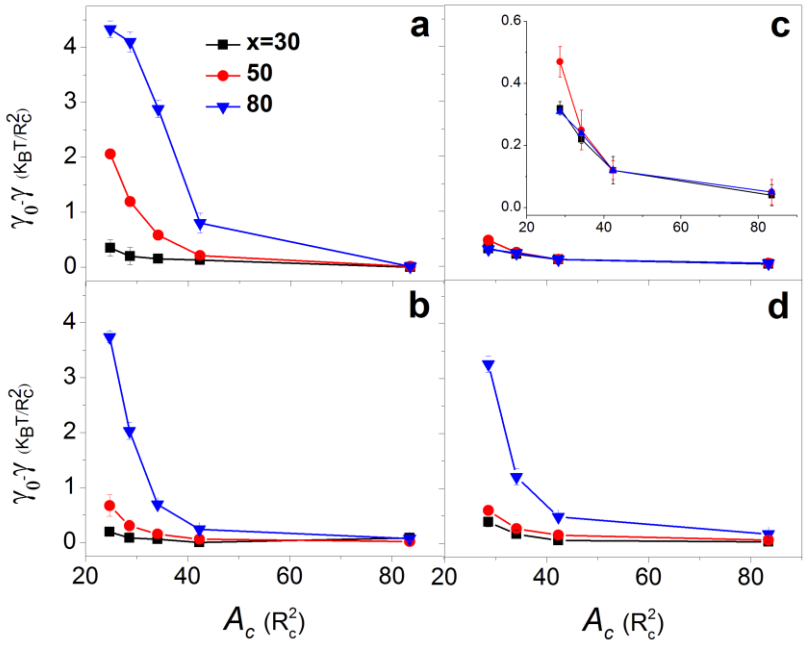

Figure 4.8. Interfacial tension reduction as a function of interfacial area per NP (A_c) for selected NPs. The error bars represent one standard deviation from the average. Lines are guides to the eye. Different panels are for different NPs: (a) *c/b*= 4; (b) *c/b*=2; (c) *c/b* =1; (d) *c/b*=0.5. In each panel, NPs with different surface properties are compared.

4.5. Conclusions

The behavior of ellipsoidal Janus nanoparticles with different shapes, surface chemistry and density at water-oil interface was investigated using dissipative particle dynamics simulations. The averaged orientation of a NP with respect to the liquid-liquid interface was found to depend on many factors. When the Janus NPs are spherical, the average orientation, within the conditions considered here, does not change when either the NP surface properties or the NP surface density are changed. When the NPs are ellipsoidal, both factors affect the averaged nanoparticle orientation. Our results suggest that the average orientation angle might play a critical role in determining the properties of Pickering emulsions, as it is found to strongly affect the liquid-liquid interfacial tension. Only in some cases we found that increasing the NP surface density affects the average NP orientation. For prolate NPs with aspect ratio of 4 (the highest considered here) our results provide evidence for an isotropic-to-nematic phase transition that seems to be triggered by entropic effects. This transition seems to occur without significant changes in the average NP orientation with respect to the liquid-liquid interface. These findings may help enhance the efficiency of utilizing nanoparticles in Pickering emulsions as well as design novel nanomaterials for liquid crystal thermometers and optical electronic devices.

Chapter 5. Ellipsoidal Janus Nanoparticles Assembled at Spherical Oil/Water Interfaces

5.1. Abstract

The equilibrium behavior of ellipsoidal Janus nanoparticles adsorbed at spherical oil/water interfaces was investigated using dissipative particle dynamics simulations. Several phenomena were documented that were not observed on similar simulations for planar oil/water interfaces. The nanoparticles were found to yield isotropic, radial nematic phases, and axial nematic domains, depending on the nanoparticle characteristics (aspect ratio and surface chemistry), particle density at the interface, and droplet properties (curvature of the interface, and, surprisingly, liquid type). When adsorbed on water droplets, the nanoparticles with high aspect ratio and few nonpolar beads on their surface can show two preferred orientation angles. Only one equilibrium orientation was found for such nanoparticles adsorbed on oil droplets. These observations might help explain a discrepancy previously reported between experimental and simulation results concerning the preferential orientation of particles at liquid-liquid interfaces. Different driving forces are responsible for the phenomena just summarized, including nanoparticle-nanoparticle and nanoparticle-solvent interactions, nanoparticle density at the interface, and droplet curvature via the Laplace pressure. The simulation results we present could be useful for engineering Pickering emulsions towards practical applications, and perhaps also for guiding new technologies for material synthesis.

5.2. Introduction

Particles and nanoparticles (NPs) can be used to stabilize the so called Pickering emulsions.[155] It has been proposed to use Pickering emulsions in various applications, including biofuel upgrading,[8] cosmetics and oil processing.[156,157] Because NPs are used as emulsifiers, their characteristics (e.g., surface chemistry and shape) have critical effects on the emulsions properties (e.g., interfacial tension, droplet size, and emulsion stability). For example, spherical Janus NPs (in which the surface functional groups are segregated in two distinct portions of the NP surface) are more effective at reducing interfacial tension than NPs of similar size and composition in which the functional groups are randomly distributed on the surface (homogeneous NPs).[39,52,158] Non-spherical NPs (e.g., rods, sheets, wedges, disk-like, needle-like, etc.) can be more efficient in stabilizing emulsions than spherical NPs,[55,57,159] and can also yield oriented structures, which could lead to additional interesting phenomena and possible applications.[42,58,150,160]

In our previous work, we focused on NPs with different surface chemistry and shape adsorbed on flat oil/water interfaces.[39,158,160] We assessed structural and dynamical properties of spherical NPs with different surface chemistries, and also their ability to reduce the interfacial tension.[39,158] We then simulated ellipsoidal NPs and found that by changing NPs aspect ratio, surface chemistry, and surface density it is possible to obtain either isotropic or axial nematic phases.[160]

In this manuscript we seek to quantify the structure and possible emergent behavior of ellipsoidal Janus NPs when they adsorb on oil (water) droplets immersed in water (oil). By changing the size of the droplets, we quantify how the curvature of the

interface affects the NPs behavior, which is expected to have practical and fundamental interest.[44,161-167] It should be noted that, because of computing power limitations, the droplets considered are never larger than ~10 times the maximum dimension of the NPs considered.

In the remainder of the manuscript, we first present the methods and algorithms; we then report our results, discussing their relevance to experimental and theoretical observations available in the literature; finally, we summarize our main findings.

5.3. Methods and Algorithms

The nanoparticles considered (NPs) are prolate Janus NPs with different aspect ratios and surface chemistries. The equation defining the NP shape is $x^2/b^2 + y^2/b^2 + z^2/c^2 = 1$, where x, y and z are Cartesian coordinates, and *b* and *c* are the semi-axes of the ellipsoidal NPs. The surface chemistry is manipulated by placing polar and nonpolar beads on the NP surface. We report the nonpolar fraction N of the NP surface beads. For example, N=30 indicates that 30% of the beads on the NP surface are nonpolar.

For the simulations discussed herein we consider one droplet, either oil or water, surrounded by the continuous phase (water or oil). The size of the droplet was varied. At the beginning of each simulation, a number of NPs are randomly placed at the droplet interface with their polar (nonpolar) part in the water (oil) phase. Shown in **Figure 5.1** is an example of one simulated system consisting of an oil droplet in water. For each simulation an orthorhombic simulation box with dimensions

$L_X \times L_Y \times L_Z \sim 120 \times 120 \times 120 R_c^3$ was used, where R_c is the DPD cutoff distance, and L_i is the box length along the ith direction. Periodic boundary conditions are used in all three dimensions. The largest droplet simulated was of diameter ~85R_c, which implies that ~ 35R_c was the minimum distance between a droplet and its periodic replica. Given the sort range typical of DPD interactions, we considered the simulation boxes large enough to minimize box-size effects. Each simulation was first equilibrated during 10^6 time steps. During the subsequent 10^6 time steps, data were recorded every 1000 time steps and used for analysis. Each simulation was repeated 3 times with different initial configurations to check the reliability of the results. The consistency between the simulation results suggests that proper equilibration was achieved.

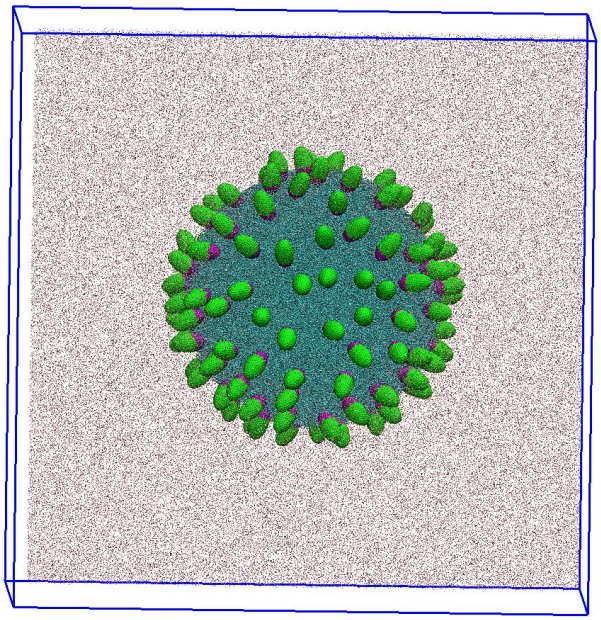

Figure 5.1. Schematic of one typical simulation box. The oil droplet (cyan) is covered by NPs and immersed in water (pink). Green and purple beads are polar and nonpolar, respectively, on the NPs. The prolate NPs have aspect ratio 2.0, and 30% of the beads on their surface are nonpolar.

To characterize the NPs structure on a droplet we focus on the orientation of their longest axes (the c axes) either with respect to each other or with respect to the radial directions from the center of the droplet. An isotropic phase is observed when the c axes of the various NPs are randomly oriented.[168] When the c axes are parallel to each other, an axial nematic phase is observed.[160] A radial nematic phase is formed when the c axes are parallel to the radial direction of the droplet.[169] Order parameters can be used to distinguish the various phases. We discussed the axial nematic order parameter when we considered flat interfaces.[160] For this work the radial nematic order parameter, S_R, is more relevant, as we used it to discriminate isotropic and radial nematic phases. The latter order parameter is obtained as:[169]

$$S_R = \left\langle \sum_i \frac{1}{2}(3(u_i \bullet R_i)^2 - 1) \right\rangle \tag{5.1}$$

In Eq. (5.1), u_i is the unit vector along the NP c axis and R_i is the unit vector representing the radial direction from the center of mass of the droplet. Angular brackets represent ensemble averages. $S_R \sim 1$ when a radial nematic phase is observed; $S_R \sim 0$ when an isotropic phase with respect to the radial direction is observed. The calculation of the radial nematic order parameter facilitates the definition of the orientation angle α, which is the angle between u_i and R_i. In **Figure 5.2** we report a schematic. When $\alpha = 0°\,(90°)$ the correspondent NP is parallel (perpendicular) to the droplet radial direction, and therefore perpendicular (parallel) to the local liquid-liquid interface. Note that the angle α is defined so that it is never larger than 90°.

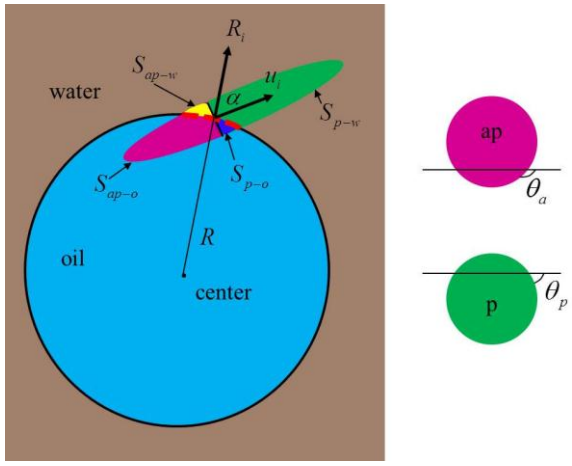

Figure 5.2. Schematic representing an ellipsoidal Janus NP adsorbed at the oil-water interface. In this picture, ap (pink), p (green), o (cyan), and w (purple) represent nonpolar, polar, oil, and water, respectively. u_i and R_i are the unit vectors along the NP c axis and along the radial direction from the center of the droplet, respectively. S_{p-w}, S_{p-o}, S_{ap-w}, and S_{ap-o} are polar NP surface in water, polar surface in oil, nonpolar surface in water, and nonpolar surface in oil, respectively. The interfacial area occupied by the NP, S_I, is highlighted in red. θ_a and θ_p are the contact angles of completely nonpolar and polar spherical NPs, respectively.

5.4. Results

5.4.1. Oil Droplets Immersed in Water

In **Table 5.1**, we report S_R and the average orientation angle obtained for NPs with aspect ratio c/b=2 adsorbed on an oil droplet with diameter d~50R_c immersed in water. The NPs have two surface chemistries: N=70 and N=30 (70% and 30% nonpolar beads, respectively). The radial order parameter was calculated at various NP surface densities, expressed in terms of interface area per NP, A_c. Low A_c corresponds to high surface density. Our results show that S_R does not change significantly when A_c varies for either NP type. S_R~0.8 for NPs with N=30, and S_R<0.4 for NPs with N=70. These data indicate that NPs with N=30 yield a radial nematic phase, while the N=70 NPs

yield an isotropic phase. The average orientation angle results show that the N=30 NPs yield an orientation angle α lower than ~20° with respect to the droplet radial direction. The density of the NPs at the oil-water interface does not affect significantly this orientation. Instead, the average orientation angle for the NPs with N=70 does change with NPs surface density, form ~ 65° at low surface density to ~45° at the highest surface density considered. At all conditions, the N=70 NPs, as already mentioned, yield a radially isotropic phase. The behavior of NPs with aspect ratio 2 on the droplet, just summarized, is similar to that of the same NPs adsorbed at the flat oil/water interface as shown in our previous studies.[160] The only difference is that instead of radial nematic order vs. isotropic, axial nematic order vs. isotropic was observed at the flat interfaces.

Table 5.1. Radial order parameter S_R, and average orientation angle of NPs adsorbed on an oil droplet of diameter $50R_c$ immersed in water. The errors are obtained as one standard deviation from the average of three simulations. NPs have aspect ratio 2 and surface chemistry N=30 or 70.

Area per NP (A_c)	**N=30**		**N=70**	
	S_R	$\alpha(°)$	S_R	$\alpha(°)$
90.5	0.80 ± 0.05	19.9 ± 2.8	0.16 ± 0.06	65.6 ± 4.5
39.8	0.82 ± 0.03	19.5 ± 1.5	0.19 ± 0.04	63.5 ± 3.8
26.5	0.82 ± 0.03	16.8 ± 1.1	0.15 ± 0.02	61.7 ± 2.8
19.4	0.89 ± 0.01	10.4 ± 0.6	0.40 ± 0.02	45.6 ± 1.9

In **Figure 5.3** we report representative simulation snapshots for the systems discussed in **Table 5.1** at two surface densities. These images confirm that NPs with N=30 (panels a and b) yield a radial nematic phase and those with N=70 (panels c and d)

yield an isotropic phase, independent with NP surface density. We expect that NPs of the same aspect ratio and with small N will behave similarly to those with N=30, while those with large N will behave similarly to those with N=70 NPs. Some examples are shown in **Figure 5S.1** in Supplemental Information (SI) for N=10 NPs and N=90 NPs. It is worth mentioning that the NPs orientation angle at an interface, as well as their structure, depends on the interactions between the NP and the solvent beads. In **Figure 5S.2** in Appendix, for example, we show that it is possible to change NP structures from isotropic to radial nematic by reducing the repulsive interaction between nonpolar and oil beads. Experimentally, changes in effective interactions can be achieved by either grafting different the functional groups to the NP surface, or by changing the solvents.

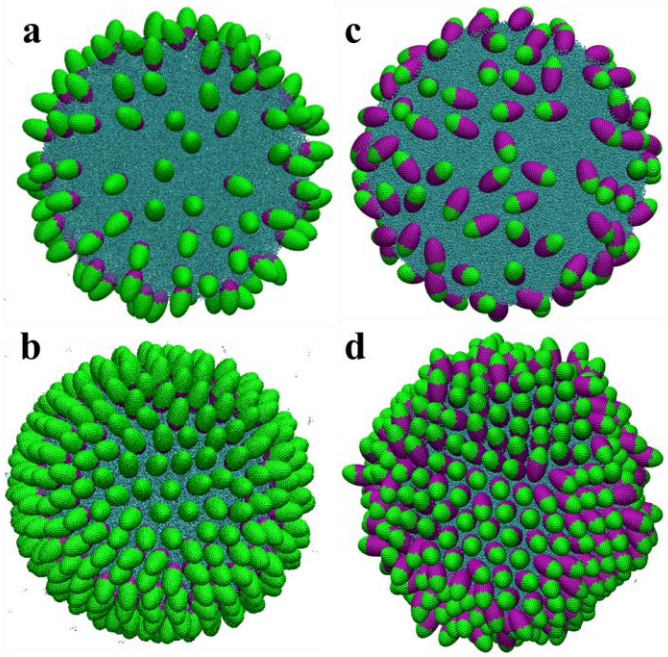

Figure 5.3. Representative simulation snapshots for ellipsoidal Janus NPs adsorbed on one oil droplet immersed in water. The color code is that of Figure 5.1. Water beads are not shown for clarity. The droplet diameter is $50R_c$. The NPs have aspect ratio 2. Left and right panels are for NPs with N=30 and N=70, respectively. Top and bottom panels are for $A_c = 90.5R_c^2$ and $A_c = 19.4R_c^2$, respectively.

To further quantify the NP packing structure on the curved interface, we extracted a portion of the droplet surfaces from panels (b) and (d) in **Figure 5.3**. We then magnified these images in panels (a) and (c) in **Figure 5.4**, respectively. To improve visualization we flattened these curved surfaces and showed the locations of the NPs center of mass in panels (b) and (d), respectively. The algorithm implemented for flattening the images is described by Meng et al.[29] To quantify the results we considered the nearest neighbors to one tagged NP. Two NPs are considered nearest neighbors if the distance between their two centers is less than $5.5R_c$, the shortest distance between two NPs parallel to each other. In Figure 4.4, the black filled circles represent NPs with six nearest neighbors; the stars indicate NPs that do not have six nearest neighbors. The results in **Figure 5.4** suggest that both N=30 and N=70 NPs yield hexagonal structures on the oil droplet, although defects are visible. The defects are due, in part, to elastic stress due to the curvature of the interface. This result agrees with observations by Bausch et al.,[170] who investigated spherical particles adsorbed on oil droplets, and found that the defects are necessary to alleviate the elastic stress induced by the adsorption of repulsive particles at the interface. The defects can also be a consequence of the ellipsoidal shape of the NPs considered in our simulations, which might prevent hexagonal packing when the particles are not perpendicular to the interface.

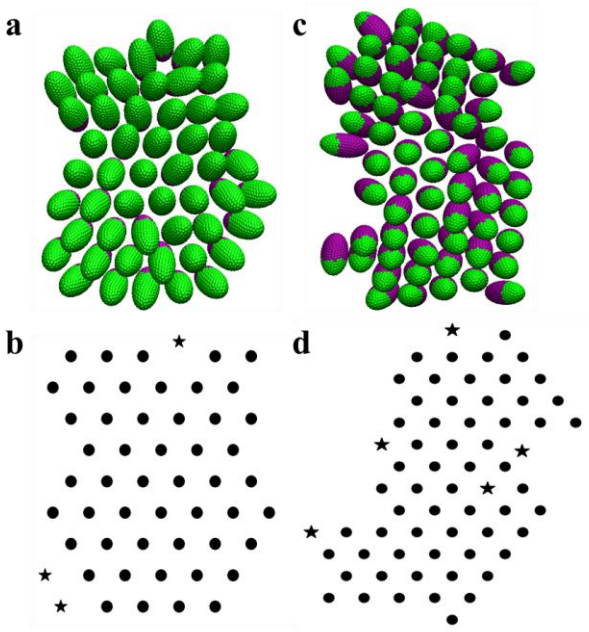

Figure 5.4. One portion of the droplets surface shown in panels (b) and (d) of Figure 5.3 is extracted and magnified in panels (a) and (c), respectively. The interfacial areas are flattened and shown in panels (b) and (d), respectively. In these latter panels the filled circles are for the centers of NPs that have six nearest neighbors, the stars for NPs with more or less than six nearest neighbors, which are indicative of 'defects'.

When NPs of aspect ratio 4 adsorb at the flat oil/water interface, their structure changes from isotropic to axial nematic upon increasing their surface density.[160] We investigate here whether the curved interface affects the behavior of these NPs. In **Figure 5.5** we report representative simulation snapshots obtained for such NPs adsorbed on an oil droplet of diameter $50R_c$. The left (right) panels are for NPs with N=30 (N=70). An isotropic phase is observed when NP density is low ($A_c \sim 90 R_c^2$) for both N=30 NPs (panel a) and N=70 NPs (panel d), as confirmed by low values of S_R ($S_R \sim 0.01$ for both panels). At medium NP density ($A_c \sim 35 R_c^2$, panels b and e) we observe that some NPs are aligned in the same direction. These NPs are found grouped

into ‘axial nematic’ domains. As domains were not observed on the flat oil-water interfaces, their appearance here must be due to the curved interface. Visualization of simulation snapshots showed that the droplet interface in these domains was flat. Note that the orientation angle of NPs on one domain can be different compared to that on other domains. The size and shape of one domain can be also different with those of other domains. When the NP density is sufficiently high (A_c~24 R_c^2), a radial nematic phase is observed for N=30 NPs (panel c, for which $S_R \sim 0.88$), while axial nematic domains are observed for N=70 NPs (panel f).

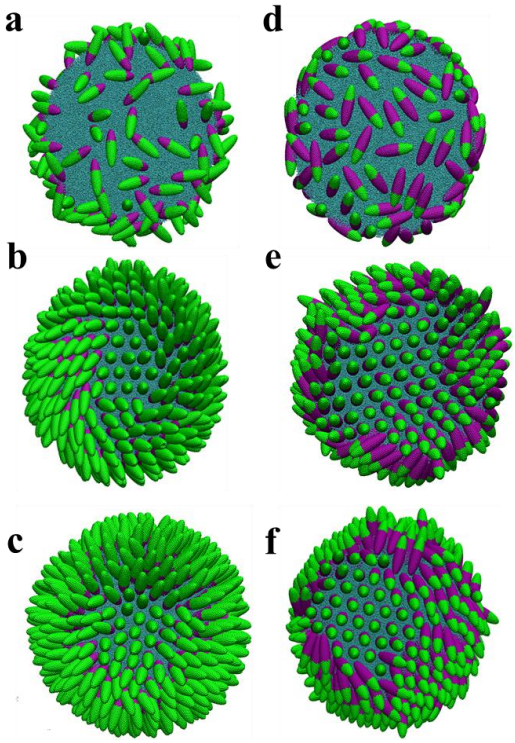

Figure 5.5. Representative simulation snapshots for ellipsoidal Janus NPs adsorbed on one oil droplet. Water beads are not shown for clarity. The droplet diameter is $50R_c$. The NPs have aspect ratio 4. Left and right panels are for NPs with N=30 and N=70, respectively. From top to bottom, the NP surface density is increased: in panels (a) and (d) A_c~90 R_c^2; (b) and (e) A_c~35 R_c^2; (c) and (f) A_c~24 R_c^2.

In **Figure 5.6** we report simulations snapshots to systematically present the change of NP structures as the oil droplet size varies. All snapshots are shown at high NP surface density ($A_c \sim 24 R_c^2$). NPs with aspect ratio 4 are used. The left and right panels are for NPs with N=30 and N=70, respectively. The snapshots for droplet size $d=50R_c$ are shown in **Figure 5.5**, and are not reproduced here. The top panels are for the flat interfaces. The inspection of these images suggests that, as droplet size reduces, N=30 NPs structures change from axial nematic on the entire interface (panel a) to axial nematic domains (panel b) to radial nematic phase (panel c). The observations for N=70 NPs are similar to those of N=30 NPs except that the transformation to radial nematic phase is not observed.

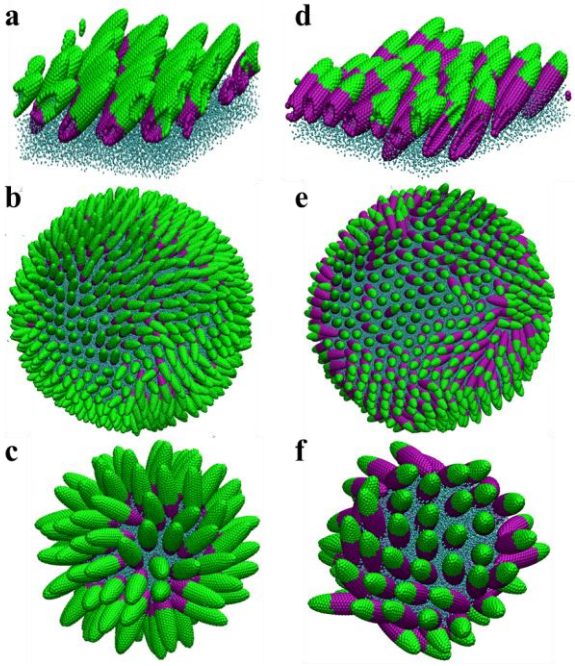

Figure 5.6. Representative simulation snapshots for ellipsoidal Janus NPs adsorbed at oil/water interfaces of increasing curvature. The NPs have aspect ratio 4. The area per NP is constant at $A_c \sim 24 R_c^2$. Left and right panels are for NPs with N=30 and N=70, respectively. Panels (a) and (d) are for flat interface; (b) and (e) for a droplet of diameter $d=75R_c$; (c) and (f) for a droplet of diameter $d=20R_c$

For the NPs of aspect ratio c/b=4 and N=30 adsorbed on an oil droplet we systematically changed the droplet size. From an experimental point of view, the droplet size could change during evaporation processes, during which the droplet size changes with time.[171] In **Figure 5.7** we report the average orientation angle, α, as a function of the area per NP. The orientation angles at low surface density are similar for all droplet diameters, and it reduces as the area per particle decreases. The effect is more pronounced for smaller droplets. For example, as A_c reduces from A_c=90 to $20\,R_c^2$, the orientation angles reduce by about $40°$ when the NPs are adsorbed on droplets of diameter d=20 and 50 R_c, and only by about $20°$ when the droplet diameter is d=75R_c, or larger (see limit for flat interface). These results suggest that curvature has a considerable effect on the particles behavior when droplet diameter is 50 R_C or less.

We complement our analysis by drawing a 'master curve' (solid line) in **Figure 5.7**. This curve identifies three regions corresponding to three NP structures, i.e., isotropic (Region 1), axial nematic domains (Region 2), and radial nematic (Region 3). In each region, the line was obtained by the least square method from the correspondent simulation results. In Region 1 the NP surface density has a negligible effect on the averaged orientation angle. In Region 2 the averaged orientation angle decreases as the NP surface density increases, but the change never exceeds $20°$, and it is not uniform for all the particles on a droplet (because of the formation of the axial nematic domains). In Region 3, upon the formation of the radial nematic structure, the averaged orientation angle can change up to $\sim 40°$ with a small change in NP surface density.

The results just discussed are most likely dependent on the NP features. In **Figure 5S.3** of the Appendix we report simulation results for NPs of aspect ratio 4 and

with N=70 adsorbed on either a flat oil-water interface, or on one oil droplet of diameter $d=50R_C$. As the NP surface density increases, the orientation angle is never less than 40°, and the change in orientation angle due to increasing surface density is of at most ~20°. This happens because the NPs considered do not yield the radial nematic structure at the conditions considered in our simulations.

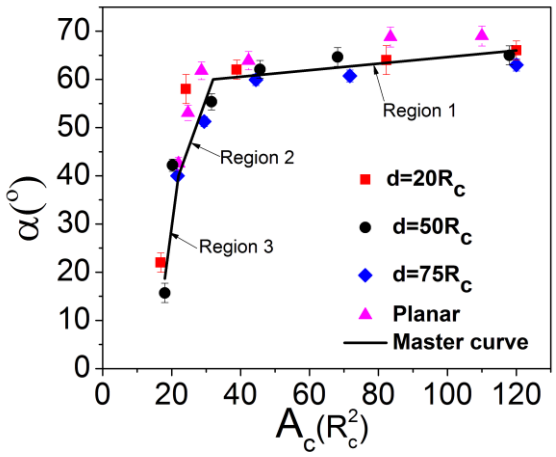

Figure 5.7. Average orientation angle as a function of area per NP. Results are for NPs with aspect ratio c/b=4 and N=30. Different symbols are for different droplet diameters. The error bars are obtained as one standard deviation from the average of three simulations. The solid line is a 'master curve', which can be divided into three regions. See text for a discussion.

5.4.2. Water Droplets Immersed in Oil

When the NPs are adsorbed on water droplets immersed in oil the simulation results are qualitatively similar to those discussed above for oil droplets immersed in water. In supplemental material we provide the relevant information (**Table 5S.1** and **Figures 5S.4-5S.6**). However, there are a few differences. The NPs were found to show only one preferred orientation angle when adsorbed on oil droplets regardless of droplet sizes, NPs type, and surface densities. When NPs of small aspect ratio (c/b=2) adsorb on

water droplets, they also show only one preferred orientation angle (see **Figure 5S.4**). However, when NPs of high aspect ratio (c/b=4) adsorb on water droplets, they can exhibit two preferred orientation angles (see **Figure 5S.5**). To qualify this phenomenon we computed the probability distribution function (PDF) of orientation angle α (see **Figure 5.8)**. We show results for NPs with c/b=4 and N=30 (panel a) and N=70 (panel b). The droplet diameter is ~40R_c. For the NPs with N=30 we observe preferential orientations at $\alpha \sim 75°$ and $\alpha \sim 15°$, with their prevalence depending on surface density (as the density increases the prevalence of the small angle increases). Sequences of visualization snapshots (see, e.g., **Figure 5S.5**) show that these NPs can dynamically change their preferential orientation during the length of our simulations, suggesting that the results are not due to long-lived metastable states. When the surface density of the NPs is increased (see simulation snapshots in **Figure 5S.6**) two preferential orientations might be needed to accommodate the structure of the NPs on the droplet surface. When NP surface density is sufficiently high, N=70 NPs are observed to yield radial nematic phase (**Figure 5S6**). This is not documented when droplet is oil.

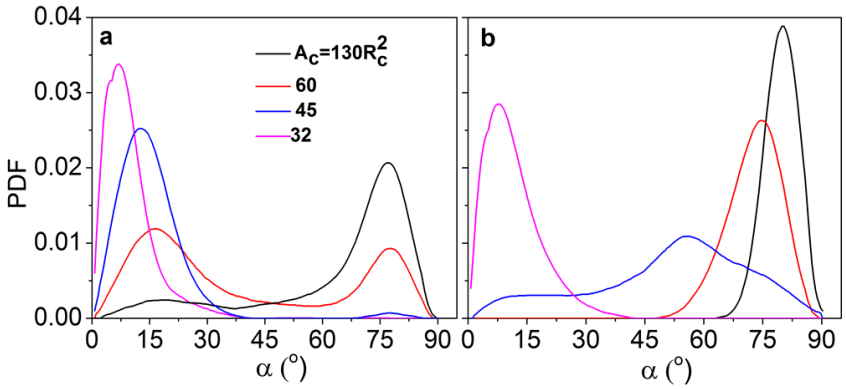

Figure 5.8. Probability density distribution (PDF) of the orientation angle of ellipsoidal Janus NPs of aspect ratio 4 adsorbed on a water droplet of diameter d=40R_c. Panels (a) and (b) are for N=30 and N=70, respectively. Different lines are for different NP surface densities, A_c.

5.5.Discussion

When adsorbed at the flat oil/water interface, NPs arrange to (1) minimize the interfacial energy, (2) minimize particle-particle and particle-solvent interactions, and (3) maximize the system entropy.[150,160] Similar arguments hold for the attachment of particles to spherical interfaces, with the difference that the interfacial curvature is also responsible of the Laplace pressure, which the particles respond to. The attachment energy for one NP moving from the oil phase to a spherical interface can be derived as (see SI):

$$\Delta E = -\gamma(S_{ap-w}\cos\theta_a + S_{p-w}\cos\theta_p + S_I) + \frac{2\varepsilon\gamma}{R}V_{NP-w} \qquad (5.2)$$

In Eq. (5.2), S_{p-w}, S_{ap-w}, and S_I are the NP polar area immersed in water, NP nonpolar area immersed in water, and droplet interfacial area occupied by the NP, respectively. θ_a and θ_p are the three phases contact angles of a spherical NP when its surface is totally covered by nonpolar and polar beads, respectively. See **Figure 5.2** for a schematic for the various geometrical terms. γ is the oil/water interfacial tension. ε is -1 for an oil droplet in water, and 1 for a water droplet in oil. $V_{NP\text{-}w}$ is the NP volume immersed in water. R is the droplet radius. The parenthetical terms represent the attachment energy when the interface is flat, while the last term represents the contribution of the Laplace pressure.

The change in NP structure in **Figure 5.5** (isotropic - axial nematic domains - radial nematic) as NP surface density increases is rationalized by the entropic effect, attachment energy reduction and steric effect. The entropic effect is responsible for the change from isotropic phase to the axial nematic domain structure. This transition is

reminiscent of the one from isotropic to axial nematic we documented on flat interfaces,[160] and it is due to the curvature of the interface.

The transition between axial nematic domains to radial nematic phase that occurs for N=30 NPs (panel (c) in **Figure 5.5**) is due to both energetic and steric effects. As all the particles assume low orientation angles, they reduce steric repulsions among themselves, and they also increase the polar NP surface area exposed to water and the apolar one exposed to the oil phase. Note that in the radial nematic phase, most of N=30 NPs are immersed in water, outside of the droplet.

The transformation to radial nematic phase only occurs when the droplet is sufficiently small, and the appropriate NPs are used (c/b=4 and N=30 for the simulations of **Figure 5.6**). This suggests that the radial nematic phase is due to a combination of steric effects and Laplace pressure contributions, both maximized in small droplets when the particles are largely immersed in the surrounding continuous phase.

Park et al.,[150] showed that an ellipsoidal Janus NP adsorbed at the flat oil/water interface can show two preferential orientation angles, correspondent to the energy wells. One energy well is a consequence of NP maximizing the interfacial area occupied, S_I (large angle), the other corresponds to the NP minimizing the interactions with the solvents (low angle). A particle can move from one preferential orientation to the other if the energy barrier between the two energy wells is not too high. Our previous results for NPs at a flat oil-water interface suggested that, under the simulated conditions, the NPs only showed one preferential orientation angle.[160] The results shown in **Figure 5.8** show that when the NPs are adsorbed on a water droplet, they can change their preferential orientation. This suggests that for this system the energy barrier

separating the two wells (low and high orientation angle) is not too high. This is probably a due to both particle-fluid interactions and to the Laplace pressure contribution to Eq. (5.2). When NP density is sufficiently high, N=70 NPs can yield radial nematic phases because both energetic and steric effects are favorable. Note that most part of N=70 NPs are immersed in oil, outside the droplet.

5.6.Conclusions

The structures of prolate Janus nanoparticles assembled at spherical oil/water interfaces were investigated using dissipative particle dynamics simulations. These structures were found to depend on nanoparticle characteristics (aspect ratio, surface chemistry, and surface density) and the properties of the droplets (curvature and liquid type). The structure of NPs can be either isotropic, radial nematic phases or axial nematic domains. The entropic effect, tendency to reduce attachment energy, and steric effect are responsible for the formation of these structures. Our findings can contribute in enhancing the stability of Pickering emulsions stability and designing novel materials via evaporation and crystallization.

Chapter 6. Conclusions and Future Work

This thesis investigated the effect of nanoparticle (NP) surface chemistry, shape, concentration, composition and the curvature of the interface on the behavior of nanoparticles. We focused on the following objectives:

- NP surface density and composition effect on structure and diffusion of spherical NPs when they adsorbed at the flat oil/water interface.
- Some evidence of emergent behavior of ellipsoidal Janus NPs adsorbed at the flat oil/water interface.
- Ellipsoidal Janus nanoparticles assembled at the spherical oil/water interfaces.

On the first objective, the analysis of the behavior of spherical NPs adsorbed at the flat oil/water interface provides insights on their structure and diffusion. We found that the structure of NPs changes from liquid-like to hexagonal solid-like as NP surface density increases. NPs can reduce interfacial tension provided that the NP surface density is high and the interactions between NPs are repulsive. Janus NPs are better at reducing interfacial tension than homogeneous NPs. The simulation results for mixture of NPs indicate that the self-diffusion coefficient is not a monotonic function of mixture composition. These finding may help enhance the efficiency of using nanoparticles in Pickering emulsions, including using several different types of NPs to stabilize emulsions.

On the second object, we focused on ellipsoidal Janus NPs adsorbed at the flat oil/water interface. The orientation of NPs with respect to the interface was found to depend on NP surface chemistry, aspect ratio and NP surface density. For prolate Janus

NPs with aspect ratio of 4, our results show an isotropic-nematic phase transition as NP surface density increases. This is the results of the entropic effects. These findings are helpful in Pickering emulsion and new material synthesis.

On the final objective, we investigated the behavior of ellipsoidal Janus NPs when adsorbed at either oil or water droplet surfaces. It is found that isotropic and radial nematic phases, and sometimes, axial nematic domains were formed depending NP characteristics (aspect ratio, amount of nonpolar beads on their surface), NP surface density, curvature of the interface and liquid type. NPs are found to have only one orientation angle when adsorbed on the oil droplet surfaces. On the contrary, NPs can switch between two orientation angle when adsorbed on water droplets, provided that NP aspect ratio is sufficiently high and the amount of nonpolar beads on their surface is small. Our finding could be helpful in interpreting the results of using ellipsoidal NPs to stabilize emulsions as well as the structure of non-spherical NPs when adsorbed at the curved surfaces.

There are many topics can be built on our thesis. One possible direction is to investigate the stability of emulsions stabilized by ellipsoidal Janus NPs. The interesting question could be how the change in the orientation angle affects the thin film around the droplet, and hence affect the coalescence. Another possible topic is to investigate the 'bridging nanoparticle' where NPs can act like a bridge between two droplets. These NPs may have homogeneous surface chemistry. A flocculation may occur when NPs have this ability.

References

(1) Silva, H.; Cerqueira, M.; Vicente, A. Nanoemulsions for Food Applications: Development and Characterization. *Food Bioprocess Technol* **2012**, *5*, 854-867.

(2) Jafari, S. M.; He, Y.; Bhandari, B. Production of sub-micron emulsions by ultrasound and microfluidization techniques. *J. Food Eng.* **2007**, *82*, 478-488.

(3) Gilbert, L.; Savary, G.; Grisel, M.; Picard, C. Predicting sensory texture properties of cosmetic emulsions by physical measurements. *Chemom. Intell. Lab. Syst.* **2013**, *124*, 21-31.

(4) Frelichowska, J.; Bolzinger, M.-A.; Pelletier, J.; Valour, J.-P.; Chevalier, Y. Topical delivery of lipophilic drugs from o/w Pickering emulsions. *Int. J. Pharm.* **2009**, *371*, 56-63.

(5) Zhang, T.; Davidson, D.; Bryant, S. L.; Huh, C.: Nanoparticle-Stabilized Emulsions for Applications in Enhanced Oil Recovery. SPE, 2010; Vol. 129885; pp 1-18.

(6) Wang, X.; Alvarado, V.: Effect of Salinity and pH on Pickering Emulsion Stability. SPE, 2008; Vol. 115941; pp 1-17.

(7) Jiang, Y.; Liu, X.; Chen, Y.; Zhou, L.; He, Y.; Ma, L.; Gao, J. Pickering emulsion stabilized by lipase-containing periodic mesoporous organosilica particles: A robust biocatalyst system for biodiesel production. *Bioresour. Technol.* **2014**, *153*, 278-283.

(8) Crossley, S.; Faria, J.; Shen, M.; Resasco, D. E. Solid Nanoparticles that Catalyze Biofuel Upgrade Reactions at the Water/Oil Interface. *Science* **2010**, *327*, 68-72.

(9) van Wijk, J.; Salari, J. W. O.; Zaquen, N.; Meuldijk, J.; Klumperman, B. Poly(methyl methacrylate)-silica microcapsules synthesized by templating Pickering emulsion droplets. *J. Mater. Chem. B.* **2013**, *1*, 2394-2406.

(10) Salari, J. W. O.; van Heck, J.; Klumperman, B. Steric Stabilization of Pickering Emulsions for the Efficient Synthesis of Polymeric Microcapsules. *Langmuir* **2010**, *26*, 14929-14936.

(11) Pardhy, N. P.; Budhlall, B. M. Pickering Emulsion as a Template to Synthesize Janus Colloids with Anisotropy in the Surface Potential. *Langmuir* **2010**, *26*, 13130-13141.

(12) Dickinson, E.; Golding, M.; Povey, M. J. W. Creaming and Flocculation of Oil-in-Water Emulsions Containing Sodium Caseinate. *J. Colloid Interface Sci.* **1997**, *185*, 515-529.

(13) Frising, T.; Noïk, C.; Dalmazzone, C. The Liquid/Liquid Sedimentation Process: From Droplet Coalescence to Technologically Enhanced Water/Oil Emulsion Gravity Separators: A Review. *J. Dispersion Sci. Technol.* **2006**, *27*, 1035-1057.

(14) Simovic, S.; Prestidge, C. A. Nanoparticles of Varying Hydrophobicity at the Emulsion Droplet−Water Interface: Adsorption and Coalescence Stability. *Langmuir* **2004**, *20*, 8357-8365.

(15) Taylor, P. Ostwald ripening in emulsions. *Adv. Colloid Interface Sci.* **1998**, *75*, 107-163.

(16) Ramsden, W. Separation of solids in the surface-layers of solutions and 'Suspensions' (Observations on surface-membranes, bubbles, emulsions, and mechanical coagulation). *Proc. R. Soc. London* **1903**, *72*, 156-164.

(17) Briggs, T. R. Emulsions with Finely Divided Solids. *Ind. Eng. Chem. Res.* **1921**, *13*, 1008-1010.

(18) Pickering, S. U. CXCVI.-Emulsions. *J. Chem. Soc. Faraday Trans.* **1907**, *91*, 2001-2021.

(19) Abend, S.; Bonnke, N.; Gutschner, U.; Lagaly, G. Stabilization of emulsions by heterocoagulation of clay minerals and layered double hydroxides. *Colloid Polym Sci* **1998**, *276*, 730-737.

(20) Brandenburg, U.; Lagaly, G. Rheological properties of sodium montmorillonite dispersions. *Applied Clay Science* **1988**, *3*, 263-279.

(21) Saleh, N.; Phenrat, T.; Sirk, K.; Dufour, B.; Ok, J.; Sarbu, T.; Matyjaszewski, K.; Tilton, R. D.; Lowry, G. V. Adsorbed Triblock Copolymers Deliver Reactive Iron Nanoparticles to the Oil/Water Interface. *Nano Letters* **2005**, *5*, 2489-2494.

(22) Zoppe, J. O.; Venditti, R. A.; Rojas, O. J. Pickering emulsions stabilized by cellulose nanocrystals grafted with thermo-responsive polymer brushes. *J. Colloid Interface Sci.* **2012**, *369*, 202-209.

(23) Perino, A.; Noïk, C.; Dalmazzone, C. Effect of Fumed Silica Particles on Water-in-Crude Oil Emulsion: Emulsion Stability, Interfacial Properties, and Contribution of Crude Oil Fractions. *Energy & Fuels* **2013**, *27*, 2399-2412.

(24) Nourani, M.; Tichelkamp, T.; Gaweł, B.; Øye, G. Method for Determining the Amount of Crude Oil Desorbed from Silica and Aluminosilica Surfaces upon Exposure to Combined Low-Salinity Water and Surfactant Solutions. *Energy & Fuels* **2014**, *28*, 1884-1889.

(25) Faria, J.; Ruiz, M. P.; Resasco, D. E. Phase-Selective Catalysis in Emulsions Stabilized by Janus Silica-Nanoparticles. *Adv. Synth. Catal.* **2010**, *352*, 2359-2364.

(26) He, Y. Preparation and modification of ZnO microspheres using a Pickering emulsion as template. *Materials Letters* **2005**, *59*, 114-117.

(27) Li, J.; Stöver, H. D. H. Correction to Pickering Emulsion Templated Layer-by-Layer Assembly for Making Microcapsules. *Langmuir* **2010**, *27*, 861-861.

(28) Li, J.; Stöver, H. D. H. Pickering Emulsion Templated Layer-by-Layer Assembly for Making Microcapsules. *Langmuir* **2010**, *26*, 15554-15560.

(29) Meng, G.; Paulose, J.; Nelson, D. R.; Manoharan, V. N. Elastic Instability of a Crystal Growing on a Curved Surface. *Science* **2014**, *343*, 634-637.

(30) Vaughan, O. Crystals: Growth on a curve. *Nat Nano* **2014**.

(31) P. Binks, B.; O. Lumsdon, S. Stability of oil-in-water emulsions stabilised by silica particles. *Phys. Chem. Chem. Phys.* **1999**, *1*, 3007-3016.

(32) Binks, B. P.; Lumsdon, S. O. Catastrophic Phase Inversion of Water-in-Oil Emulsions Stabilized by Hydrophobic Silica. *Langmuir* **2000**, *16*, 2539-2547.

(33) Binks, B. P.; Lumsdon, S. O. Transitional Phase Inversion of Solid-Stabilized Emulsions Using Particle Mixtures. *Langmuir* **2000**, *16*, 3748-3756.

(34) Saigal, T.; Dong, H.; Matyjaszewski, K.; Tilton, R. D. Pickering Emulsions Stabilized by Nanoparticles with Thermally Responsive Grafted Polymer Brushes. *Langmuir* **2010**, *26*, 15200-15209.

(35) Alvarez, N. J.; Anna, S. L.; Saigal, T.; Tilton, R. D.; Walker, L. M. Interfacial Dynamics and Rheology of Polymer-Grafted Nanoparticles at Air–Water and Xylene–Water Interfaces. *Langmuir* **2012**, *28*, 8052-8063.

(36) Li, J.; Stöver, H. D. H. Doubly pH-Responsive Pickering Emulsion. *Langmuir* **2008**, *24*, 13237-13240.

(37) Saleh, N.; Sarbu, T.; Sirk, K.; Lowry, G. V.; Matyjaszewski, K.; Tilton, R. D. Oil-in-Water Emulsions Stabilized by Highly Charged Polyelectrolyte-Grafted Silica Nanoparticles†. *Langmuir* **2005**, *21*, 9873-9878.

(38) Aveyard, R. Can Janus particles give thermodynamically stable Pickering emulsions? *Soft Matter* **2012**, *8*, 5233-5240.

(39) Fan, H.; Striolo, A. Nanoparticle effects on the water-oil interfacial tension. *Phys. Rev. E* **2012**, *86*, 051610.

(40) Levine, S.; Bowen, B. D.; Partridge, S. J. Stabilization of emulsions by fine particles I. Partitioning of particles between continuous phase and oil/water interface. *Colloids Surf.* **1989**, *38*, 325-343.

(41) Tambe, D. E.; Sharma, M. M. Factors Controlling the Stability of Colloid-Stabilized Emulsions: I. An Experimental Investigation. *J. Colloid Interface Sci.* **1993**, *157*, 244-253.

(42) Tu, F.; Park, B. J.; Lee, D. Thermodynamically Stable Emulsions Using Janus Dumbbells as Colloid Surfactants. *Langmuir* **2013**, *29*, 12679-12687.

(43) Hunter, T. N.; Pugh, R. J.; Franks, G. V.; Jameson, G. J. The role of particles in stabilising foams and emulsions. *Adv. Colloid Interface Sci.* **2008**, *137*, 57-81.

(44) Fan, H.; Striolo, A. Mechanistic Study of Droplets Coalescence in Pickering Emulsions. *Soft Matter* **2012**, *8*, 9533-9538.

(45) Aveyard, R.; Binks, B. P.; Clint, J. H. Emulsions stabilised solely by colloidal particles. *Adv. Colloid Interface Sci.* **2003**, *100–102*, 503-546.

(46) Binks, B. P.; Whitby, C. P. Nanoparticle silica-stabilised oil-in-water emulsions: improving emulsion stability. *Colloids Surf A Physicochem Eng Asp* **2005**, *253*, 105-115.

(47) Binks, B. P.; Lumsdon, S. O. Pickering Emulsions Stabilized by Monodisperse Latex Particles: Effects of Particle Size. *Langmuir* **2001**, *17*, 4540-4547.

(48) Wang, W.; Zhou, Z.; Nandakumar, K.; Xu, Z.; Masliyah, J. H. Effect of charged colloidal particles on adsorption of surfactants at oil–water interface. *J. Colloid Interface Sci.* **2004**, *274*, 625-630.

(49) Horozov, T. S.; Binks, B. P. Particle-Stabilized Emulsions: A Bilayer or a Bridging Monolayer? *Angewandte Chemie* **2006**, *118*, 787-790.

(50) Binks, B. P. Colloidal particles at liquid interfaces. *Phys. Chem. Chem. Phys.* **2007**, *9*, 6298-6299.

(51) Vignati, E.; Piazza, R.; Lockhart, T. P. Pickering Emulsions: Interfacial Tension, Colloidal Layer Morphology, and Trapped-Particle Motion. *Langmuir* **2003**, *19*, 6650-6656.

(52) Binks, B. P.; Fletcher, P. D. I. Particles Adsorbed at the Oil−Water Interface: A Theoretical Comparison between Spheres of Uniform Wettability and “Janus” Particles. *Langmuir* **2001**, *17*, 4708-4710.

(53) Park, B. J.; Lee, D. Equilibrium Orientation of Nonspherical Janus Particles at Fluid–Fluid Interfaces. *ACS Nano* **2011**, *6*, 782-790.

(54) Park, B. J.; Choi, C.-H.; Kang, S.-M.; Tettey, K. E.; Lee, C.-S.; Lee, D. Geometrically and chemically anisotropic particles at an oil-water interface. *Soft Matter* **2013**, *9*, 3383-3388.

(55) Mejia, A. F.; Diaz, A.; Pullela, S.; Chang, Y.-W.; Simonetty, M.; Carpenter, C.; Batteas, J. D.; Mannan, M. S.; Clearfield, A.; Cheng, Z. Pickering emulsions stabilized by amphiphilic nano-sheets. *Soft Matter* **2012**, *8*, 10245-10253.

(56) Boode, K.; Walstra, P. Partial coalescence in oil-in-water emulsions 1. Nature of the aggregation. *Colloids Surf A Physicochem Eng Asp* **1993**, *81*, 121-137.

(57) Madivala, B.; Vandebril, S.; Fransaer, J.; Vermant, J. Exploiting Particle Shape in Solid Stabilized Emulsions. *Soft Matter* **2009**, *5*, 1717-1727.

(58) Kalashnikova, I.; Bizot, H.; Bertoncini, P.; Cathala, B.; Capron, I. Cellulosic nanorods of various aspect ratios for oil in water Pickering emulsions. *Soft Matter* **2013**, *9*, 952-959.

(59) Binks, B. P.; Lumsdon, S. O. Effects of oil type and aqueous phase composition on oil-water mixtures containing particles of intermediate hydrophobicity. *Phys. Chem. Chem. Phys.* **2000**, *2*, 2959-2967.

(60) Frelichowska, J.; Bolzinger, M.-A.; Chevalier, Y. Pickering emulsions with bare silica. *Colloids Surf A Physicochem Eng Asp* **2009**, *343*, 70-74.

(61) Midmore, B. R. Effect of Aqueous Phase Composition on the Properties of a Silica-Stabilized W/O Emulsion. *J. Colloid Interface Sci.* **1999**, *213*, 352-359.

(62) Lagerwall, J. P. F.; Scalia, G. A new era for liquid crystal research: Applications of liquid crystals in soft matter nano-, bio- and microtechnology. *Curr. Appl Phys* **2012**, *12*, 1387-1412.

(63) Groot, R. D.; Warren, P. B. Dissipative particle dynamics: Bridging the gap between atomistic and mesoscopic simulation. *J. Chem. Phys.* **1997**, *107*, 4423-4435.

(64) Groot, R. D.; Rabone, K. L. Mesoscopic Simulation of Cell Membrane Damage, Morphology Change and Rupture by Nonionic Surfactants. *Biophys. J.* **2001**, *81*, 725-736.

(65) Plimpton, S. Fast parallel algorithms for short-range molecular-dynamics. *J. Comput. Phys.* **1995**, *117*, 1-19.

(66) Fan, H.; Striolo, A. Nanoparticles Effects on Water-Oil Interfacial Tension. *Phys. Rev. E* **2012**.

(67) Calvaresi, M.; Dallavalle, M.; Zerbetto, F. Wrapping Nanotubles with Micelles, Hemimicelles, and Cylindrical Micelles. *Small* **2009**, *5*, 2191-2198.

(68) Groot, R. D.; Warren, P. B. Dissipative Particle Dynamics: Bridging the Gap between Atomistic and Mesoscopic Simulation. *J. Chem. Phys.* **1997**, *107*, 4423-4435.

(69) Fan, H.; Resasco, D. E.; Striolo, A. Amphiphilic Silica Nanoparticles at the Decane-Water Interface: Insights from Atomistic Simulations. *Langmuir* **2011**, *27*, 5264-5274.

(70) Jakobsen, A. F.; Mouritsen, O. G.; Besold, G. Artifacts in dynamical simulations of coarse-grained model lipid bilayers. *J. Chem. Phys.* **2005**, *122*.

(71) Pickering, S. U. CXCVI.-Emulsions. *J. Chem. Soc. Trans.* **1907**, *91*, 2001-2021.

(72) Kokal, S. Crude-oil emulsions: A state-of-the-art review. *SPE Prod. Fac.* **2005**, *20*, 5-13.

(73) Gu, G.; Zhou, Z.; Xu, Z.; Masliyah, J. H. Role of fine kaolinite clay in toluene-diluted bitumen/water emulsion. *Colloids Surf A Physicochem Eng Asp* **2003**, *215*, 141-153.

(74) Drexler, S.; Faria, J.; Ruiz, M. P.; Harwell, J. H.; Resasco, D. E. Amphiphilic Nanohybrid Catalysts for Reactions at the Water/Oil Interface in Subsurface Reservoirs. *Energy & Fuels* **2012**, *26*, 2231-2241.

(75) Angelova, A.; Angelov, B.; Mutafchieva, R.; Lesieur, S.; Couvreur, P. Self-Assembled Multicompartment Liquid Crystalline Lipid Carriers for Protein, Peptide, and Nucleic Acid Drug Delivery. *Accounts Chem. Res.* **2011**, *44*, 147-156.

(76) Shchukina, E. M.; Shchukin, D. G. Layer-by-layer coated emulsion microparticles as storage and delivery tool. *Curr. Opin. Colloid Interface Sci.* **2012**, *17*, 281-289.

(77) Puglia, C.; Bonina, F. Lipid nanoparticles as novel delivery systems for cosmetics and dermal pharmaceuticals. *Expert Opin. Drug Deliv.* **2012**, *9*, 429-441.

(78) Binks, B. P.; Horozov, T. S.: *Colloidal Particles at Liquid Interfaces*; Cambridge University Press, 2008.

(79) Glaser, N.; Adams, D. J.; Böker, A.; Krausch, G. Janus Particles at Liquid−Liquid Interfaces. *Langmuir* **2006**, *22*, 5227-5229.

(80) Zang, D. Y.; Rio, E.; Delon, G.; Langevin, D.; Wei, B.; Binks, B. P. Influence of the contact angle of silica nanoparticles at the air-water interface on the mechanical properties of the layers composed of these particles. *Mol. Phys.* **2011**, *109*, 1057-1066.

(81) Safouane, M.; Langevin, D.; Binks, B. P. Effect of particle hydrophobicity on the properties of silica particle layers at the air-water interface. *Langmuir* **2007**, *23*, 11546-11553.

(82) Miller, R.; Fainerman, V. B.; Kovalchuk, V. I.; Grigoriev, D. O.; Leser, M. E.; Michel, M. Composite interfacial layers containing micro-size and nano-size particles. *Adv. Colloid and Interface Sci.* **2006**, *128–130*, 17-26.

(83) Blute, I.; Pugh, R. J.; van de Pas, J.; Callaghan, I. Industrial manufactured silica nanoparticle sols. 2: Surface tension, particle concentration, foam generation and stability. *Colloids Surf A Physicochem Eng Asp* **2009**, *337*, 127-135.

(84) Comeau, K. D.; Meli, M. V. Effect of Alkanethiol Chain Length on Gold Nanoparticle Monolayers at the Air–Water Interface. *Langmuir* **2011**, *28*, 377-381.

(85) Pichot, R.; Spyropoulos, F.; Norton, I. T. Competitive adsorption of surfactants and hydrophilic silica particles at the oil-water interface: Interfacial tension and contact angle studies. *J. Colloid Interface Sci.* **2012**, *377*, 396-405.

(86) Tigges, B.; Dederichs, T.; Moller, M.; Liu, T. T.; Richtering, W.; Weichold, O. Interfacial Properties of Emulsions Stabilized with Surfactant and Nonsurfactant Coated Boehmite Nanoparticles. *Langmuir* **2010**, *26*, 17913-17918.

(87) Wang, D.; Yordanov, S.; Paroor, H. M.; Mukhopadhyay, A.; Li, C. Y.; Butt, H.-J.; Koynov, K. Probing Diffusion of Single Nanoparticles at Water–Oil Interfaces. *Small* **2011**, *7*, 3502-3507.

(88) Zahn, K.; MendezAlcaraz, J. M.; Maret, G. Hydrodynamic interactions may enhance the self-diffusion of colloidal particles. *Phys. Rev. Lett.* **1997**, *79*, 175-178.

(89) Cheung, D. L. Molecular Simulation of Nanoparticle Diffusion at Fluid Interfaces. *Chem. Phys. Lett.* **2010**, *495*, 55-59.

(90) Weeks, E. R.; Weitz, D. A. Subdiffusion and the cage effect studied near the colloidal glass transition. *Chem. Phys* **2002**, *284*, 361-367.

(91) Sonnenburg, J.; Kremp, D.; Sandig, R. Diffusion-processes in brownian particle-systems with short-range interaction. *Mol. Phys.* **1991**, *74*, 649-664.

(92) Peng, Y.; Chen, W.; Fischer, T. M.; Weitz, D. A.; Tong, P. Short-time self-diffusion of nearly hard spheres at an oil-water interface. *J. Fluid Mech.* **2009**, *618*, 243-261.

(93) Cheng, S. F.; Grest, G. S. Structure and diffusion of nanoparticle monolayers floating at liquid/vapor interfaces: A molecular dynamics study. *J. Chem. Phys.* **2012**, *136*.

(94) Alba-Simionesco, C.; Coasne, B.; Dosseh, G.; Dudziak, G.; Gubbins, K. E.; Radhakrishnan, R.; Sliwinska-Bartkowiak, M. Effects of confinement on freezing and melting. *J. Phys.-Condes. Matter* **2006**, *18*, R15-R68.

(95) Garbin, V.; Crocker, J. C.; Stebe, K. J. Nanoparticles at fluid interfaces: Exploiting capping ligands to control adsorption, stability and dynamics. *J. Colloid Interface Sci.* **2012**, *387*, 1-11.

(96) Luo, M.; Dai, L. L. Molecular dynamics simulations of surfactant and nanoparticle self-assembly at liquid-liquid interfaces. *J. Phys.-Condes. Matter* **2007**, *19*.

(97) Luo, M. X.; Song, Y. M.; Dai, L. L. Heterogeneous or competitive self-assembly of surfactants and nanoparticles at liquid-liquid interfaces. *Mol. Simul.* **2009**, *35*, 773-784.

(98) Ma, H.; Luo, M. X.; Dai, L. L. Influences of surfactant and nanoparticle assembly on effective interfacial tensions. *Phys. Chem. Chem. Phys.* **2008**, *10*, 2207-2213.

(99) Nielsen, S. O.; Nguyen, C. T.; Ranatunga, U. Molecular dynamics simulations of nanoparticles and surfactants at oil/water interfaces: Chemisorption vs. physisorption. *Abstr. Pap. Am. Chem. Soc.* **2010**, *240*.

(100) Ranatunga, R.; Nguyen, C. T.; Wilson, B. A.; Shinoda, W.; Nielsen, S. O. Molecular dynamics study of nanoparticles and non-ionic surfactant at an oil-water interface. *Soft Matter* **2011**, *7*, 6942-6952.

(101) Walker, E. M.; Frost, D. S.; Dai, L. L. Particle self-assembly in oil-in-ionic liquid Pickering emulsions. *J. Colloid Interface Sci.* **2011**, *363*, 307-313.

(102) Hong, B.; Panagiotopoulos, A. Z. Molecular Dynamics Simulations of Silica Nanoparticles Grafted with Poly(ethylene oxide) Oligomer Chains. *J. Phys. Chem. B* **2012**, *116*, 2385-2395.

(103) Iacovella, C. R.; Glotzer, S. C. Phase behavior of ditethered nanospheres. *Soft Matter* **2009**, *5*, 4492-4498.

(104) Phillips, C. L.; Glotzer, S. C. Effect of nanoparticle polydispersity on the self-assembly of polymer tethered nanospheres. *J. Chem. Phys.* **2012**, *137*.

(105) Izvekov, S.; Violi, A.; Voth, G. A. Systematic coarse-graining of nanoparticle interactions in molecular dynamics simulation. *J. Phys. Chem. B* **2005**, *109*, 17019-17024.

(106) Song, Y. M.; Luo, M. X.; Dai, L. L. Understanding Nanoparticle Diffusion and Exploring Interfacial Nanorheology using Molecular Dynamics Simulations. *Langmuir* **2010**, *26*, 5-9.

(107) Ndoro, T. V. M.; Voyiatzis, E.; Ghanbari, A.; Theodorou, D. N.; Böhm, M. C.; Müller-Plathe, F. Interface of Grafted and Ungrafted Silica Nanoparticles with a

Polystyrene Matrix: Atomistic Molecular Dynamics Simulations. *Macromolecules* **2011**, *44*, 2316-2327.

(108) Alejandre, J.; Rivera, J. L.; Mora, M. A.; de la Garza, V. Force Field of Monoethanolamine. *J. Phys. Chem. B* **2000**, *104*, 1332-1337.

(109) Agod, A.; Nagy, N.; Hórvölgyi, Z. Modeling the Structure Formation of Particulate Langmuir Films: the Effect of Polydispersity. *Langmuir* **2007**, *23*, 5445-5451.

(110) Sun, J.; Stirner, T. Molecular Dynamics Simulation of the Surface Pressure of Colloidal Monolayers. *Langmuir* **2001**, *17*, 3103-3108.

(111) Perro, A.; Reculusa, S.; Ravaine, S.; Bourgeat-Lami, E.; Duguet, E. Design and synthesis of Janus micro- and nanoparticles. *J. Mater. Chem.* **2005**, *15*, 3745-3760.

(112) Deák, A.; Bancsi, B.; Tóth, A. L.; Kovács, A. L.; Hórvölgyi, Z. Complex Langmuir–Blodgett films from silica nanoparticles: An optical spectroscopy study. *Colloids Surf A Physicochem Eng Asp* **2006**, *278*, 10-16.

(113) Monteux, C.; Kirkwood, J.; Xu, H.; Jung, E.; Fuller, G. G. Determining the mechanical response of particle-laden fluid interfaces using surface pressure isotherms and bulk pressure measurements of droplets. *Phys. Chem. Chem. Phys.* **2007**, *9*, 6344-6350.

(114) Xin, Q.; Chen, Y.; Jin, Y.; Yang, Y. H. Bond-orientational order in melting of colloidal crystals. *J. Korean Phys. Soc.* **2006**, *49*, 1682-1686.

(115) Chakrabarti, J.; Löwen, H. Effect of confinement on charge-stabilized colloidal suspensions between two charged plates. *Phys. Rev. E* **1998**, *58*, 3400-3404.

(116) Okubo, T. Surface Tension of Structured Colloidal Suspensions of Polystyrene and Silica Spheres at the Air-Water Interface. *J. Colloid Interface Sci.* **1995**, *171*, 55-62.

(117) Ho, T. A.; Papavassiliou, D. V.; Lee, L. L.; Striolo, A. Liquid water can slip on a hydrophilic surface. *Proc. Natl. Acad. Sci. U. S. A.* **2011**, *108*, 16170-16175.

(118) Phan, A.; Ho, T. A.; Cole, D. R.; Striolo, A. Molecular Structure and Dynamics in Thin Water Films at Metal Oxide Surfaces: Magnesium, Aluminum, and Silicon Oxide Surfaces. *J. Phys. Chem. C* **2012**, *116*, 15962-15973.

(119) Lekkerkerker, H. N. W.; Dhont, J. K. G. On the calculation of the self-diffusion coefficient of interacting brownian particles. *J. Chem. Phys.* **1984**, *80*, 5790-5792.

(120) Kasper, A.; Bartsch, E.; Sillescu, H. Self-diffusion in concentrated colloid suspensions studied by digital video microscopy of core-shell tracer particles. *Langmuir* **1998**, *14*, 5004-5010.

(121) Faria, J.; Ruiz, M. P.; Resasco, D. E. Phase-Selective Catalysis in Emulsions Stabilized by Janus Silica-Nanoparticles. *Adv. Synth. Catal.* **2010**, *352*, 2359-2364.

(122) Zapata, P. A.; Faria, J.; Ruiz, M. P.; Jentoft, R. E.; Resasco, D. E. Hydrophobic Zeolites for Biofuel Upgrading Reactions at the Liquid-Liquid Interface in Water/Oil Emulsions. *J. Am. Chem. Soc.* **2012**, *134*, 8570-8578.

(123) Marku, D.; Wahlgren, M.; Rayner, M.; Sjöö, M.; Timgren, A. Characterization of Starch Pickering Emulsions for Potential Applications in Topical Formulations. *Int. J. Pharm.* **2012**, *428*, 1-7.

(124) Nonomura, Y.; Suzuki, M. Pickering Emulsions and Microcapsules Stabilized by Solid Particles and Biological Lipids. *Chem. Lett.* **2008**, *37*, 1196-1197.

(125) Kim, J. W.; Lee, D.; Shum, H. C.; Weitz, D. A. Colloid Surfactants for Emulsion Stabilization. *Adv. Mater.* **2008**, *20*, 3239-3243.

(126) Champion, J. A.; Katare, Y. K.; Mitragotri, S. Particle Shape: A New Design Parameter for Micro- and Nanoscale Drug Delivery Carriers. *J. Control. Release* **2007**, *121*, 3-9.

(127) Ruhland, T. M.; Gröschel, A. H.; Walther, A.; Müller, A. H. E. Janus Cylinders at Liquid–Liquid Interfaces. *Langmuir* **2011**, *27*, 9807-9814.

(128) Sacanna, S.; Rossi, L.; Philipse, A. P. Oil-in-water Emulsification Induced by Ellipsoidal Hematite Colloids: Evidence for Hydrolysis-Mediated Self-Assembly. *Langmuir* **2007**, *23*, 9974-9982.

(129) Xu, K.; Guo, R.; Dong, B.; Yan, L.-T. Directed Self-Assembly of Janus Nanorods in Binary Polymer Mixture: Towards Precise Control of Nanorod Orientation Relative to Interface. *Soft Matter* **2012**, *8*, 9581-9588.

(130) Laredj-Bourezg, F.; Chevalier, Y.; Boyron, O.; Bolzinger, M. A. Emulsions Stabilized with Organic Solid Particles. *Colloid Surf. A-Physicochem. Eng. Asp.* **2012**, *413*, 252-259.

(131) Lattuada, M.; Hatton, T. A. Synthesis, Properties and Applications of Janus Nanoparticles. *Nano Today* **2011**, *6*, 286-308.

(132) Isenbugel, K.; Gehrke, Y.; Ritter, H. Evaporation-Driven Self-Assembly of Colloidal Silica Dispersion: New Insights on Janus Particles. *Macromol. Rapid Commun.* **2012**, *33*, 41-46.

(133) Garbin, V.; Crocker, J. C.; Stebe, K. J. Nanoparticles at Fluid Interfaces: Exploiting Capping Ligands to Control Adsorption, Stability and Dynamics. *J. Colloid Interface Sci.* **2012**, *387*, 1-11.

(134) Casagrande, C.; Fabre, P.; Raphael, E.; Veyssie, M. Janus Beads - Realization and Behavior at Water Oil Interfaces. *Europhys. Lett.* **1989**, *9*, 251-255.

(135) Cheung, D. L.; Bon, S. A. F. Stability of Janus Nanoparticles at Fluid Interfaces. *Soft Matter* **2009**, *5*, 3969-3976.

(136) Jiang, S.; Chen, Q.; Tripathy, M.; Luijten, E.; Schweizer, K. S.; Granick, S. Janus Particle Synthesis and Assembly. *Adv. Mater.* **2010**, *22*, 1060-1071.

(137) Zhang, Z. L.; Glotzer, S. C. Self-assembly of Patchy Particles. *Nano Lett.* **2004**, *4*, 1407-1413.

(138) Park, B. J.; Choi, C.-H.; Kang, S.-M.; Tettey, K. E.; Lee, C.-S.; Lee, D. Geometrically and Chemically Anisotropic Particles at an Oil-Water Interface. *Soft Matter* **2013**, 3383-3388.

(139) Dendukuri, D.; Hatton, T. A.; Doyle, P. S. Synthesis and Self-assembly of Amphiphilic Polymeric Microparticles. *Langmuir* **2007**, *23*, 4669-4674.

(140) Kim, J. W.; Larsen, R. J.; Weitz, D. A. Synthesis of Nonspherical Colloidal Particles with Anisotropic Properties. *J. Am. Chem. Soc.* **2006**, *128*, 14374-14377.

(141) Tervoort, E.; Studart, A. R.; Denier, C.; Gauckler, L. J. Pickering Emulsions Stabilized by in situ Grown Biologically Active Alkyl Gallate Microneedles. *RSC Advances* **2012**, *2*, 8614-8618.

(142) Okubo, T. Surface Tension of Structured Colloidal Suspensions of Polystyrene and Silica Spheres at the Air-Water Interface. *J. Colloid Interface Sci.* **1995**, *171*, 55-62.

(143) Fan, H.; Resasco, D. E.; Striolo, A. Amphiphilic Silica Nanoparticles at the Decane−Water Interface: Insights from Atomistic Simulations. *Langmuir* **2011**, *27*, 5264-5274.

(144) Binks, B. P.; Fletcher, P. D. I. Particles Adsorbed at the Oil-Water Interface: A Theoretical Comparison between Spheres of Uniform Wettability and "Janus" Particles. *Langmuir* **2001**, *17*, 4708-4710.

(145) De Lara, L. S.; Michelon, M. F.; Metin, C. O.; Nguyen, Q. P.; Miranda, C. R. Interface Tension of Silica Hydroxylated Nanoparticle with Brine: A Combined Experimental and Molecular Dynamics Study. *J. Chem. Phys.* **2012**, *136*, 164702-164710.

(146) Luo, M.; Dai, L. L. Molecular Dynamics Simulations of Surfactant and Nanoparticle Self-assembly at Liquid–Lquid interfaces. *J. Phys.: Condens. Matter* **2007**, *19*, 375109-375123.

(147) Fan, H.; Striolo, A. Nanoparticle Effects on the Water-Oiil Interfacial Tension. *Phys. Rev. E* **2012**, *86*, 051610-051621.

(148) Luu, X.-C.; Yu, J.; Striolo, A.; . Nanoparticles Adsorbed at the Water/Oil Interface: Coverage and Composition Effects on Structure and Diffusion. *Langmuir* **2013**, *29*, 7221-7228.

(149) Ruhland, T. M.; Groschel, A. H.; Ballard, N.; Skelhon, T. S.; Walther, A.; Muller, A. H. E.; Bon, S. A. F. Influence of Janus Particle Shape on Their Interfacial Behavior at Liquid-Liquid Interfaces. *Langmuir* **2013**, *29*, 1388-1394.

(150) Park, B. J.; Lee, D. Configuration of Nonspherical Amphiphilic Particles at a FLuid-Fluid Interface. *Soft Matter* **2012**, *8*, 7690-7698.

(151) Park, B. J.; Lee, D. Equilibrium Orientation of Nonspherical Janus Particles at Fluid-Fluid Interfaces. *ACS Nano* **2012**, *6*, 782-790.

(152) Morgan, A. R.; Ballard, N.; Rochford, L. A.; Nurumbetov, G.; Skelhon, T. S.; Bon, S. A. F. Understanding the Multiple Orientations of Isolated Superellipsoidal Hematite Particles at the Oil-Water Interface. *Soft Matter* **2013**, *9*, 487-491.

(153) Satoh, A. Three-Dimentional Monte Carlo Simulations of Internal Aggregate Structures in a Colloidal Dispersion Composed of Rod-like Particles with Magnetic Moment Normal to the Particle Axis. *J. Colloid Interface Sci.* **2008**, *318*, 68-81.

(154) Alejandre, J.; Rivera, J. L.; Mora, M. A.; de la Garza, V. Force Field of Monoethanolamine. *J. Phys. Chem. B* **2000**, *104*, 1332-1337.

(155) Binks, B. P. Particles as surfactants—similarities and differences. *Curr. Opin. Colloid Interface Sci.* **2002**, *7*, 21-41.

(156) Sessa, M.; Balestrieri, M. L.; Ferrari, G.; Servillo, L.; Castaldo, D.; D'Onofrio, N.; Donsi, F.; Tsao, R. Bioavailability of encapsulated resveratrol into nanoemulsion-based delivery systems. *Food Chem.* **2014**, *147*, 42-50.

(157) Son, H.; Kim, H.; Lee, G.; Kim, J.; Sung, W. Enhanced oil recovery using nanoparticle-stabilized oil/water emulsions. *Korean J. Chem. Eng.* **2014**, *31*, 338-342.

(158) Luu, X.-C.; Yu, J.; Striolo, A. Nanoparticles Adsorbed at the Water/Oil Interface: Coverage and Composition Effects on Structure and Diffusion. *Langmuir* **2013**, *29*, 7221-7228.

(159) Dendukuri, D.; Hatton, T. A.; Doyle, P. S. Synthesis and Self-Assembly of Amphiphilic Polymeric Microparticles. *Langmuir* **2006**, *23*, 4669-4674.

(160) Luu, X.-C.; Yu, J.; Striolo, A. Ellipsoidal Janus Nanoparticles Adsorbed at the Water–Oil Interface: Some Evidence of Emergent Behavior. *J. Phys. Chem. B* **2013**, *117*, 13922-13929.

(161) Cheng, T.-L.; Wang, Y. U. Shape-anisotropic particles at curved fluid interfaces and role of Laplace pressure: A computational study. *J. Colloid Interface Sci.* **2013**, *402*, 267-278.

(162) Cui, M.; Emrick, T.; Russell, T. P. Stabilizing Liquid Drops in Nonequilibrium Shapes by the Interfacial Jamming of Nanoparticles. *Science* **2013**, *342*, 460-463.

(163) Guzowski, J.; Tasinkevych, M.; Dietrich, S. Capillary interactions in Pickering emulsions. *Phys. Rev. E.* **2011**, *84*, 031401-031412.

(164) Hirose, Y.; Komura, S.; Nonomura, Y. Adsorption of Janus particles to curved interfaces. *J. Chem. Phys.* **2007**, *127*, 054707-054713.

(165) Kralchevsky, P. A.; Ivanov, I. B.; Ananthapadmanabhan, K. P.; Lips, A. On the Thermodynamics of Particle-Stabilized Emulsions: Curvature Effects and Catastrophic Phase Inversion. *Langmuir* **2004**, *21*, 50-63.

(166) Leandri, J.; Wurger, A. Trapping energy of a spherical particle on a curved liquid interface. *J. Colloid Interface Sci.* **2013**, *405*, 249-255.

(167) Lewandowski, E. P.; Bernate, J. A.; Searson, P. C.; Stebe, K. J. Rotation and Alignment of Anisotropic Particles on Nonplanar Interfaces. *Langmuir* **2008**, *24*, 9302-9307.

(168) Fan, C.-p.; Stephen, M. J. Isotropic-Nematic Phase Transition in Liquid Crystals. *Phys. Rev. Lett.* **1970**, *25*, 500-503.

(169) Jayasri, D.; Sairam, T.; Murthy, K. P. N.; Sastry, V. S. S. Liquid crystal films on curved surfaces: An entropic sampling study. *Phys Stat Mech Appl* **2011**, *390*, 4549-4554.

(170) Bausch, A. R.; Bowick, M. J.; Cacciuto, A.; Dinsmore, A. D.; Hsu, M. F.; Nelson, D. R.; Nikolaides, M. G.; Travesset, A.; Weitz, D. A. Grain Boundary Scars and Spherical Crystallography. *Science* **2003**, *299*, 1716-1718.

(171) Bigioni, T. P.; Lin, X.-M.; Nguyen, T. T.; Corwin, E. I.; Witten, T. A.; Jaeger, H. M. Kinetically driven self assembly of highly ordered nanoparticle monolayers. *Nat Mater* **2006**, *5*, 265-270.

APPENDIX

A. Supporting Information for chapter 4

In the main text (see Figure 4.2) we defined the orientation angle α as the angle between the vector *n* normal to the interface and the unit vector along the axis c of one NP. In the main text we report the averaged orientation angle as obtained during our simulations. In addition, we calculated the probability distribution (P) of orientation angles for nanoparticles (NPs) with different geometries and surface chemistry. The results are plotted in Figure 4S.1 for all NPs considered in this work with nonpolar fraction x=30 and in Figure 4S.2 for all NPs with x=70. For every NP considered, our results show that the probability distribution is characterized by one clear maximum, although the distribution can in some cases be wide. This suggests that the averaged orientation angles reported in the main text representative of equilibrium conditions, and that some NPs oscillate more than others around their preferential orientation.

To understand the effect of bead-bead interactions on the averaged orientation angle, we conduced additional simulations in which the interaction parameter that describes the interactions between water (w) and nonpolar (ap) beads was changed systematically. The results are shown in Figure 4S.3. Note that all other interaction parameters shown in Table 2.1 of the main text have not been changed for these calculations. The w-ap interaction parameter is $178.5\,k_BT/R_c$ for the simulations discussed in the main text. This parameter was changed systematically from 158 to 198 k_BT/R_c for the simulations shown in Figure 4S.3. The results show that the orientation angle decreases as the w-ap interaction parameter increases.

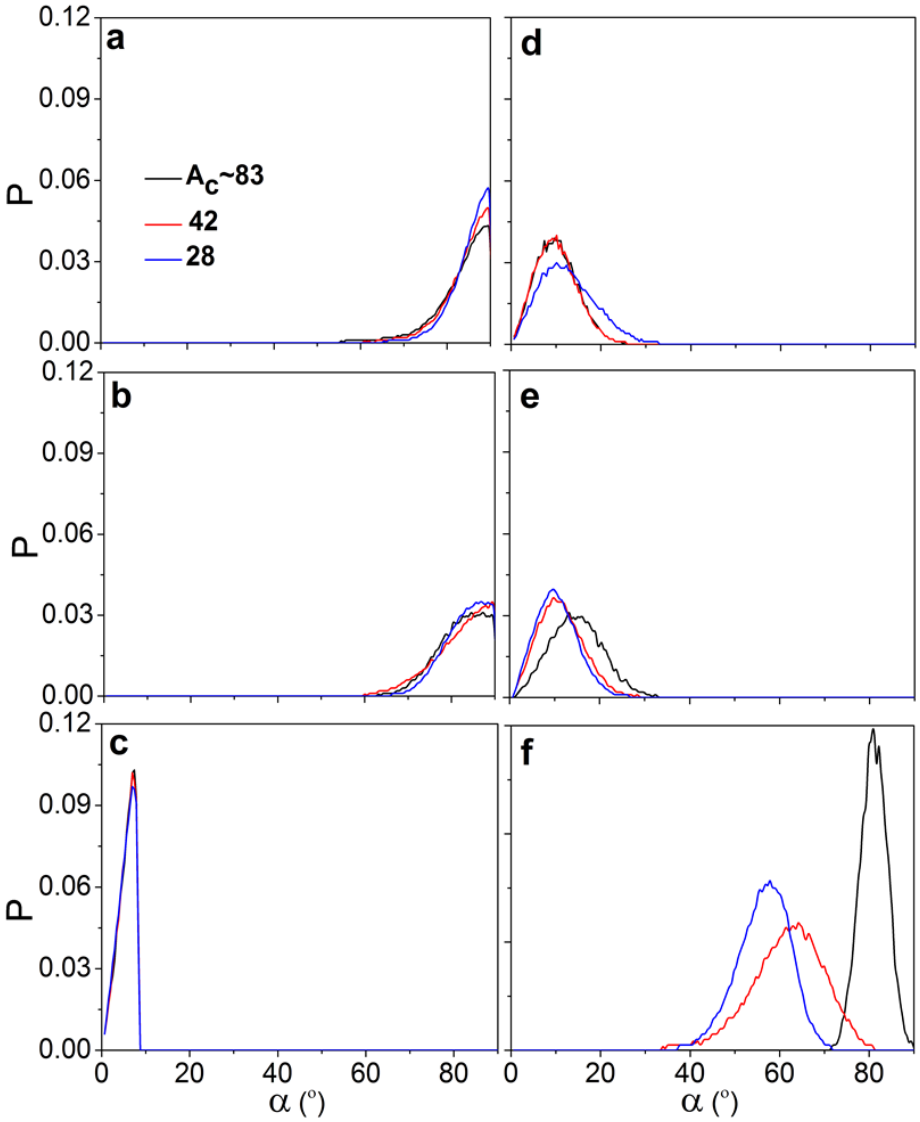

Figure 4S.1. Probability distribution of the orientation angle for ellipsoidal NPs at the water-decane interface. The results are obtained for NPs with nonpolar fraction x=30. Different panels are for different NPs. In each panel, three NP surface densities are presented. In some cases the lines overlap. Different panels are for NPs with different aspect ratio: (a) c/b=0.3; (b) c/b=0.5; (c) c/b=1; (d) c/b=1.5; (e) c/b=2; (f) c/b=4.

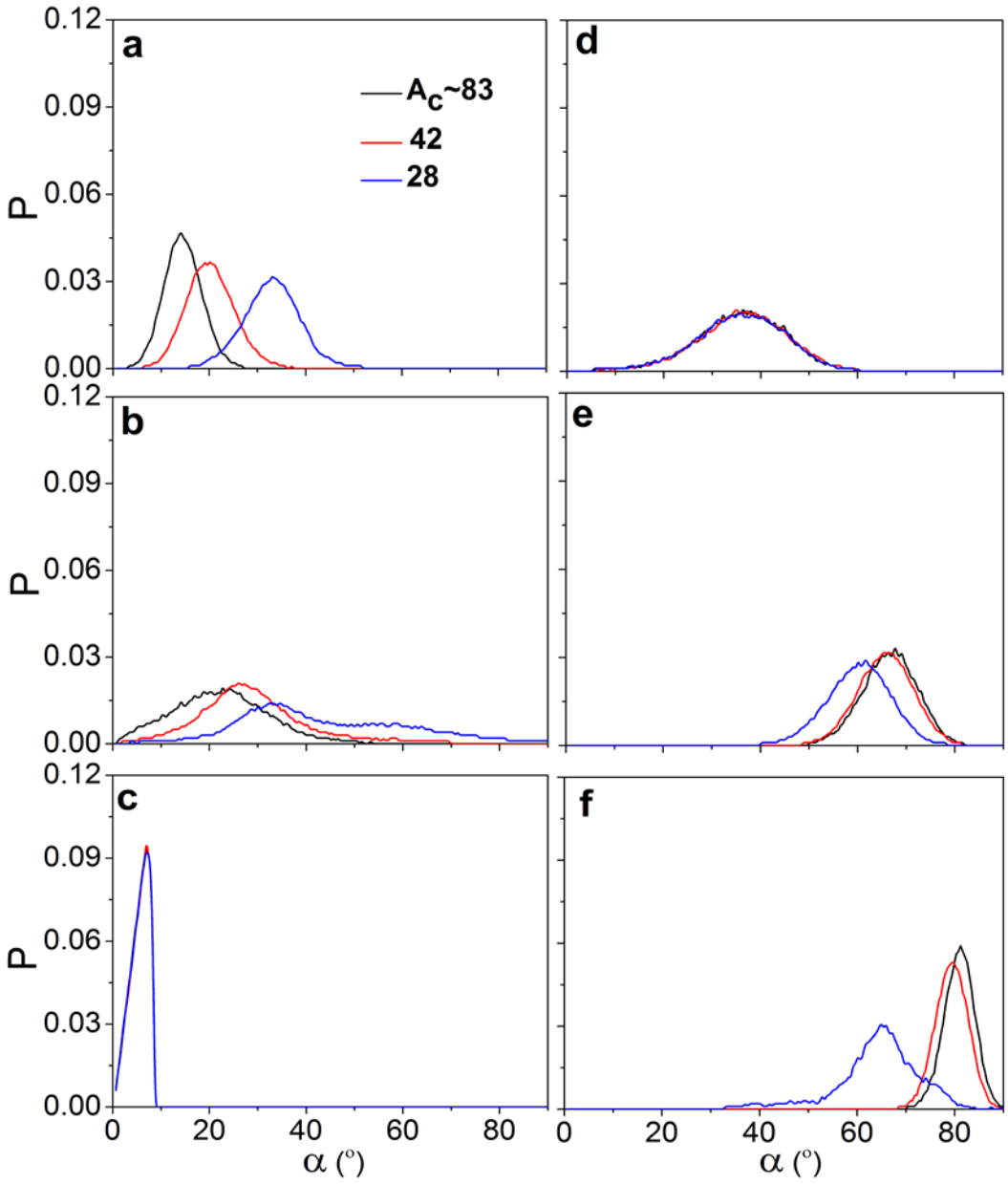

Figure 4S.2. Probability distribution of the orientation angle for ellipsoidal NPs at the water-decane interface. The results are obtained for NPs with nonpolar fraction x=70. Different panels are for different NPs. In each panel, three NP surface densities are presented. In some cases the lines overlap. Different panels are for NPs with different aspect ratio: (a) c/b=0.3; (b) c/b=0.5; (c) c/b=1; (d) c/b=1.5; (e) c/b=2; (f) c/b=4.

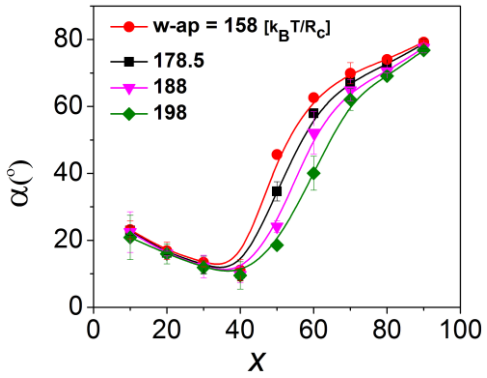

Figure 4S.3. Orientation angle as a function of surface properties for prolate NPs with c/b=2. Different lines are results obtained for different w-ap interaction parameters. The results are obtained at a surface coverage correspondent to a surface area per NP $A_c \approx 84.34\ R_c^2$. Error bars represent one standard deviation from the average, and can be smaller than symbols. Lines are guides to the eye.

B. Supporting Information for chapter 5

In **Figure 5S.1** we show representative snapshots for NPs with aspect ratio of 2 when adsorbed at oil droplet interface. The droplet diameter is $50R_c$. The interface area per NP is $A_c=90.5\,R_c^2$. The NPs with N=10, panel a, create a radial nematic phase. The NPs with N=90, panel b, show an isotropic phase.

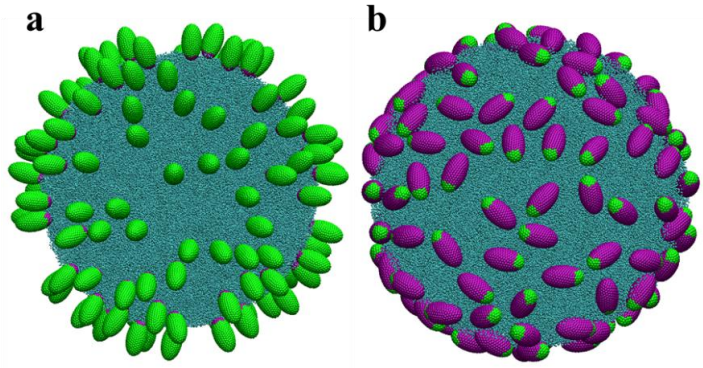

Figure 5S.1. Simulation snapshots of NPs with aspect ratio 2 adsorbed on an oil droplet immersed in water. The color code is that of **Figure 5S.1** in the main text. The droplet diameter is $50R_c$. Left and right panels are for NPs with N=10 and N=90, respectively. The area per NP is $A_c=90.5\,R_c^2$.

In **Figure 5S.2** we show representative simulation results obtained for NPs with aspect ratio 2 and N=70 adsorbed on an oil droplet of droplet diameter d=50R_c. The results shown in panel (a) are for an isotropic phase, obtained with the o-ap interaction parameter set at 161.5 k_BT/R_c. The results in panel (b) are obtained by reducing this parameter to 120 k_BT/R_c. The radial nematic order S_R~0.16 for panel (a) (indicative of an isotropic phase) and ~0.8 for panel (b) (indicative of a radial nematic phase).

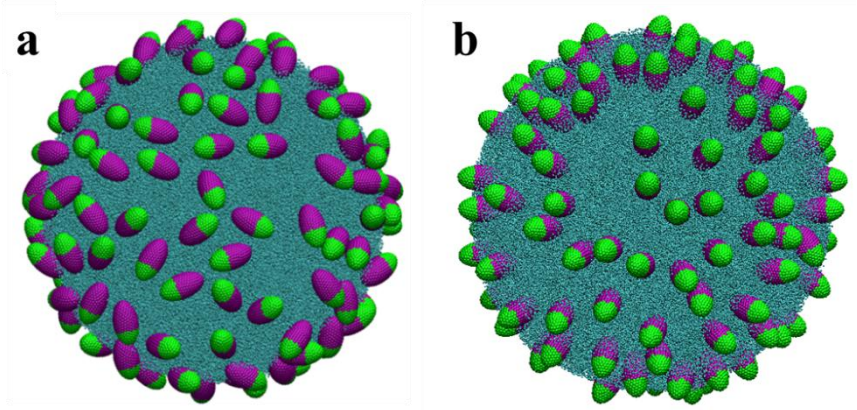

Figure 5S.2. Simulation snapshots for NPs with aspect ratio 2 and N=70 adsorbed on one oil droplet. The color code is that of **Figure 5S.1**. The droplet diameter is 50R_c. Panel (a), shown also in the main text, was obtained when the o-ap interaction parameter was set to 161.5 k_BT/R_c. Panel (b) was obtained when the o-ap interaction parameter was reduced to 120 k_BT/R_c.

In **Figure 5S.3** we report the averaged orientation angle as a function of area per NP, A_c, for NPs with aspect ratio 4 and N=30 adsorbed either on a flat oil-water

interface, or on an oil droplet of diameter $50R_c$. Note that the orientation angles are always larger than 40°.

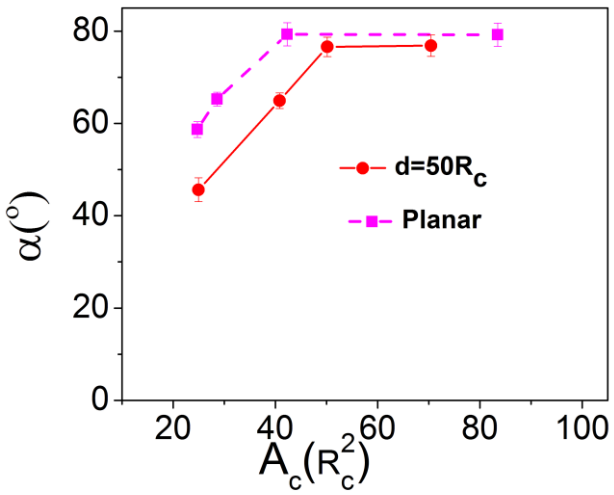

Figure 5S.3. Average orientation angle as a function of area per NP. Results are for NPs with aspect ratio 4 and N=70. The NPs are either adsorbed at a flat interface, or on an oil droplet of diameter $50R_c$. The error bars are obtained as one standard deviation from the average of three simulations. Lines are guides to the eyes.

In **Table 5S.1**, we report S_R and the average orientation angle for NPs with aspect ratio c/b=2 adsorbed on a water droplet of diameter d~$40R_c$ immersed in oil. We present the results for N=30 and N=70 NPs at different NP surface densities. The results indicate that S_R does not change substantially as Ac varies for both NP types considered. S_R>0.81 for NPs with N=30 suggests a radial nematic phase, and S_R<0.4 for NPs with N=70 indicates an isotropic phase. The orientation angle with respect to the droplet radial direction for N=30 NPs is always small (~15°), independent of NP surface density. This observation is consistent with radial nematic phase characteristic,

where NPs are parallel to the droplet radial vector. The orientation angle for N=70 NPs changes from ~ 60° at low NP surface density to ~ 38° at the highest NP density considered.

Table 5S.1. Radial order parameter S_R, and average orientation angle of NPs adsorbed on a water droplet of diameter $40R_c$ immersed in oil. The errors are obtained as one standard deviation from the average. NPs have aspect ratio 2 and surface chemistry N=30 or 70.

Area per NP (A_c)	N=30		N=70	
	S_R	$\alpha(°)$	S_R	$\alpha(°)$
60.2	0.81 ± 0.04	16.2 ± 2.3	0.2 ± 0.08	60.5 ± 3.5
22.8	0.91 ± 0.01	11.8 ± 0.5	0.45 ± 0.03	38.8 ± 2.7

In **Figure 5S.4** we report representative simulation snapshots for NPs of aspect ratio 2 adsorbed on water droplets of diameter $40R_c$. The NPs with N=30 (panel a) yield a radial nematic structure, while the NPs with N=70 (panel b) are isotropic. These results are similar to those obtained for the NPs on the oil droplet.

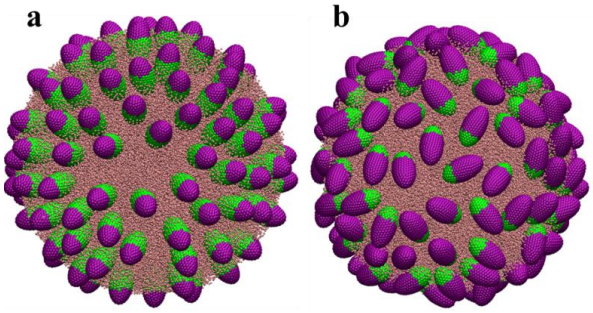

Figure 5S.4. Simulation snapshots of NPs with aspect ratio 2 adsorbed on one water droplet of diameter $40R_c$. The color code is that of **Figure 5S.1**. Left and right panels are for NPs with N=30 and N=70, respectively. The area per NP is $A_c=60\,R_c^2$. Oil molecules are not shown for clarity.

In **Figure 5S.5** we report a sequence of simulation snapshots obtained for a system containing NPs of aspect ratio 4 and N=30 adsorbed on one water droplet of diameter $40R_c$. One particle is highlighted in blue to ease visualization. The area per NP is Ac=60 R_c^2 . The highlighted NP was found to have small orientation angle at t=0 and t=39 ns and large orientation angle at t=16 and 66ns. This indicates that the NPs simulated here have the ability of changing their preferred orientation with respect to the radial direction during the length of our simulations.

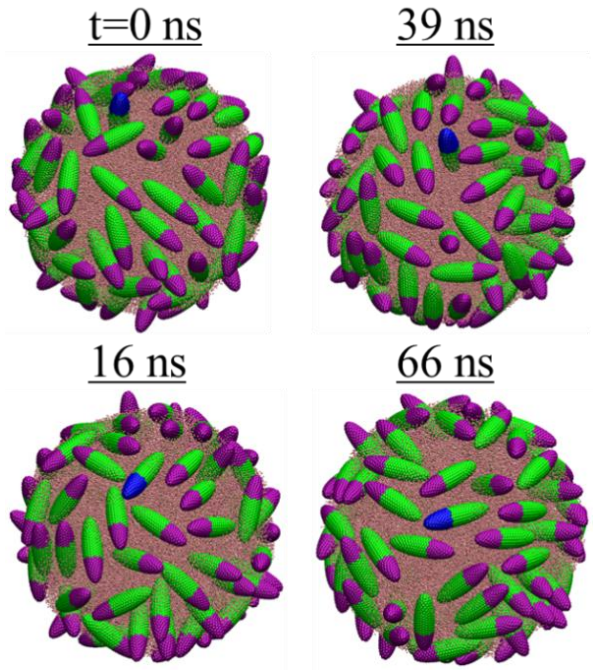

Figure 5S.5. Sequence of simulation snapshots obtained for a system containing NPs of aspect ratio 4 and N=30 adsorbed on one water droplet of diameter $40R_c$, immersed in oil, at different simulation times. The color code is that of **Figure 5.1**, except one particle is highlighted in blue to ease visualization. The area per NP is Ac=60 R_c^2 . The labels indicate the simulation time.

Simulation snapshots for NPs with aspect ratio 4 adsorbed on water droplets of diameter $40R_c$ as a function of surface density are shown in **Figure 5S.6**. The left (right) panels are for N=30 (N=70) NPs. An isotropic orientation is observed for both N=30 NPs (panel a) and N=70 NPs (panel d) when the NP density is low, $A_c=60\,R_c^2$. When the NP surface density increases to $A_c=45\,R_c^2$, most of N=30 NPs (panel b) have low orientation angle. At this condition, N=70 NPs (panel e) yield axial nematic domains. When the NP density is sufficiently high (panels e and f), a radial nematic phase is observed for both N=30 and N=70 NPs.

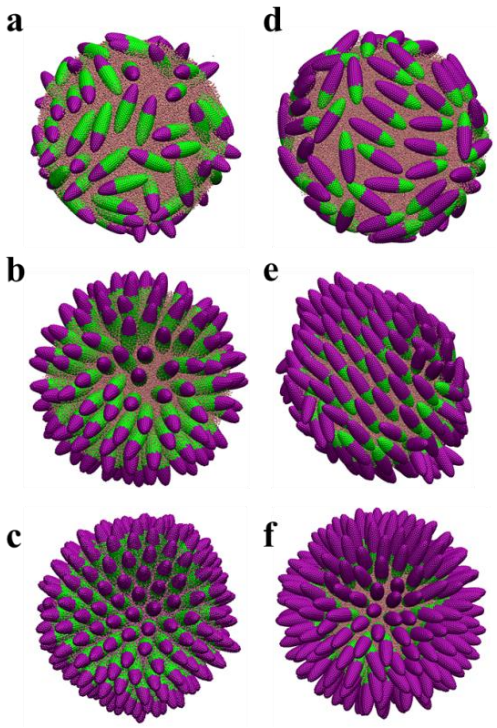

Figure 5S6. Representative simulation snapshots for ellipsoidal Janus NPs of aspect ratio 4 adsorbed on a water droplet of diameter $40R_c$. The left (right) panel is for NPs with N=30 (70). The surface density increases from top to bottom: in panels (a) and (d) $A_c=60\,R_c^2$; (b) and (e) $A_c=45\,R_c^2$; (c) and (f) $A_c=32\,R_c^2$.

Attachment energy calculation

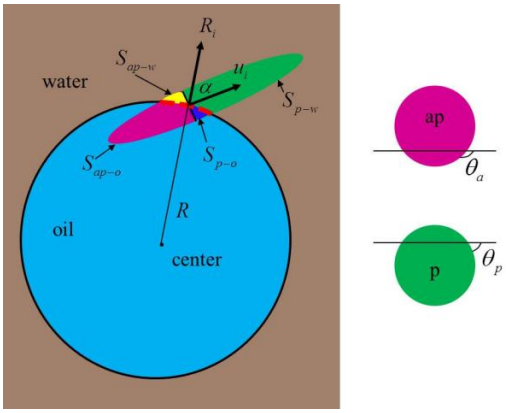

Figure 5S.7. Schematic representing an ellipsoidal Janus NP adsorbed at the oil-water interface. In this picture, ap (pink), p (green), o (cyan), and w (purple) represent nonpolar, polar, oil, and water, respectively. u_i and R_i are the unit vectors along the NP c axis and along the radial direction from the center of the droplet, respectively. S_{p-w}, S_{p-o}, S_{ap-w}, and S_{ap-o} are polar NP surface in water, polar surface in oil, nonpolar surface in water, and nonpolar surface in oil, respectively. The interfacial area occupied by the NP, S_I, is highlighted in red. θ_a and θ_p are the contact angles of completely nonpolar and polar spherical NPs, respectively.

The attachment energy in Eq. (5.2) can be derived as the following steps.[52,150,172,173]

The energy when a NP is totally immersed in oil phase

$$E_o = \gamma_{p-o}(S_{p-w} + S_{p-o}) + \gamma_{ap-o}(S_{ap-o} + S_{ap-w}) + \gamma_{o-w}S_0 + P_oV_{NP}$$

(5S.1)

The energy when this NP is adsorbed at the water/oil interface

$$E_I = \gamma_{p-o}S_{p-o} + \gamma_{ap-o}S_{ap-o} + \gamma_{p-w}S_{p-w} + \gamma_{ap-w}S_{ap-w} + \gamma_{o-w}(S_0 - S_I) + P_oV_{NP-o} + P_wV_{NP-w}$$

(5S.2)

In these equations, E_o and E_I are the energies when the NP immersed in oil phase and adsorbed at the oil/water interface, respectively; γ_{o-w}, γ_{p-o}, γ_{ap-o}, γ_{p-w}, and γ_{ap-w} are the surface tension between oil and water, polar and oil, nonpolar and oil, polar and water, and nonpolar and water respectively; S_{p-w}, S_{p-o}, S_{ap-w}, and S_{ap-o} are polar NP surface immersed in water, polar NP surface immersed in oil, nonpolar NP surface in water, and nonpolar NP surface in oil, respectively; P_o and P_w are the pressure of the oil and water phases, respectively; V_{NP-o}, V_{NP-w}, and V_{NP} are the NP volume immersed in oil phase, water phase, and total NP volume, respectively. S_0 and S_I are the total oil/water interface and the oil/water interface occupied by the NP.

The attachment energy ΔE is obtained by subtracting Eq. (5S.2) from Eq. (5S.1)

$$\Delta E = S_{p-w}(\gamma_{p-w} - \gamma_{p-o}) + S_{ap-w}(\gamma_{ap-w} - \gamma_{ap-o}) - \gamma_{o-w}S_I + (P_w - P_o)V_{NP-w} \quad (5S.3)$$

We apply the Young's relation

$$\begin{aligned} \gamma_{o-w}\cos\theta_P &= \gamma_{p-o} - \gamma_{p-w} \\ \gamma_{o-w}\cos\theta_a &= \gamma_{ap-o} - \gamma_{ap-w} \end{aligned} \quad (5S.4)$$

Substituting Eq. (5S4) into Eq. (5S3), we obtain

$$\Delta E = -\gamma_{o-w}(S_{p-w}\cos\theta_p + S_{ap-w}\cos\theta_a + S_I) + (P_w - P_o)V_{NP-w} \quad (5S.5)$$

The difference between pressure inside and outside droplet can be described by Laplace pressure

$$P_{inside} - P_{outside} = \frac{2\gamma_{o-w}}{R} \quad (5S.6)$$

Here R is the droplet radius.

For the water droplet:

$$P_w - P_o = \frac{2\gamma_{o-w}}{R} \tag{5S.6a}$$

For the oil droplet

$$P_w - P_o = \frac{-2\gamma_{o-w}}{R} \tag{5S.6b}$$

The attachment energy when a NP adsorbs on water droplet

$$\Delta E = -\gamma_{o-w}(S_{p-w}\cos\theta_p + S_{ap-w}\cos\theta_a + S_1) + \frac{2\gamma_{o-w}}{R}V_{NP-w} \tag{5S.7}$$

The attachment energy when a NP adsorbs on oil droplet

$$\Delta E = -\gamma_{o-w}(S_{p-w}\cos\theta_p + S_{ap-w}\cos\theta_a + S_1) - \frac{2\gamma_{o-w}}{R}V_{NP-w} \tag{5S.8}$$

We can combine Eq. (S7) and (S8) in a general form

$$\Delta E = -\gamma_{o-w}(S_{p-w}\cos\theta_p + S_{ap-w}\cos\theta_a + S_1) - \frac{2\varepsilon\gamma_{o-w}}{R}V_{NP-w} \tag{5S.9}$$

Where ε = 1 when the droplet is water and ε = -1 when the droplet is oil.

Reference

(1) Hirose, Y.; Komura, S.; Nonomura, Y. Adsorption of Janus particles to curved interfaces. *J. Chem. Phys.* **2007**, *127*, 054707-054712.

(2) Park, B. J.; Lee, D. Configuration of nonspherical amphiphilic particles at a fluid-fluid interface. *Soft Matter* **2012**, *8*, 7690-7698.

(3) Binks, B. P.; Fletcher, P. D. I. Particles Adsorbed at the Oil−Water Interface: A Theoretical Comparison between Spheres of Uniform Wettability and "Janus" Particles. *Langmuir* **2001**, *17*, 4708-4710.

(4) Jiang, S.; Granick, S. Janus balance of amphiphilic colloidal particles. *J. Chem. Phys.* **2007**, *127*, -161102-161106.